AIR-COOLED WINDOW FOR A RECUPERATED SOLAR-DISH BRAYTON CYCLE USING A TURBOCHARGER AND SHORT-TERM THERMAL STORAGE

by

Jan Hendrik de Beer

Submitted in partial fulfilment of the requirements for the degree
MASTER OF ENGINEERING (Mechanical Engineering)

in the

Faculty of Engineering, the Built Environment and Information Technology

UNIVERSITY OF PRETORIA
South Africa

2022

Abstract

Title:	Air-cooled window for a recuperated solar-dish Brayton cycle using a turbocharger and short-term thermal storage
Author:	J.H. de Beer
Supervisor:	Prof W.G. le Roux
Co-supervisor:	Prof J.P. Meyer
University:	University of Pretoria
Department:	Mechanical and Aeronautical Engineering
Degree:	MEng (Mechanical Engineering)

A recuperated solar-dish Brayton cycle using an off-the-shelf turbocharger as a micro-turbine and a rectangular cavity receiver with integrated thermal storage was considered for this study. Due to the high temperatures that these solar receivers reach, a considerable amount of heat is lost to the environment through the aperture, decreasing the efficiency of the cycle. In this research, the heat losses from the solar receiver with integrated thermal storage had to be reduced by utilising a glass channel on the inside of the cavity receiver, which ran parallel to the receiver walls and was cooled by the working fluid (air) flowing from the compressor. The objective of this conceptual study was to investigate the impact of the air-cooled window on the performance of the cycle and to provide insight into the feasibility of the implementation of the cooling window. An entropy generation minimisation technique combined with a SolTrace analysis was used to analyse the impact of the cooling window on the performance of the cycle at steady state. Results showed that the maximum solar-to-mechanical efficiencies were on average between 41% and 45% lower than for the cycle without the window. The results also indicated that a smaller cooling channel width increased the pressure drop and cooling effectiveness but further decreased the solar-to-mechanical efficiency of the cycle. However, a smaller cooling channel width also produced lower glass surface temperatures, which was very important for the structural integrity of the glass. Furthermore, it was found that the cooling window increased the exhaust temperature of the optimised cycle. The exhaust temperature of the cycle with the window was higher than the exhaust temperature of the cycle without the window, which led to a higher energy utilisation factor of between 9% and 11% if the exhaust was used for cogeneration such as water heating or thermal energy storage. Therefore, this conceptual study indicated that it might not be feasible to implement the cooling window, except where a higher cycle exhaust temperature was preferred for cogeneration.

Acknowledgements

I wish to express my gratitude to the following people and institutions who made this dissertation possible:

Research outputs

The following research outputs resulted from this work:

Journal article:

The findings from this work have been summarised into a manuscript which has been submitted for publication in a suitable journal article.

Conference paper:

De Beer, J. H., Le Roux, W. G. & Meyer, J. P., 2021. Conceptual investigation of an air-cooled window cover in the tubular receiver of a recuperated solar thermal Brayton cycle. In: Proceedings of the 7th Southern African Sustainable Energy Conference (SASEC 2021), 17-19 November, Stellenbosch, South Africa.

Table of contents

List of figures

vii

viii

ix

List of tables

xi

Nomenclature

Alphabetic Symbols	Description	Unit
a	Aperture width	m
a	Recuperator channel width	m
$\bar{a}$	Constant for heat transfer coefficient relation	-
A	Area	m²
AR	Aspect ratio	-
b	Recuperator channel height	m
$\bar{b}$	Constant for heat transfer coefficient relation	-
B	View factor function	-
BSR	Blade speed ratio	-
$c_{p,0}$	Constant pressure specific heat	J/kgK
c	Linear fit constant	-
D	Diameter	m
D_1	Error between exergy and first law calculation of $\dot{W}_{net}$	%
D_2	Error between exergy and heat balance calculation of $\dot{W}_{net}$	%
f	Darcy friction factor	-
F	View factor	-
g	Gravitational constant	m/s²
h	Heat transfer coefficient	W/m²K
$\bar{h}$	Specific enthalpy	J/kg
H	Height of recuperator	m
i	Indexing variable	-
I	Solar irradiation	W/m²
j	Indexing variable	-
k	Thermal conductivity	W/mK
l	Indexing variable	-
L	Length	m
$\dot{m}$	Mass flow rate	kg/s
m	Slope of linear equation	-
n	Number of parallel flow channels in one direction	-
N	Number of glass divisions (N and N_{div})	-

N'	Speed of micro-turbine shaft	rpm
Nu	Nusselt number	-
NTU	Number of transfer units	-
p	View factor relation function	-
p	Wetted perimeter	m
P	Pressure	Pa
Pr	Prandtl number	-
q	View factor relation function	-
$\dot{Q}$	Heat transfer rate	W
$\dot{Q}_{loss}$	Heat loss rate	W
$\dot{Q}_{net}$	Net energy transfer rate available to cooling fluid	W
$\dot{Q}^*$	Rate of solar energy intercepted	W
r	Pressure ratio	-
Ra	Rayleigh number	-
Re	Reynolds number	-
s	Specific entropy	J/kgK
S	Entropy	J/K
t	Thickness	m
t'	Time	s
T	Temperature	°C / K
T^*	Apparent temperature of the sun as an exergy source	K
u	View factor relation function	-
U	Overall heat transfer coefficient	W/m^{2}K
v	View factor relation function	-
V	Velocity	m/s
$\dot{W}$	Power	W
x	Geometric coordinates (x_1 and x_2)	m
y	Geometric coordinates (y_1 and y_2)	m
z	Geometric distance	m

Greek Symbols	Description	Unit
α	Absorptivity	-
α	Thermal diffusivity	m^2/s
β	Coefficient of thermal expansion	K^{-1}

Γ	Ratio between fluxes	-
Δ	Change in	-
δ	Geometric coordinates (δ_1 and δ_2)	m
ε	Emissivity	-
η	Efficiency	-
θ	Receiver inclination angle	degrees
ν	Kinematic viscosity	m^2/s
ξ	Geometric coordinates (ξ_1 and ξ)	m
ρ	Density	kg/m^3
ρ	Reflectivity	-
σ	Stefan-Boltzmann constant	W/m^2K^4
τ	Transmissivity	-
ϕ	Exergy	W
$\bar{\psi}$	Constant for heat transfer coefficient relation	-
ψ	Flow exergy	J/kg

Subscripts	Description
0	Initial
0	Zero-pressure (for c_p)
1-2	From Surface 1 to Surface 2
1-11	Position in cycle (refer to Figure 1.1 or Figure 1.3)
a	Air
abs	Absorbed
aper	Aperture
avg	Average
C	Cold side
c	Compressor
c.v.	Control volume
cav	Cavity
chn	Channel
cond	Conduction
conv	Convection
D	Based on diameter (or hydraulic diameter)

dish	Of the dish
div	Division
e	Exit
eff	Effective
f	Fluid
gap	Of the gap
gl	Glass
gen	Generated
H	Hot side
h	Hydraulic
i	Inlet
inc	Incident
L	Based on the length
loss	Heat loss
max	Maximum
n	Glass section number
net	Net
out	Outlet
rad	Radiation
rec	Receiver
reg	Recuperator
s	Surface
ss	Stainless steel
t	Turbine
th	Thermal
tot	Total
w	To the water
wall	At the wall
win	Window
∞	Free stream / surrounding area

Chapter 1

Introduction

Concentrating solar power (CSP) technologies use mirrors to focus the energy of the sun onto a receiver and convert it into heat. The heat can then be used to drive a power cycle to generate electricity. Solar receivers reach very high temperatures, which lead to significant heat losses to the environment, consequently reducing a power cycle's thermal efficiency. The research investigated the performance impact of a cooling window on the inside of the solar receiver of a solar-dish Brayton cycle. This chapter introduces the research by briefly discussing the background and context. Further, the research problem, objectives, significance and limitations of the study are presented.

1.1   Background and previous work

The closed Brayton cycle was first developed in the early 1930s to generate electricity for which the cycle showed high reliability and long-term operation (Pietsch & Brandes, 1989). Extensive testing with the open Brayton cycle in aircraft gas turbines provided a base for the development of closed Brayton cycle engines in the 1960s to be used in space power applications where the sun is the only source of energy (Pietsch & Brandes, 1989). Small-scale solar thermal systems can provide renewable energy solutions to areas where grid access and space are very limited. For the Brayton cycle, off-the-shelf turbochargers have been investigated to reduce overall cycle costs (Le Roux et al., 2014a, Le Roux et al., 2014b). Le Roux and Sciacovelli (2019) studied a recuperated solar-dish Brayton cycle using off-the-shelf turbochargers and short-term thermal storage. Le Roux and Sciacovelli (2019) showed that maximum solar-to-mechanical efficiencies of 10% to 15% could be achieved at receiver temperatures of between 900 K and 1200 K (when the dish reflectivity and intercept factor were both assumed to be 85%). The current study used the methodology and code from Le Roux and Sciacovelli (2019) as a base to which the developed code was added.

1.2   Problem formulation

Heat losses are a big concern to the designer of an open-cavity solar receiver due to the high temperatures that can be achieved with CSP. The heat losses from a solar receiver negatively impact the solar-to-mechanical efficiency of a power cycle. The thermal losses of an open-

1

cavity solar receiver include the convective and radiative losses from the cavity to the surroundings as well as the conductive heat losses through the insulation. The radiative losses depend on the cavity wall temperature, the shape factors as well as the emissivity of the receiver walls (Prakash et al., 2009). The radiative and conductive heat losses are reported to be independent of the inclination angle of the cavity (Prakash et al., 2009). The convective heat losses depend on the air temperature on the inside of the cavity, the inclination angle of the cavity as well as the environmental wind conditions (Clausing, 1983). Therefore, these dependencies lead to complex convection heat transfer correlations.

By using computational fluid dynamics (CFD) and ray tracing on an open-cavity tubular solar receiver, Craig et al. (2020) found that the receiver had a total heat loss rate of 6.8 kW at a 0° inclination angle (for a 4.8 m diameter parabolic dish) and a maximum receiver temperature of 921 K. Le Roux and Sciacovelli (2019) also found that the maximum total heat losses from the same solar receiver were about 12 kW at a receiver temperature of 1200 K. Some research has been done to minimise heat losses from rectangular solar receivers by using glass covers (Cui et al., 2013, Fischer & Hahne, 2000, Fuqiang et al., 2014, Subedi et al., 2019). However, keeping the glass covers cool under highly concentrated solar irradiation has proved to be a difficult task. Too et al. (2017) tested the difference in thermal performance of a tubular solar receiver with and without a quartz window. They found that the glass cracked after an hour of steady-state operation at an outlet gas temperature of 750 °C. Uhlig and Röger (2004) mention that when quartz glass is subject to high temperatures, the recrystallisation of the glass will be accelerated. High receiver temperatures also increase the heat loss by infrared radiation to the ambient environment. For these reasons, Uhlig and Röger (2004) suggest that it is necessary to develop a cooling system to keep the quartz glass temperature below 800 °C.

1.3   System description

The open and direct solar-dish Brayton cycle under consideration was investigated by Le Roux (2015). The solar-dish Brayton cycle is envisaged to be implemented on a small scale with a parabolic dish concentrator and an open-cavity tubular solar receiver, as shown in Figure 1.1. The cycle can be paired with commercial turbochargers to lower the system's overall cost. The results from an analytical model showed that maximum thermal efficiencies of 20.2% to 34.2% could be reached at receiver phase-change temperatures of between 900 K and 1200 K (Le Roux & Sciacovelli, 2019). The receiver was made of stainless steel 316 pipes, which were coiled to form a rectangular receiver. The receiver was also encapsulated with thermal storage,

which contained a phase-change material, thus keeping a constant temperature around the coil during phase change. A case study was done by Le Roux and Sciacovelli (2019), who found that molten aluminium was notable for further investigation as phase-change material in a simple and low-cost solar-gas hybrid Brayton cycle configuration with cogeneration.
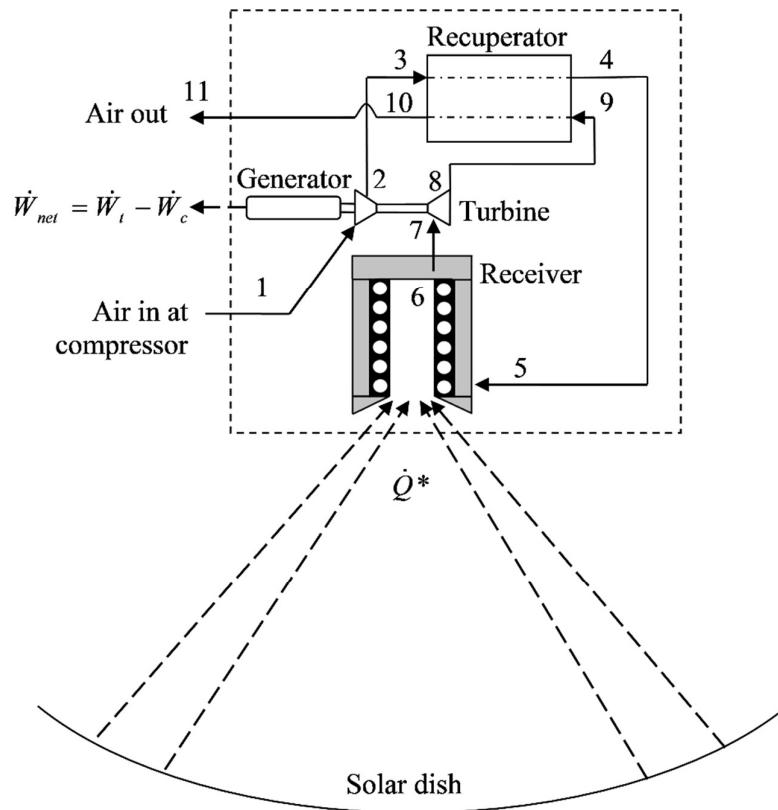
Figure 1.1 Solar-dish Brayton cycle without window cover (Le Roux & Sciacovelli, 2019)

The reflected rays ($\dot{Q}^*$ in Figure 1.1) heat the inside of the receiver walls, after which the heat is transferred to the working fluid (air). The compressor increases the pressure of the air before it enters the recuperator and receiver (State 2 in Figure 1.1). Once the air has passed through the receiver, it expands in the turbine, which provides rotational power for the compressor and electrical load (States 7 and 8 in Figure 1.1) (Le Roux et al., 2014a). In the recuperator, hot exhaust air from the turbine preheats the colder air before it enters the receiver (States 3, 4, 9 and 10 in Figure 1.1). High recuperator effectiveness is often used in Brayton cycles to maximise cycle efficiency (Pietsch & Brandes, 1989). The recuperator also allows for a lower

3

operating pressure in the receiver due to the preheating of the ambient air before it enters the receiver (Le Roux & Sciacovelli, 2019). The receiver considered in this study was a low-pressure receiver because it was to be paired with a low-pressure turbocharger. The operating pressure of the turbomachinery is between 1.3 and 2.5 times the ambient pressure (Le Roux et al., 2011, Le Roux et al., 2012a, Le Roux et al., 2012b, Le Roux et al., 2013). For the solar-dish Brayton cycle, the maximum receiver phase-change temperature is of great importance. A higher receiver temperature leads to a better-performing Brayton cycle (Le Roux et al., 2012a), but this also means an increased heat loss rate to the environment.

A proposed solution was to place two glass panes parallel to each of the four receiver walls as well as parallel to the top wall, specifically to minimise radiation and convection heat losses. A 3D section view was created with *ANSYS* and is shown in Figure 1.2. Glass is transparent to solar radiation and opaque to infrared radiation, making it an excellent candidate to curb the radiation heat losses from the cavity. The idea is to allow air from the compressor (between States 2 and 3 in Figure 1.1) to flow through the channel that is created by the two glass panes to cool it down. This is done to prevent it from shattering due to the very high temperatures that are reached with the concentrated solar irradiation on the inside of the cavity. Figure 1.3 shows the cycle with the included cooling window.
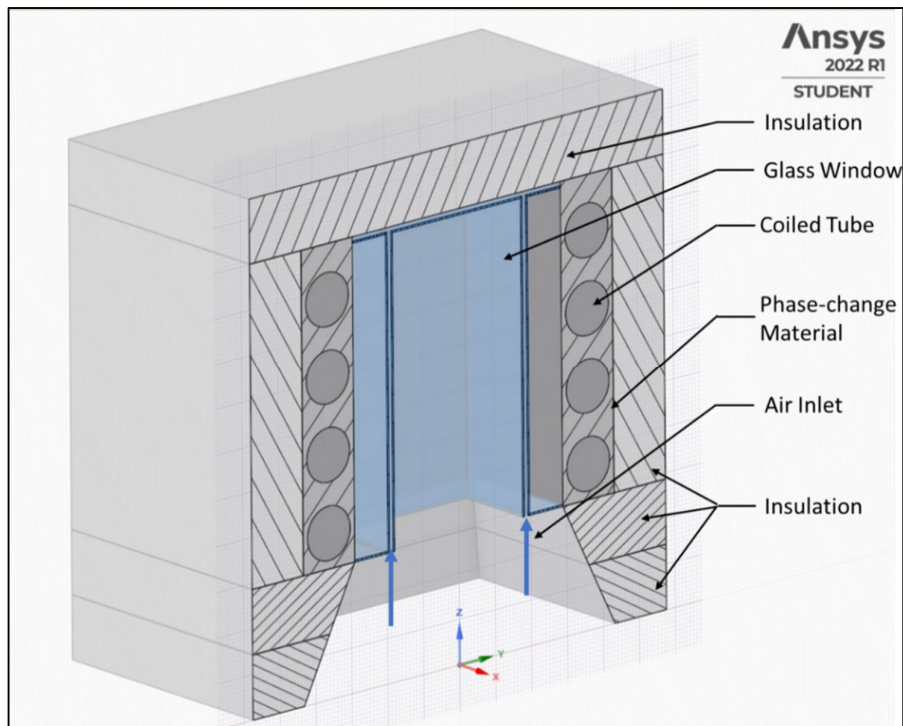
Figure 1.2 3D section view of receiver with window (not drawn to scale)
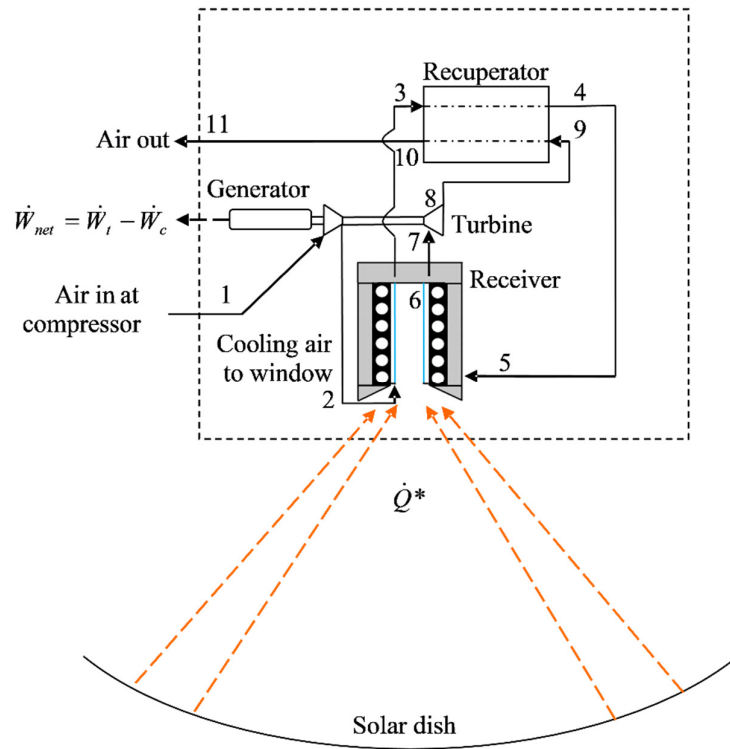
Figure 1.3 Solar-dish Brayton cycle with window cover, adapted from Le Roux and Sciacovelli (2019).

1.4   Purpose of the study

To minimise heat losses from the solar receiver, a cooling channel made up of glass was placed on the inside of a rectangular solar receiver, parallel to the receiver walls. The research investigated the impact of this cooling window on the performance of the solar-dish Brayton cycle.

1.5   Objectives

The research objectives included analysing the impact of the cooling window on the solar-to-mechanical efficiency and energy utilisation factor using numerical methods. The glass surface temperature was another important property by which the impact of the cooling window would be measured. The different performance parameters for this novel cooling window and the solar receiver without the cooling window were compared. This study's results were compared to Le Roux and Sciacovelli (2019) to further analyse the cooling window's impact. This comparison would provide a clear understanding of the impact of the cooling window on the performance of the solar-dish Brayton cycle.

5

1.6   Scope of the work

Essentially, the conceptual study investigated whether the cooling window was feasible to reduce the heat losses of the solar receiver while maintaining acceptable solar-to-mechanical efficiencies. The results of this study are limited to open solar-dish Brayton cycles that use a parabolic solar dish to concentrate the solar irradiation on an open-cavity coiled tube rectangular receiver with thermal storage. For this study, only one glass thickness was considered and the conduction heat losses from the glass were assumed to be negligible. The solar receiver dimensions remained fixed throughout the study and were based on a previous optimisation study (Le Roux et al., 2014a). The rectangular receiver aperture had dimensions of 0.25 m × 0.25 m with a cavity depth of 0.5 m. The coiled tubes embedded in the receiver were made of stainless steel 316 and the tube diameter was 0.0833 m. It was assumed that the phase-change material, as well as the inner-cavity walls and the tube surface, was at a constant temperature (the melting temperature of the phase-change material), as proposed by Le Roux and Sciacovelli (2019).

1.7   Layout of dissertation

Chapter 2 provides a review of the existing literature on the different heat loss mechanisms from solar receivers and solar receivers with glass covers. Different types of glass that are suitable for high-temperature applications were also reviewed. Chapter 3 provides the methodology, which includes the numerical model and code structure that were used. The methodology that was used by Le Roux and Sciacovelli (2019) was updated and modified to include the window concept. Chapter 4 provides the results. The optimum recuperator geometries and operating points for the different micro-turbines are given for different receiver temperatures. Concluding remarks and recommendations for future work are given in Chapter 5.

6

Chapter 2

Literature study

2.1 Introduction

This chapter briefly introduces the basic operation principles and historical background of CSP systems and the basic operation principles thereof. A review of the current literature on the heat loss mechanisms from solar receivers and the methods of reducing heat losses from solar receivers follows. The chapter also compares different solar receivers with and without glass covers. The type of glass and its thickness were important considerations in the study; the literature provides an overview of the properties and types of high-temperature glass.

2.2 Historical background

A systematic layout of a CSP system is shown in Figure 2.1. All the CSP systems in existence begin with a concentrator, which is intercepted by a receiver that converts the solar power to another form, usually thermal energy (Lovegrove & Pye, 2012). After the receiver, the energy can either be converted into its final desired form (such as electricity), or it is conveyed to another location for final conversion. In some instances, the power generation is carried out a distance away from the receiver and the collected thermal energy is transported away in a heat transfer fluid (HTF). The final stage of the CSP system is electricity generation, which usually occurs with a Stirling engine, organic Rankine cycle, Brayton cycle or photovoltaics (Lovegrove & Pye, 2012).
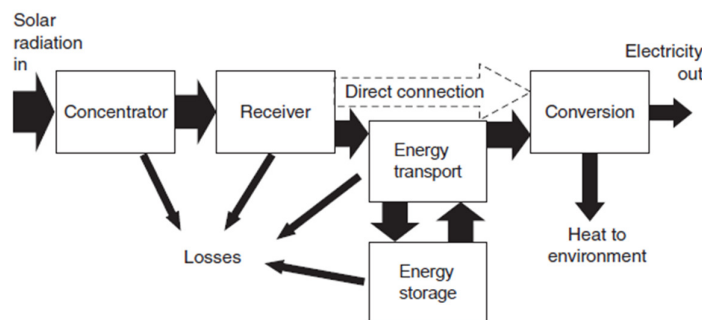
Figure 2.1 Representation of the components of a solar power system (Lovegrove & Pye, 2012)

The most notable solar concentrators are trough, linear Fresnel, dish and tower concentrators. Line-focusing systems (trough and linear Fresnel) concentrate the solar radiation by 50 to 100,

7

whereas point-focusing systems (dish and tower) concentrate the solar radiation by 500 to several thousand (Schiel & Keck, 2012). Point-focusing systems have the highest optical efficiencies, the highest concentration ratios, and the highest overall solar-to-mechanical efficiencies. Dish CSP systems use paraboloidal mirrors, which track the sun and focus solar radiation on a receiver where heat is absorbed and transported to a heat engine or in some cases to an HTF, which moves the thermal energy to a remote ground-based plant (Schiel & Keck, 2012).

Schiel and Keck (2012) provide numerous examples of the development of parabolic dish CSP systems, most of which used Stirling engines for power generation. The research and development of dish-mounted air Brayton engines were funded by the US dish programme in the 1980s because the Brayton engine was considered a lower risk than using the Stirling engines (Coventry & Andraka, 2017). According to Mills (2004), the Brayton cycle micro-turbines had the potential to replace Stirling engines in the two-axis solar-dish tracking market due to their much lower cost. Experimental testing by NASA of a 10 kWe closed Brayton cycle intended for a solar dish showed that the cycle had high reliability and efficiencies of above 30% at turbine inlet temperatures of between 1033 K and 1144 K (Pietsch & Brandes, 1989). A successful on-sun dish-mounted Brayton cycle demonstration was led by Sanders Associates in 1984 using a micro-turbine designed by Allied Signal (Torrance, CA) (Coventry & Andraka, 2017). Brayton Energy and Southwest Solar Technologies tested their dish-mounted Brayton system (Coventry & Andraka, 2017). Gavagnin et al. (2018) report that one of the most recent demonstrations of a dish-mounted Brayton cycle is the OMSoP project (Lanchi et al., 2015).

2.3   Heat loss mechanisms from solar receivers

When solar radiation falls on the solar receiver's surface, it increases the temperature of the absorber to above ambient temperature. This starts a process of heat loss from the receiver (Stine & Harrigan, 1985). Heat losses from open-cavity receivers consist mainly of radiation, convection and conduction heat losses. The conduction and radiation heat losses can easily be calculated from standard equations, as presented in McDonald (1995). However, the convection heat losses are a function of the wind speed, the angle of the receiver relative to the wind as well as the type of receiver, to name a few. Various convection heat loss models have been developed over the years, with each one applying to a specific type of receiver or receiver conditions.

8

2.3.1 **Convection**

2.3.1.1 Natural convection

Samanes et al. (2015) reviewed the available natural convection heat loss correlations of solar cavity receivers; some of the important correlations are shown in this section.

Le Quere et al. (1981) presented a correlation for the Nusselt number as a function of the Grashof number. However, their study used a cubical cavity, which is often used in central receiver cycles, and the cavity used in testing was modular by design so that each panel could be heated independently by an electrical source (McDonald, 1995). The total heat loss was calculated from the total electrical power consumed by each of the panels. The convection heat loss was then calculated by subtracting the conductive and radiative heat losses from the total heat loss. Le Quere et al. (1981) did not investigate the effect of the receiver dimensions on the heat losses. McDonald (1995) used the model of Le Quere et al. (1981) and investigated the impact of different receiver angles, aperture sizes and operating temperatures on convective heat losses. The operating temperature varied from about 150 °C to 315 °C, the aperture size varied from 15 cm to 66 cm, the angle of the receiver varied from -90° to 90°, and the convection heat losses varied from 0 kW to about 4 kW (maximum) for the entire range of the variables (McDonald, 1995). The Nusselt number of the Le Quere et al. (1981) model is given by equation (2.1):

$$Nu = \frac{q_{convection}L}{Ak\left(T_{panel} - T_{ambient}\right)} \tag{2.1}$$

The Grashof number was calculated with the standard equation:

$$Gr = \frac{g\beta\left(T_{panel} - T_{ambient}\right)L^3}{v^2} \tag{2.2}$$

All the fluid properties were evaluated at the ambient temperature and an experimental Nusselt number correlation based on empirically derived constants, which were a function of the receiver angle, was derived (see equation (2.3)).

$$Nu_L = aGr^b = \frac{hL}{k} \tag{2.3}$$

It must be noted that equation (2.3) is valid for a Grashof number of between 10^7 and 5×10^9 (Le Quere et al., 1981). The convective heat transfer coefficient could then be calculated by the standard Nusselt number equation, as shown in equation (2.3).

9

The Koenig and Marvin model was presented by Harris and Lenz (1985) and was based on operating temperatures of between 550 °C and 900 °C, whereas the Le Quere et al. (1981) model had an operating temperature range of between 150 °C to 315 °C. The standard convection heat loss and Nusselt number equations were used to calculate the heat loss and convection heat transfer coefficient. The Koenig and Marvin model was numerically investigated by McDonald (1995) for the same temperature and aperture size ranges used with the previous model. The convective heat losses ranged from about 0.1 kW to 2.2 kW for receiver angles of 0° to 90°. The Koenig and Marvin model was also used by Le Roux et al. (2014a).

The Clausing model was developed by A.M. Clausing in 1981 to enable the estimation of convective heat losses from cavity receivers. The model provided a good correlation with solar experiments and also indicated that the influence of wind on the convective losses was minimal under normal operating conditions (Clausing, 1981). The convective heat loss of the Clausing model was based on an energy balance between the convective energy loss within the cavity and the energy transported through the aperture of the cavity. It must be noted that the model was developed for large central receivers. The model divided the receiver into stagnation and convective zones and the two zones were analysed separately (McDonald, 1995). The equations of the Clausing (1981) model consisted of a fair number of empirical correlations, which were derived from experimental testing.

Another natural convection model for the inside of a receiver was developed by Paitoonsurikarn and Lovegrove (2006). This model was based on results from numerical simulations of three different cavity receiver geometries, one of which was a small-scale experimental model receiver, while the other two were full-scale receivers (Paitoonsurikarn & Lovegrove, 2006). The proposed correlation could predict approximately 50% of the data to within ±20% and 90% of the data within ±50%. This was much better and simpler to use than the previously discussed models. The three cavity receivers that were considered in the study by Paitoonsurikarn and Lovegrove (2003) are shown in Figure 2.2. The first three geometries (Figure 2.2a-c) are the same geometries that were considered in another study by Paitoonsurikarn and Lovegrove (2003), in which they developed the free convection heat loss correlation (Paitoonsurikarn & Lovegrove, 2003, Paitoonsurikarn et al., 2004). Figure 2.2d shows a model that was used by McDonald (1995) in experimental work and is included for additional validation of the numerical results (Paitoonsurikarn & Lovegrove, 2006). For each receiver geometry, a set of simulations was undertaken to calculate the heat loss at different receiver inclinations, θ,

10

ranging from 0° (cavity aperture is parallel with the horizon) to 90° (cavity aperture plane is vertical). Figure 2.2 shows the receivers used in the study of Paitoonsurikarn and Lovegrove (2006) in a 0° configuration, where a 90° inclination angle would be a rotation of the receiver 90° clockwise from the 0° inclination angle. Details of the numerical procedure and computational grids can be found in previous works by Paitoonsurikarn and Lovegrove (2003). A rectangular cavity model receiver was used to derive the new correlation. This correlation can be used for geometries with different dimensions due to a parameter used by Paitoonsurikarn and Lovegrove (2006) called the ensemble length. This ensemble length accounts for the effect of cavity geometric parameters in combination with the inclination of the receiver. It has been shown that the correlation compares well with a modified version of the Clausing model.
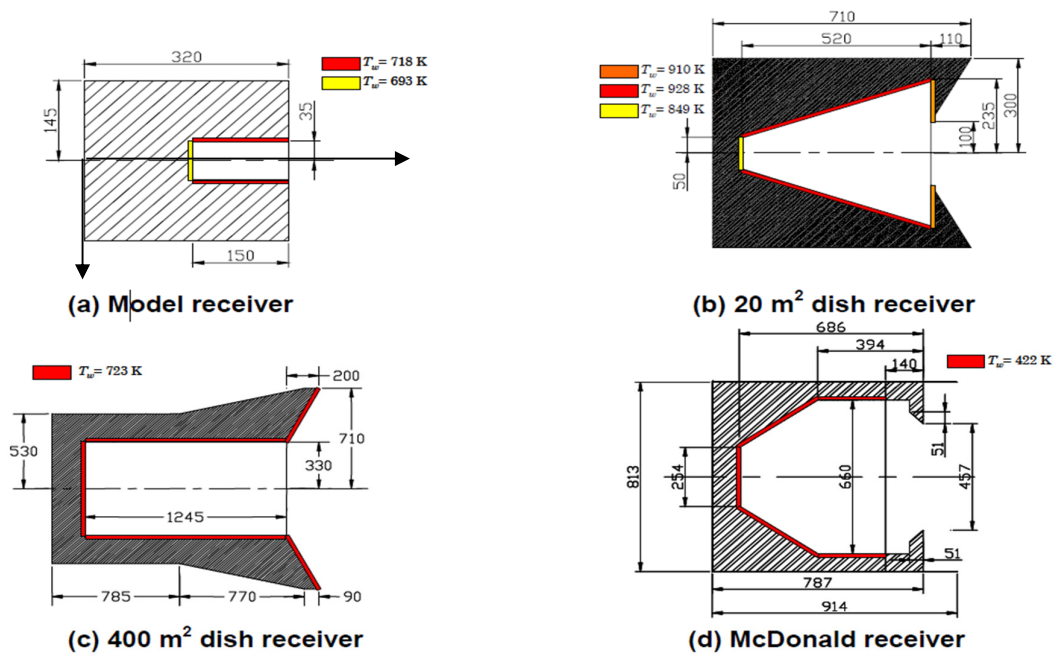
Figure 2.2 Different receiver models used in the study by Paitoonsurikarn and Lovegrove (2006)

Natural convection heat transfer is induced by the buoyancy forces created by a difference in the density of the fluid (Pendyala et al., 2015). The Rayleigh number is described as the ratio of buoyancy forces and thermal and momentum diffusivities and is defined as the product of the Grashof (equation (2.2)) and the Prandtl numbers. The characteristic length is the distance between the two plates and T_1 and T_2 are the temperatures of the hot and cold surfaces respectively. The fluid properties are often evaluated at the average fluid temperature ($T_{ave} = (T_1 + T_2)/2$). Various authors have proposed relations for predicting the Nusselt number (and

11

thus the heat transfer coefficient) of natural convection inside an enclosure. However, these relations are subject to strict parameters of validity, especially in terms of aspect ratio (H/L_c), Prandtl and Rayleigh numbers. Existing correlations for large aspect ratios are given in the work of MacGregor and Emery (1969) and two different Nusselt number correlations are given by equation (2.4) and equation (2.5):

$$Nu = 0.42 Ra_L^{\frac{1}{4}} Pr^{0.012} \left(\frac{H}{L}\right)^{-0.3} \tag{2.4}$$

with conditions:

$$10 < \frac{H}{L} < 40$$
$$1 < Pr < 2 \times 10^4$$
$$10^4 < Ra_L < 10^9$$

$$Nu = 0.046 Ra_L^{1/3} \tag{2.5}$$

with conditions:

$$1 < \frac{H}{L} < 40$$
$$1 < Pr < 20$$
$$10^6 < Ra_L < 10^9$$

CFD simulations provide significant insight into three-dimensional vertical rectangular enclosures. CFD experiments were done by Pendyala et al. (2015) for three-dimensional enclosures with varying aspect ratios and different fluid types. The aspect ratios vary from 0.125 to about 150 with the Prandtl number ranging from 0.01 to 4500. The proposed correlation for air is given by equation (2.6):

$$Nu = 1.46 \times 10^{-5} (AR)^{0.19} (\ln(Ra))^{3.337} \tag{2.6}$$

Equation (2.6) exhibits an average absolute deviation of about 11.3% and the sum of squared errors is about 0.015 (Pendyala et al., 2015), which is an acceptable error range considering the assumptions that are made when deriving the proposed correlations. The correlation of Pendyala et al. (2015) was used to model the natural convection in the enclosure between the receiver wall and the glass.

2.3.1.2   Forced convection

Forced internal convection occurs on the inside of the circular tubes, on the inside of the recuperator channels and on the inside of the glass channels. For the coiled tube, Le Roux and Sciacovelli (2019) used the Dittus-Boelter equation (Dittus & Boelter, 1930) to determine the Nusselt number and convection heat transfer coefficient.
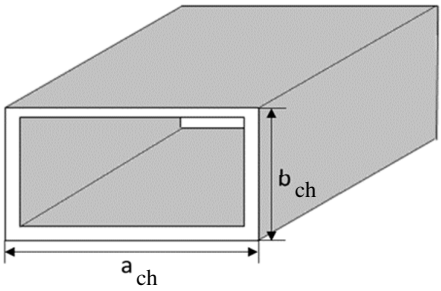
Forced convection heat transfer depends on the Reynolds number of the flow. For internal forced convection, most flows are laminar for a Reynolds number smaller than 2300 and fully turbulent for a Reynolds number larger than 10^4 (Ghiaasiaan, 2011). It is however suggested by Çengel and Ghajar (2015) that a conservative approach be used when designing piping networks and flows with a Reynolds number greater than 4000 are considered to be turbulent. The Reynolds number depends on the velocity and characteristic length. Since this work mostly deals with rectangular channels, the Reynolds number had to be altered by using the hydraulic diameter, which is given by equation (2.7):

$$D_h = \frac{2a_{chn}b_{chn}}{a_{chn} + b_{chn}} \qquad (2.7)$$

For laminar flow (Reynolds number smaller than 4000), the Nusselt numbers and friction factors for a rectangular duct are shown in Table 2.1 (Çengel & Ghajar, 2015), assuming constant heat flux. The heat transfer coefficient was calculated by rearranging the Nusselt number given in equation (2.8):

$$Nu = \frac{h_{conv}D_h}{k} \qquad (2.8)$$

Table 2.1 Nusselt numbers and friction factors for laminar flow in a rectangular section (Çengel & Ghajar, 2015)

	a_{chn}/b_{chn}	Nu	f
	1	3.61	$56.92/Re$
	2	4.12	$62.20/Re$
	3	4.79	$68.36/Re$
	4	5.33	$72.92/Re$
	6	6.05	$78.80/Re$
	8	6.49	$82.32/Re$
	∞	8.24	$96.00/Re$

13

For turbulent flow (Reynolds number greater than 4000), the Nusselt number for the glass channels and the recuperator channels are given by equation (2.9) (Gnielinski, 1976):

$$Nu = \frac{(f/8)(Re - 1000)Pr}{1 + 12.7(f/8)^{0.5}(Pr^{2/3} - 1)} \tag{2.9}$$

Note that the friction factor, f, in equation (2.9) was derived from the Petukhov equation for turbulent flow in smooth tubes, as shown in equation (2.10) (Petukhov, 1970):

$$f = (0.790 \ln(Re) - 1.64)^{-2} \tag{2.10}$$

2.3.2   Radiation

For receivers operating at temperatures marginally above ambient, radiation heat loss is important. However, for collectors operating at higher temperatures, radiation heat loss becomes dominant (Stine & Harrigan, 1985). The radiation heat loss is proportional to the emittance and the temperature difference of the surface under consideration. This is given by equation (2.11) (Stine & Harrigan, 1985):

$$\dot{Q}_{loss,rad} = \varepsilon\sigma A_r\left(T_r^4 - T_{sky}^4\right) \tag{2.11}$$

The designer of the solar receiver has some control over the terms in equation (2.11). These include the emittance of the surface of the receiver and the receiver's surface area. Surfaces that have low emittance generally have a low absorptance as well, thus reducing the absorbed solar energy. However, in recent years, a class of surface coatings has been developed, which is called selective coatings. These coatings have low values of emittance when the surface is at a low temperature but high values of absorptance for solar energy (Stine & Harrigan, 1985). To maximise the useful heat collected by a solar receiver, the receiver should have a high absorptance and a low emittance. However, radiation heat transfer theory states that the absorptance and emittance are equal – at least in an enclosure. However, for all surfaces, Kirchoff's law states that they are equal only for radiation at a specific wavelength, not as an average property integrated over a spectrum (Stine & Harrigan, 1985). Kirchoff's law is given by equation (2.12):

$$\alpha_\lambda = \varepsilon_\lambda \tag{2.12}$$

The subscripts in equation (2.12) indicate that this law only applies to properties in the same wavelength spectrum. Solar collectors absorb energy from a spectrum of a 6050 K blackbody

14

emitter with its peak intensity at a wavelength of about 0.48 µm. The spectrum of the energy emitted by the receiver is governed by the receiver's surface temperature, which is much less than the 6050 K of the blackbody emitter. As an example, for a receiver temperature of 80 °C, the peak intensity is at a wavelength of 8.21 µm (Stine & Harrigan, 1985). Thus, for a cavity receiver with a large aperture, Kirchoff's law is not applicable, because the radiation that is absorbed is at a different wavelength from that of the emitted radiation from the cavity receiver.

View factors are an important quantity when calculating the temperature profile of the glass surface. Some standard equations for view factors between two aligned parallel rectangles or between perpendicular rectangles with a common edge can be used from the textbook of Lienhard IV and Liendhard V (2020). The glass can be divided into smaller 'cells' to be able to obtain a temperature profile of the glass surface from the bottom to the top. Thus, each cell in the cavity will have a specific view factor to each of the other cells in the cavity. The view factors can be calculated by making use of the reciprocity, summation, symmetry and superposition rules as set out in Lienhard IV and Liendhard V (2020). However, when using a program such as *Octave* to calculate the view factors, it is much easier to code a single equation as a function of the specific rectangle's dimension to find the view factor. The relevant view factor correlations are presented in Appendix A.

2.3.3 Conduction

Conduction heat loss is often described in terms of a material constant, the thickness of the material and its cross-sectional area. The conduction heat loss equation is given by Stine and Harrigan (1985) as follows:

$$\dot{Q}_{loss,cond} = \frac{kA_s(T_s - T_a)}{\Delta x} \tag{2.13}$$

It is of great importance to ensure that the conduction heat loss is a minimum in solar receiver design. Flat-plate collectors are designed to have good insulation material (a low thermal conductivity) on the sides and the back and material that is thick enough (Stine & Harrigan, 1985). Rectangular receivers, such as the one considered in this work, have four sides as well as the top side of the receiver through which heat is conducted. According to Le Roux et al. (2014a), high-temperature ceramic fibre insulation can be used to insulate the receiver considered in this work. Equation (2.13) was modified by using the electrical analogy to find equation (2.14):

$$\dot{Q}_{loss,cond} = A(T_{s,ave} - T_\infty)/R_{total} \qquad (2.14)$$

$$R_{total} = \left(\frac{1}{h_{outer}} + \frac{t_{ins}}{k_{ins}}\right)$$

2.4 Solar receivers with glass covers

A standard solar receiver, whether it is a flat-plate, parabolic through or tubular solar receiver, is subject to convective, conductive and radiative heat transfer due to the high temperature of the receiver relative to the environment. A solution for minimising the heat losses from the receiver to the environment is to cover the aperture with a selective spectral material that is transparent to certain bands of light and opaque to infrared radiation. Glass is an excellent example of such a material.

2.4.1 Glass covers without cooling

Experiments by Too et al. (2017), in which a 250 kW$_{th}$ tubular cavity receiver was used with a window covering the receiver's aperture, showed an increase of about 17% in the receiver's thermal efficiency. The receiver reached maximum steady-state temperatures of about 900 °C (Too et al., 2017). Uhlig et al. (2014) investigated the performance impact of a window cover on the receiver of a hybrid combined cycle solar power plant. The cycle included a heliostat field, a tower receiver and a gas turbine, which was combined with a conventional steam Rankine cycle. The receiver was a cylindrical-shaped tubular cavity receiver, where the window was placed over the receiver aperture (Uhlig et al., 2014). The receiver saw temperatures of between 335 °C and 800 °C and it was found that the window cover did not only increase the efficiency of the cycle but also reduced the overall cost of electricity generation (Uhlig et al., 2014).

Cui et al. (2013) investigated the heat loss of a dish receiver with and without a quartz glass cover on the aperture. The receiver geometry is shown in Figure 2.3 where a 5 mm thick high-temperature quartz glass cover with a selective coating layer was installed over the aperture of the cavity. The receiver had copper tube coils that absorbed the solar radiation, with 20 mm thick opaque insulation on the outside of the receiver (Cui et al., 2013). The model that was considered by Cui et al. (2013) was a combination of natural laminar convection and radiation. The receiver was simulated using FLUENT 6.3 CFD software. Cui et al. (2013) found that, compared with an uncovered receiver, the glass cover largely reduced the convection and radiation heat losses.
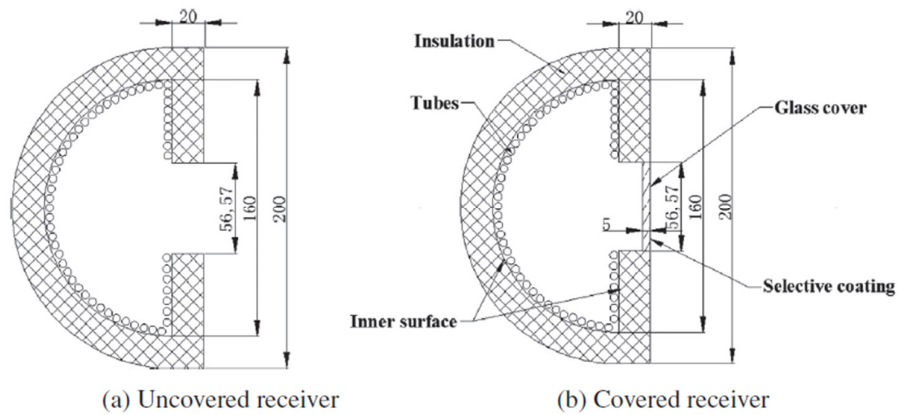
Figure 2.3 Schematic of cavity receiver with and without quartz glass cover (Cui et al., 2013)

The reduced losses are shown in Figure 2.4, which indicates the temperature contours for the uncovered and covered receivers. The covered receiver had a much higher temperature on the inside of the cavity than for the uncovered receiver, especially for inclination angles from 0° to 60°. The covered receiver's heat losses were about 36% less than those of the uncovered receiver (Cui et al., 2013). The results indicated that the orientation of the receiver had a great influence on the convection heat transfer. The radiation heat loss, which was the dominant heat loss component, was relatively constant at different receiver inclination angles. Cui et al. (2013) found that the radiation heat transfer from the receiver to the environment was significantly affected by the temperature and emissivity of the inner surface.
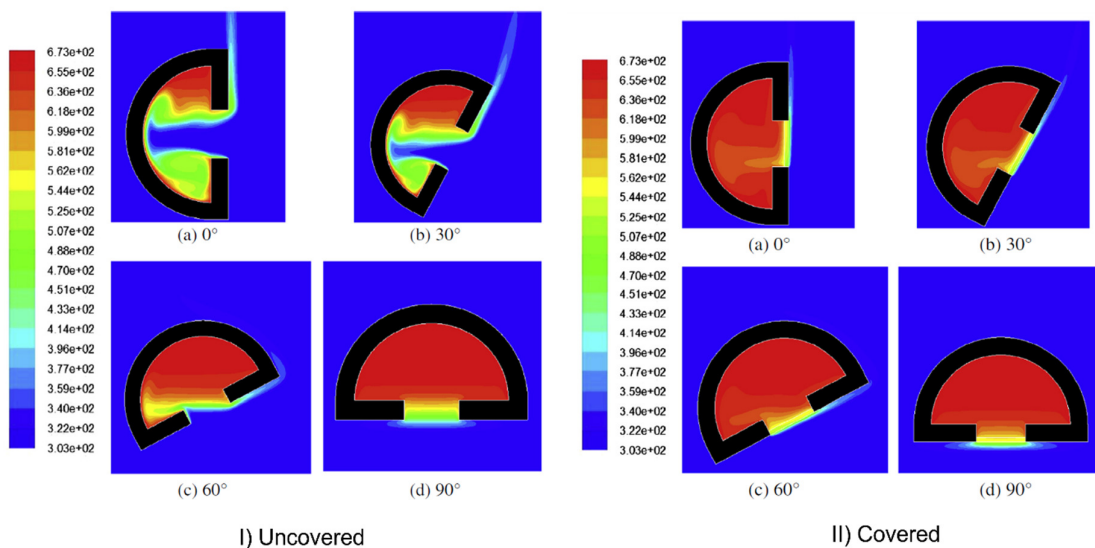
Figure 2.4 Temperature contours for different inclination angles of an uncovered and a covered receiver (Cui et al., 2013)

17
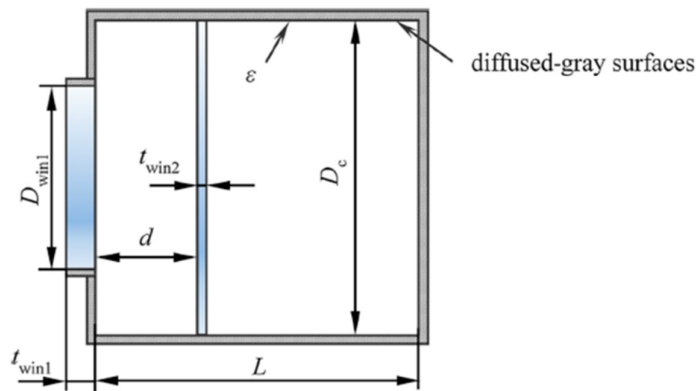
Figure 2.5 Double-glazing concept (Li et al., 2019)
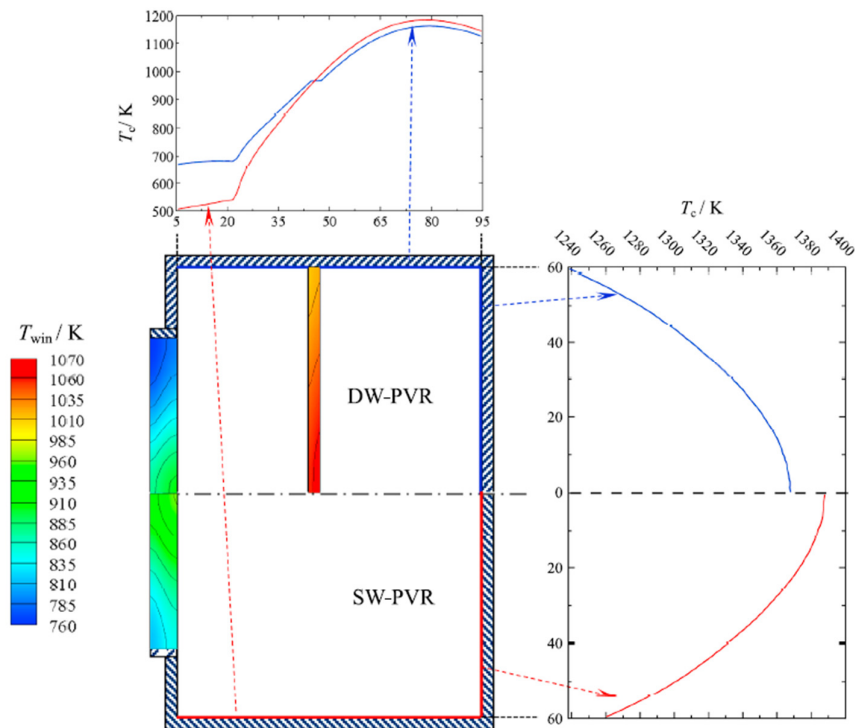
Figure 2.6 Comparison between temperature distribution of double-glazing and single-glazing receivers (Li et al., 2019)

A double-glazing solar receiver was investigated by Li et al. (2019). The authors employed a combination of the Monte Carlo ray-tracing and finite volume methods to evaluate the temperature profile, heat losses and efficiencies of the double-glazing solar receiver. A simplified model of the receiver is shown in Figure 2.5. Figure 2.6 shows a comparison of temperature distributions between the single-glazing and double-glazing concepts, as well as the cavity wall temperatures (Li et al., 2019). Due to a large proportion of re-radiative energy that was reflected from the inner window and absorbed by the outer window, the temperature

18

of the outer window was much lower in the double-glazing configuration than in the single-glazing configuration. The results showed that the total efficiency increased by increasing the cavity size, inner-window thickness, emissivity of the inner surface and distance between the windows (Li et al., 2019). Compared with a single-glazing receiver, the double-glazing receiver can have higher thermal efficiencies only for very specific cases. It is also shown that for the double-glazing receiver, the outer-window peak temperature is about 39 K to 83 K lower than that of the receiver with only one window. Therefore, there is some merit in designing a solar receiver with a double-glazing configuration.

It is thus clear that the efficiency of a typical tubular solar cavity receiver can benefit from a window-covered aperture. However, a glass cover can provide significant complications because the glass must withstand reradiation emitted by the high temperature of the receiver's walls. The glass must also endure highly concentrated solar irradiation, and therefore extreme temperatures, as well as high-pressure loads (Li et al., 2019). Various strategies have been put forward to ensure that the glass does not shatter or deform. These strategies include strengthening the glass by adopting specific curvatures of the glass or by reducing the glass temperature by cooling it with an HTF (Li et al., 2019). Alternative methods of minimising heat losses are to use a double-glazing configuration. However, these methods have not been well-researched and are more common with flat-plate solar collectors (Li et al., 2019).

2.4.2 Glass covers with cooling

Wang et al. (2016) experimentally and numerically investigated the thermal performance of a windowed volumetric solar receiver (WVSR). The concentrator used in their study consisted of a 16-mirror parabolic dish system driven by a two-axis tracking system. The window was placed directly in front of the cavity aperture and cooling air was pumped directly from the compressor. The receiver was composed of an absorber material, SiC ceramic foam, where the solar irradiation was concentrated on the solid matrix. The air that passed over the solid matrix was heated up through forced convection (see Figure 2.7) (Wang et al., 2016). Wang et al. (2016) discretised the governing equations by applying the finite volume method. The windowed cavity with the absorber was modelled in a coupled radiative-convection boundary condition. The numerical solutions were compared with three all-day experimental tests, where three samples with different pore structures and thicknesses were tested (Wang et al., 2016). Outlet air temperatures of greater than 1003 K and the best thermal efficiency (solar to thermal) of 63.1% at a receiver temperature of 1000 K were observed. The maximum deviations between

19

the experimental and theoretical results were 9.4% and 2.3% for the temperature of the back wall and the outlet air respectively. The thermal efficiency (solar-to-thermal) differed by a maximum of 5.35% between the experimental and theoretical results (Wang et al., 2016). Wang et al. (2016) concluded that their results showed that the model was feasible when describing the overall transport process from solar to thermal energy in a pressurised receiver.
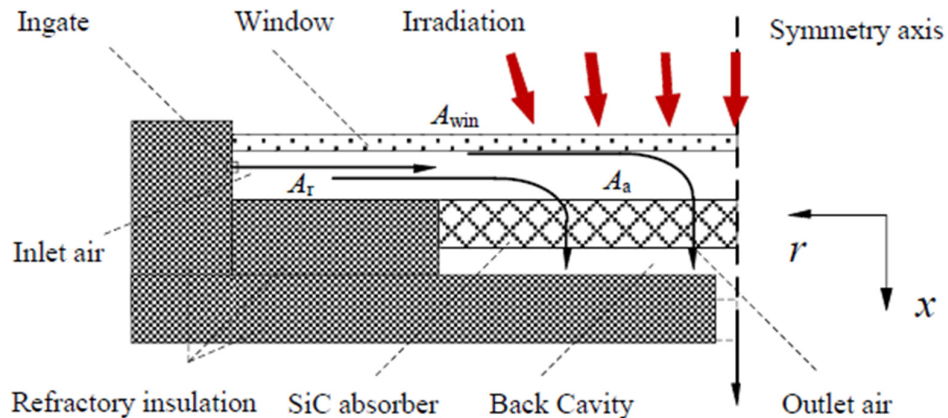
Figure 2.7 Schematic of the internal structure of the WVSR (Wang et al., 2016)

Research work was done by Uhlig and Röger (2004) in which cooling air was also used to cool the glass cover. However, there is a significant difference between the work of Uhlig and Röger (2004) and that of Wang et al. (2016). Uhlig and Röger (2004) investigated a dome-shaped pressurised volumetric receiver with an active cooling system in which the window was designed, simulated and experimentally tested. According to Uhlig and Röger (2004), to keep the glass temperature below 800 °C for quartz glass, a cooling heat flow of about 77 kW is necessary. Figure 2.8 shows the window concept with cooling proposed by Uhlig and Röger (2004). The cooling was achieved by having air flow between the two windows. The outlet of the cooling air was at the vertex of the dome and was mixed with the main flow to the receiver. The advantage of a cooling system such as this is that the cooling efficiency can be optimised by finding an optimal dimension of the outlet gap. Since the receiver operates at a pressure of 7 bar, the cooling flow must also be at the same pressure if it is to be mixed with the receiver flow (Uhlig & Röger, 2004). Thus, the cooling air is bled off directly after the compressors. The concept was first simplified and simulated with the ANSYS CFD package.

The goal of the study of Uhlig and Röger (2004) was to reach the highest cooling efficiency possible while maintaining an acceptable pressure drop with the smallest possible mass flow rate. It was found that a simple window with a cooling flow did not provide enough cooling to

20

keep the glass below 800 °C, as proposed by Uhlig and Röger (2004). The two windows reached maximum temperatures of 950 °C and 835 °C respectively, which was above the maximum temperature of 800 °C, as proposed by the designers. Uhlig and Röger (2004) proposed to introduce a swirl component to the flow passing over the glass using a specially designed inlet flange. This improved the amount of cooling of the glass, but the cooling was not close to the required 77 kW. The inlet flow temperature was then decreased further to about 70 °C, which allowed for cooling of about 80 kW (Uhlig & Röger, 2004).
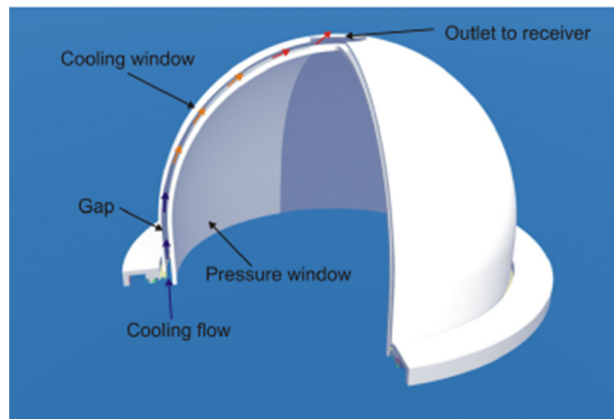
Figure 2.8 Dome-shaped cooling window concept (Uhlig & Röger, 2004)

Röger et al. (2006) modelled, tested and evaluated a high-temperature receiver with external multiple air-jet window cooling. This receiver window also had a concave shape and was made of fused silica, much the same as what was used in the work of Uhlig and Röger (2004). Röger et al. (2006) found that an asymmetric window-cooling design with pulsating air mass flow achieved suitable cooling of the window. Figure 2.9 shows the pressurised volumetric receiver with the concave window and how the window was cooled. A thermodynamic model of the receiver was developed, which included non-grey radiative, convective and conductive heat transfer, which was the basis of the window-cooling design. A solar test with no window was conducted to verify the thermodynamic model. Röger et al. (2006) conducted high-temperature testing with the window cooling in operation, where the temperature distribution on the quartz window and the absorber were determined by an infrared scanner that was specially developed. The simulations and experimental tests showed good agreement. With the multiple air-jet window cooling, the receiver had air outlet temperatures of more than 1000 °C, while the window temperatures were kept below 800 °C (Röger et al., 2006).
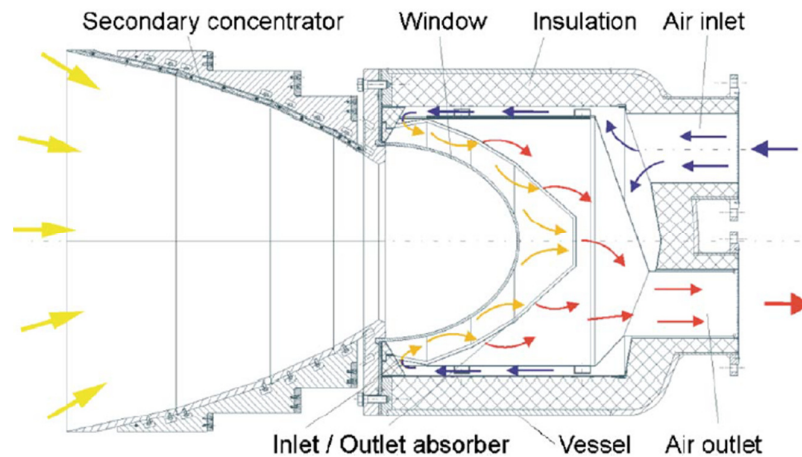
Figure 2.9 Pressurised volumetric receiver with concave window (Röger et al., 2006)

Another pressurised receiver with window cooling of note was developed by Karni et al. (1997). The directly irradiated annular pressurised receiver (DIAPR) was a volumetric, windowed cavity receiver, which operated at an aperture flux of up to 10 MW/m^2. This receiver had an innovative frustum-like high-pressure (FLHiP) window that was made of fused silica and was cooled by the working fluid before it entered the absorber (Karni et al., 1997). Karni et al. (1997) claimed that this window could withstand pressures of over 50 bar. Figure 2.10 shows the DIAPR that was developed and tested. The frustum shape of the window allowed for it to sustain such high pressures. The frustum shape also ensured that the tensile stresses did not develop at any possible working conditions and thus the window was subject only to compression stresses (Karni et al., 1997). Fused silica has a compression strength that is about 23 times higher than its tensile strength and the compression strength is about 2.5 times higher than that of carbon steel (Karni et al., 1997). Kribus (1994) shows through ray-tracing calculations that the reflection losses of a frustum-like window are only about 1% because several reflections are necessary for the incoming rays to escape. Figure 2.10 indicates that the window thickness (*t*) is only 2.25 mm and since fused silica is highly transparent to solar radiation, heat losses due to sunlight absorption are negligible. The DIAPR was put through about 250 hours of experimental tests and the absorber reached a temperature of about 1600 °C, while the window reached a maximum temperature of 600 °C (Karni et al., 1997). The FLHiP window has the added benefit of the prevention of dust accumulation on the inside of the receiver due to the low-pressure external air stream that flushes out any dust (Karni et al., 1997).

22
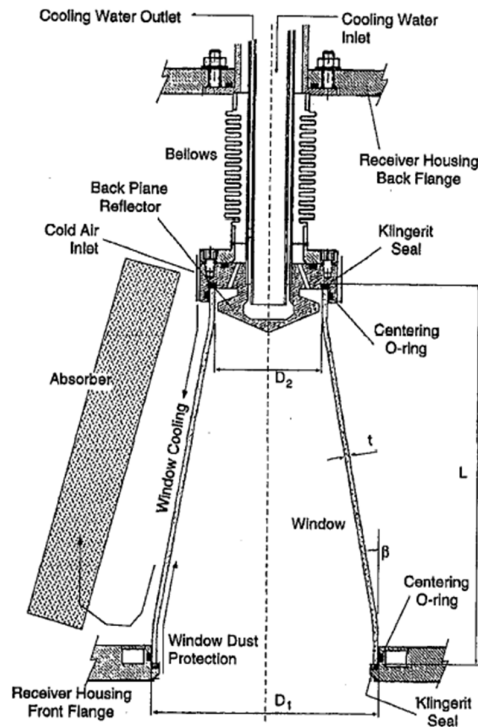
Figure 2.10 DIAPR with the FLHiP window (Karni et al., 1997)

2.5   Glass types and properties

Commercially available glass can be divided into a few major categories: vitreous silica, soda lime silica and borosilicate. Vitreous silica can be manufactured in such a way that it has a very small thermal expansion coefficient and very high working and melting temperatures. Commercial glass is often used in a wide range of applications and some of the most important properties that need to be considered by the end-user are the density, refractive index, thermal expansion coefficient, glass transformation temperature, strength, elastic modulus and chemical durability (Shelby & Lopes, 2005). The following sections provide some background to three different glass types, their properties, applications, and some examples of commercially available types of glass.

2.5.1   Vitreous silica

Vitreous silica is the only commercial glass that contains a single major chemical component and is often made directly from a naturally occurring mineral called quartz. Optical fibres and infrared transmitting equipment often use vitreous silica as the glass type of choice. This glass type is often praised for its very low thermal expansion coefficient, which allows its use at temperatures above 1000 °C (Shelby & Lopes, 2005). The thermal expansion coefficient of

23

vitreous silica is about 0.5 to 0.6 parts per million K^{-1} at room temperature and varies only slightly between 25 °C and 1000 °C (Shelby & Lopes, 2005). However, it must be noted that vitreous silica has some differences in its properties and most commercial glass products are thus designated by their trademark name. Therefore, it is not adequate to refer to a sheet of glass only as "vitreous silica" (Shelby & Lopes, 2005). Vitreous silica also goes by other names such as silica glass, fused silica, fused quartz or simply quartz. The latter is often undesirable to use because it can be confused with crystalline quartz, which is something entirely different in structure from vitreous silica (Bansal & Doremus, 1986).

2.5.2 Soda lime silica

Soda lime silica is produced in larger quantities than vitreous silica. Soda lime silica is often used for flat glass applications such as mirrors, residential and automotive windows and container and incandescent lamp glass (Shelby & Lopes, 2005). Vitreous silica might have many properties that make it desirable for applications such as flat, container or lamp glass; however, it has a very high melting temperature (more than 2 000 °C). This very high melting temperature has a high cost linked to it and thus vitreous silica is not often used for the more common consumer products (Shelby & Lopes, 2005). Hence the development of soda lime silica is based on a compromise between the outstanding properties of pure silica, and the cost of producing large quantities of glass required for windows, containers and electrical lighting. Soda is added to the silica, which results in a large decrease in the melting temperature; however, this leads to poor chemical durability of the glass (Shelby & Lopes, 2005). Therefore, a portion of the soda is replaced by lime (CaO), which partially increases the chemical durability and results in a glass with a reasonable melting temperature (of about 1500 °C), while maintaining acceptable properties for consumer applications. Soda lime silica has a glass transformation temperature of about 550 °C to 580 °C, significantly lower than that of the vitreous silica glass type (Shelby & Lopes, 2005). The thermal expansion coefficient is about 8 to 9 parts per million K^{-1}. This lower transition temperature and higher thermal expansion coefficient restrict the soda lime silica glass for use in cases where a thermal shock is unlikely to occur, but it reduces the cost of production.

2.5.3 Borosilicate

Borosilicate glass is produced for specialised applications where it is recognised for its excellent resistance to thermal shocks and high physical robustness. It is used in laboratory ware, televisions and cookware. Many other glass types are produced in very limited numbers for

extremely specialised applications such as optical, electronic and biological applications (Shelby & Lopes, 2005). The borosilicate glass type has a much better thermal shock resistance due to its much lower thermal expansion coefficient. The thermal expansion coefficient of borosilicate glass lies in-between that of vitreous silica and that of soda lime silica. Borosilicate glass is clear and colourless, with almost no detectable visible light scattering (Shelby & Lopes, 2005). Other types of borosilicate glass are homogeneous with much higher alumina concentrations. These types of glass are based on the alkaline earth borosilicate system instead of the sodium borosilicate system. Consequently, this glass has a higher index of refraction and higher chemical and electrical resistivities (Shelby & Lopes, 2005). A typical thermal expansion coefficient of borosilicate is about 3.2 parts per million K^{-1}. Borosilicate has a glass transformation temperature of greater than 600 °C.

2.5.4 Examples of commercial glass

A specific patented glass for high-temperature applications manufactured by Schott in Germany is called Robax. This glass type does not require special manufacturing processes and is commercially available in 3 mm and 5 mm thicknesses. Common applications for this glass are fireplace windows and doors, heat insulators, oven/boiler inspection windows and outdoor lighting. This glass has a smaller thermal expansion coefficient than that of borosilicate and is about the same as that of vitreous silica at about 0.5 parts per million K^{-1}. Robax also has a relatively large working temperature range from about -240 °C to about 800 °C (Schott, 2021). These temperature ranges are often subject to loading time restrictions. More specifically, the Robax line-up can handle up to 610 °C for about 1000 hours of continuous temperature loading (Schott, 2021). It must be noted that the temperature refers to the hottest point on the outside of the glass and thermal gradients and shock have been considered. Figure 2.11 shows the transmission coefficient versus different wavelengths for Robax. Thermal radiation falls in the 0.1 µm to 1000 µm range. This includes UV light, near infrared radiation and visible light, with solar radiation falling in the 0.3 µm to 3 µm range (Lienhard IV & Liendhard V, 2020). Figure 2.11 indicates that the glass can transmit wavelengths of between 0.3 µm and 2.5 µm almost completely, meaning the glass will transmit solar radiation. However, in the 3 µm to 5 µm range, the transmissivity of the glass drops to about half of what it is in the 0.3 µm to 2.5 µm range, with some wavelengths having nearly zero transmission. This means that the glass is almost opaque to infrared radiation, but as Figure 2.11 indicates, the transmissivity in the infrared wavelength range depends on the glass thickness.
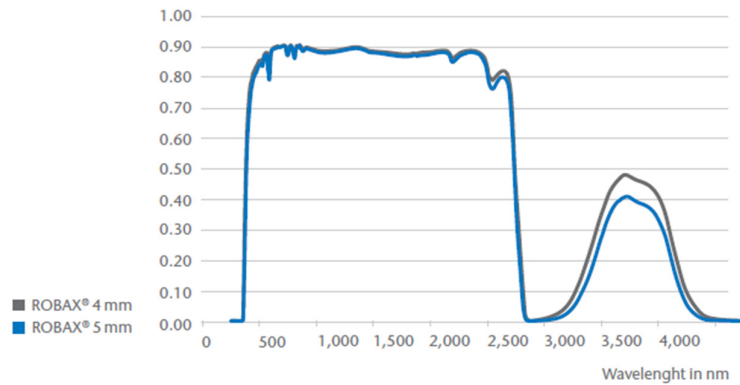
Figure 2.11 Transmission properties of Robax (Schott, 2021)

Another glass that is made by Schott is called Nextrema and is made specifically for high-temperature applications. The glass is manufactured in sheets and can be further processed by a wide variety of technologies to fit client requirements, such as surface smoothing, polishing or coating (Schott, 2014). Due to the careful manufacturing process, the glass can be made to conform to the client's specific requirements. Nextrema is specifically designed with a complex microstructure to achieve a near-zero thermal expansion, which gives it excellent thermal strength and heat resistance (Schott, 2014). The technical brochure of the glass from Schott (2014) claims robustness at high operating temperatures of up to 950 °C and high thermal shock resistance of up to 800 °C. Figure 2.12 shows the wide transmittance spectrum of different Nextrema variants. The glass has a high transmittance (almost 90%) in the solar radiation spectrum (300 nm – 3000 nm) and a lower transmittance in the thermal radiation range (> 3000 nm). This glass will perform well in the solar environment. The technical brochure from Schott (2014) lists it as one of the applications of glass.
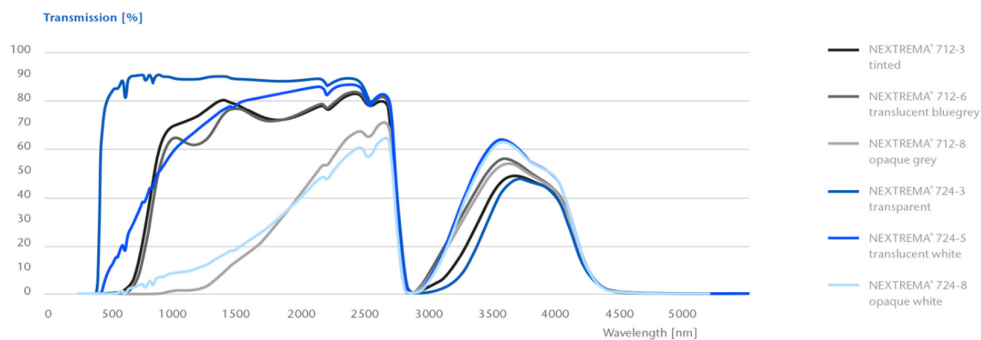
Figure 2.12 Transmission values of different Nextrema variants (Schott, 2014)

A few other commercial types of glass that are designed for high-temperature applications are produced by Glass Dynamics LLC (2015) in the USA. Corning Pyrex 7740 glass is a low

26

thermal expansion borosilicate glass, which is often used for fireplace glass, high-temperature light lenses and ovens. The working temperature of Pyrex 7740 ranges from 230 °C to 490 °C and the glass can withstand thermal shocks of up to 160 °C (Glass Dynamics LLC, 2015). Another Corning trademark glass for high-temperature applications is called Pyroceram 9963. This glass is also used for wood-burning stove windows, oven or boiler windows, cooking tops and other high-temperature appliances. Pyroceram 9963 has a much higher working temperature than that of Pyrex 7740 at about 704 °C to 775 °C with a thermal shock resistance of up to 700 °C. Figure 2.13 shows the transmission curve for Pyroceram 9963, which shows an excellent transmission in the solar radiation spectrum and low transmission in the thermal radiation spectrum (Glass Dynamics LLC, 2015).
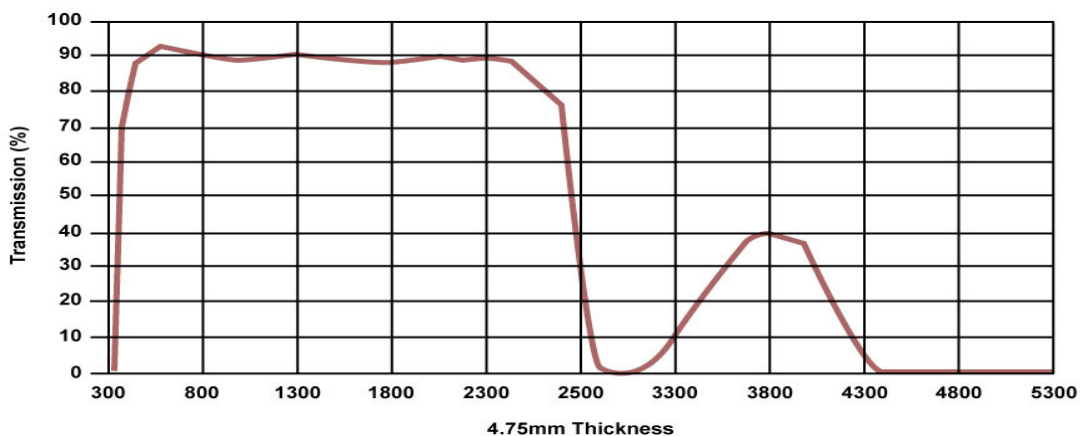
Figure 2.13 Transmission curve for 4.75 mm thick Pyroceram 9963 glass (Glass Dynamics LLC, 2015)

Glass Dynamics LLC (2015) also produces four different types of quartz glass: Dynasil IRQ, Dynasil Low OH IR, GE214 fused quartz and optical homogeneity fused silica. These types of glass have working temperatures in the range of 926 °C to 1204 °C along with very low thermal expansion coefficients in the range of 0.5 parts per million K^{-1}. Corning's high-temperature, high-silica quartz glass is called Vycor and is also produced by Glass Dynamics LLC (2015). It has almost the same working temperature range as the previously mentioned types of quartz glass and can be produced in thicknesses of 3 mm up to 20 mm (Glass Dynamics LLC, 2015).

2.5.5   Summary

Table 2.2 provides a summary of the glass properties for the different glass types. The vitreous silica glass type has the lowest thermal expansion coefficient and refractive index as well as the highest glass transformation temperature.

Table 2.2 Summary of properties of three glass types (Shelby & Lopes, 2005)

Property	Vitreous silica	Borosilicate (7070 - electrical)	Soda lime silicate (windows)
Density (g/cm^3)	2.197	2.13	2.53
Refractive index	1.457	1.469	1.520
Thermal expansion coefficient (parts per million K^{-1})	0.6	3.2	9.5
Glass transformation temperature (°C)	1050 – 1200	> 600	550 - 580

Table 2.3 also summarises the properties of different types of commercial glass that are available. Dynasil IRQ and Vycor have the highest operating temperature range, but these two types of glass have the highest thermal expansion of all the commercial glass types considered. One must thus consider all the properties of the glass at the same time when deciding on which glass to use. Pyroceram 9963 has a working temperature limit of 775 °C with a very low thermal expansion and a high thermal shock resistance. Nextrema also has a high working temperature limit and thermal shock resistance temperature with a low thermal expansion coefficient. Vitreous silica, also known as fused silica or quartz, is often used as a window cover on solar-dish receivers. For example, Li et al. (2019) used a fused silica window, which was treated as a homogeneous emitting and absorbing material in their CFD simulation. Cui et al. (2013) simulated a 5 mm thick high-temperature resistant quartz glass cover, which was treated with a selective coating layer. Wang et al. (2016) also used a quartz glass cover, which had a limiting operating temperature of 1 400 K (1127 °C) and was cooled by bleed air.

Table 2.3 Summary of properties of different commercial glass types (Glass Dynamics LLC, 2015, Schott, 2014)

	Robax	Nextrema	Pyrex 7740	Pyroceram 9963	Dynasil IRQ	Vycor
Working temperature (°C)	-240 to 800	Up to 950	230 - 490	704 - 775	926 - 1204	926 - 1204
Thermal expansion coefficient (parts per million K^{-1})	± 0.05	0.04 - 0.16	0.325	0.03	5	5
Thermal shock resistance (°C)	700	600 - 820	160 (3.2 mm)	700 (3 mm)	-	-

2.6   Summary of literature study

Based on the many existing convection heat loss models, the Koenig and Marvin and Paitoonsurikarn and Lovegrove models were the most suitable for this study. The Koenig and Marvin model was verified by McDonald (1995). The Paitoonsurikarn and Lovegrove model was validated against experimental results by Paitoonsurikarn and Lovegrove (2006). The Paitoonsurikarn and Lovegrove model proved to be much more accurate and easier to implement than the Koenig and Marvin model. Therefore, the Paitoonsurikarn and Lovegrove model was used in this study.

The literature on solar receivers with glass covers indicates that a window proves to be quite successful in minimising the convection and radiation heat losses from a solar receiver. Furthermore, cooling the glass with air flow improves the longevity of the glass and can also lead to further reductions in solar receiver heat losses and increases in solar-to-mechanical efficiencies (Uhlig & Röger, 2004, Wang et al., 2016). However, there is no existing solar receiver study that has a glass window on the inside of the receiver cavity.

Considering the different commercial glass types in existence, borosilicate and vitreous silica are the two types that have the potential to perform well in a high-temperature environment. Borosilicate and vitreous silica both have very low thermal expansion coefficients, 3.2 and 0.6 parts per million K^{-1} respectively (Shelby & Lopes, 2005). Vitreous silica will handle the higher temperatures better because its thermal expansion coefficient is much lower and its transition temperature is in the 1000 °C range. There are also a few commercial vitreous silica (or quartz) glass types that are suitable for this high-temperature and high-thermal stress application. More specifically, Robax or Nextrema manufactured by Schott or Pyroceram 9963 manufactured by Glass Dynamics would also be suitable for use as a window cover on a solar receiver.

Chapter 3

Methodology

3.1   Introduction

The relevant entropy generation equations for each part of the cycle are described fully in this chapter. With these equations, an exergy analysis provides the net power output, entropy generation and the solar-to-mechanical efficiency of the cycle, thus analysing the impact of the cooling window on the performance of the cycle. Next, the receiver and window models are discussed based on the relevant reviewed literature. A summary of the recuperator geometry leads to the variables and parameters that make up the objective function of the study. The objective function depended on initial assumptions, constraints and constants. Finally, a dedicated subsection presents the numerical methods used to solve the cooling window's surface temperature and heat transfer rate. Note that parts of this chapter used the methodology and code of Le Roux and Sciacovelli (2019) as a base to allow for a direct comparison of the results.

3.2   Entropy generation in the solar-dish Brayton cycle components

Five components contribute to the entropy generation in the cycle, namely the turbine, compressor, solar collector (receiver), recuperator and window. Equation (3.1) (second law of thermodynamics) shows the change of entropy in a control mass for an irreversible process (Borgnakke & Sonntag, 2014). When an energy and entropy balance is done on either a control volume or a control mass, the energy is conserved but not the entropy, which is due to heat transfer and having an irreversible process. The total entropy increases and is not conserved, which is true for all irreversible processes. The total entropy must increase by the sum of all the entropy generation terms and it must be positive or at least zero for any conceivable process (Borgnakke & Sonntag, 2014). Equation (3.2) expresses the entropy change of an ideal gas as a function of the pressure and temperature ratio, which can be used with constant specific heat and the ideal gas constant. Equation (3.3) shows the entropy balance equations for a control volume (Borgnakke & Sonntag, 2014):

$$S_2 - S_1 = \int_1^2 \frac{\delta Q}{T} + S_{gen} \tag{3.1}$$

$$s_2 - s_1 = c_{p0} \ln \frac{T_2}{T1} - R \ln \frac{P_2}{P_1} \tag{3.2}$$

$$\frac{dS_{cv}}{dt} = \sum \dot{m}_i\, s_i - \sum \dot{m}_e\, s_e + \sum \frac{\dot{Q}_{cv}}{T} + \dot{S}_{gen} \tag{3.3}$$

The above equations could then be used to derive the entropy generation rate of each of the five components in the cycle at a steady state. Figure 1.3 indicates the state numbers in the entropy generation rate equations in the following sections.

3.2.1 Turbine and compressor

Equation (3.2) and equation (3.3) were used to derive the entropy generation rates for the compressor and turbine. These relations are expressed in terms of the pressures and temperatures, which could be described by the isentropic efficiencies (Le Roux, 2011). Equation (3.4) and equation (3.5) show the entropy generation rates for the turbine and the compressor respectively:

$$\dot{S}_{gen,c} = \dot{m}c_{p0} \ln\frac{T_2}{T_1} - \dot{m}R \ln\frac{P_2}{P_1} \tag{3.4}$$

$$\dot{S}_{gen,t} = \dot{m}c_{p0} \ln\frac{T_8}{T_7} - \dot{m}R \ln\frac{P_8}{P_7} \tag{3.5}$$

3.2.2 Solar receiver and window

Equation (3.6) and equation (3.7) express the entropy generation rate of the solar receiver and the window for an ideal gas working fluid. Again, equation (3.2) and equation (3.3) were used to derive these equations. The symbol, $\dot{Q}^*_{rec}$, is the rate of heat transfer from the sun's apparent temperature as an exergy source, T^*. The apparent sun temperature as an exergy source is about 75% of the apparent blackbody temperature of the sun, which is about 6000 K (Le Roux, 2011). Therefore, T^* was considered to be close to 4 500 K (Bejan, 1982) and was used as such in this research study.

$$\dot{S}_{gen,rec} = -\frac{\dot{Q}^*_{rec}}{T^*} + \frac{\dot{Q}_{loss,cond,rec}}{T_\infty} + \frac{\dot{Q}_{loss,rad,rec}}{T_s} + \frac{\dot{Q}_{loss,conv,rec}}{T_s} + \dot{m}c_{p0} \ln\frac{T_6}{T_5} \\ - \dot{m}R \ln\frac{P_6}{P_5} \tag{3.6}$$

$$\dot{S}_{gen,win} = -\frac{\dot{Q}^*_{win}}{T^*} - \frac{\dot{Q}_{gain}}{T_s} + \frac{\dot{Q}_{loss,win}}{T_\infty} + \dot{m}c_{p0} \ln\frac{T_3}{T_2} - \dot{m}R \ln\frac{P_3}{P_2} \tag{3.7}$$

With the proposed concept of having the window on the inside of the receiver, parallel to the receiver walls, the radiation and convection heat losses from the receiver would be absorbed by the window. Thus, $\dot{Q}_{loss,rad.rec}$ and $\dot{Q}_{loss,conv,rec}$ are included in the $\dot{Q}_{gain}$ term in equation (3.8):

$$\dot{Q}_{gain} = \dot{Q}_{loss,rad.rec} + \dot{Q}_{loss,conv,rec} \tag{3.8}$$

This means that when the total entropy generation rate was calculated, the $\dot{Q}_{loss,rad.rec}$ and

31

$\dot{Q}_{loss,conv,rec}$ terms in equation (3.6) would cancel out.

3.2.3 Recuperator

The entropy generation rate of the recuperator was derived from equation (3.2) and equation (3.3) and is given by equation (3.9) (Le Roux & Sciacovelli, 2019):

$$\dot{S}_{gen} = \dot{m}c_{p0}\ln\left[\frac{T_{10}T_4}{T_9T_3}\left(\frac{P_{10}P_4}{P_9P_3}\right)^{-R/c_{p0}}\right] + \frac{\dot{Q}_{loss,reg}}{T_\infty} \tag{3.9}$$

In equation (3.9), T_9 to T_{10} is the hot stream and T_3 to T_4 is the cold stream in the recuperator (heat exchanger).

3.3 Exergy analysis for the cycle

When solar radiation is concentrated, mechanical power can be generated with the solar-dish Brayton cycle. Considering Figure 1.3, $\dot{Q}^*$ represents the solar heat input, or in other words, the intercepted solar heat input power that is concentrated by the parabolic dish. Figure 1.3 also shows the control volume around the cycle. This control volume, along with the assumption that the cycle is run at a steady state, can be used to determine where exergy is crossing the boundary.

It was assumed that $V_1 = V_{11}$ and $z_1 = z_{11}$ and an exergy analysis was conducted for the system. It is important to note that $T_1 \neq T_{11}$ but $P_1 = P_{11}$ since the cycle is an open cycle. The two temperatures (at the exit of the cycle) were taken to be the same ($T_{10} = T_{11}$) because it was assumed that the control volume boundary was very close to the hot stream exit of the recuperator (Le Roux, 2011, Le Roux & Sciacovelli, 2019). Borgnakke and Sonntag (2014) provide the exergy rate equation, which is shown in equation (3.10):

$$\frac{d\Phi}{dt} = \sum\left(1 - \frac{T_0}{T}\right)\dot{Q}_{c.v.} - \dot{W}_{c.v.} + P_0\frac{dV}{dt} + \sum\dot{m}_i\psi_i - \sum\dot{m}_e\psi_e - T_0\dot{S}_{gen} \tag{3.10}$$

Due to the steady-state assumption and only one inlet and outlet, equation (3.10) was rewritten and equation (3.11) was derived:

$$T_0\dot{S}_{gen} = \dot{m}[h_i - h_e - T_0(s_i - s_e)] + \left(1 - \frac{T_0}{T^*}\right)\dot{Q}^* - \dot{W}_{net} \tag{3.11}$$

When equation (3.11) was rearranged to make the net power output the object of the equation and by assuming constant specific heat and ideal gas, equation (3.12) was derived:

$$\dot{W}_{net} = -T_0\dot{S}_{gen} + \left(1 - \frac{T_0}{T^*}\right)\dot{Q}^* + \dot{m}c_{p0}\ln(T_1 - T_{11}) - \dot{m}T_0 c_{p0}\ln\left(\frac{T_1}{T_{11}}\right) \tag{3.12}$$

The internal entropy generation rate of the system could be written in terms of the sum of all the entropy generation rates of each component and the ducts in the system (Le Roux, 2011). The entropy generation in the ducts of the system was also calculated by equation (3.2) and equation (3.3). The total internal entropy generation rate was then expressed from Section 3.2, as shown in equation (3.13):

$$
\begin{aligned}
\dot{S}_{gen} = &\left[-\dot{m}c_{p0}\ln\left(\frac{T_1}{T_2}\right) + \dot{m}R\ln\left(\frac{P_1}{P_2}\right)\right]_{compressor} \\
&+ \left[\dot{m}c_{p0}\,ln\left[\frac{T_{10}T_4}{T_9 T_3}\left(\frac{P_{10}P_4}{P_9 P_3}\right)^{-\frac{R}{c_{p0}}}\right] + \frac{\dot{Q}_{loss,reg}}{T_\infty}\right]_{recuperator} \\
&+ \left[-\frac{\dot{Q}^*_{rec}}{T^*} + \frac{\dot{Q}_{loss,cond,rec}}{T_\infty} + \dot{m}c_{p0}\,ln\left(\frac{T_6}{T_5}\right) - \dot{m}R\,ln\left(\frac{P_6}{P_5}\right)\right]_{receiver} \\
&+ \left[-\dot{m}c_{p0}\,ln\left(\frac{T_7}{T_8}\right) + \dot{m}R\,ln\left(\frac{P_7}{P_8}\right)\right]_{turbine} \\
&+ \left[-\dot{m}c_{p0}\ln\left(\frac{T_2}{T_3}\right) + \dot{m}R\,ln\left(\frac{P_2}{P_3}\right) + \frac{\dot{Q}_{loss,win}}{T_\infty} - \frac{\dot{Q}^*_{win}}{T^*}\right]_{window} \\
&+ \left[-\dot{m}c_{p0}\,ln\left(\frac{T_4}{T_5}\right) + \dot{m}R\,ln\left(\frac{P_4}{P_5}\right) + \frac{\dot{Q}_{loss,4-5}}{T_\infty}\right]_{duct\,4-5} \\
&+ \left[-\dot{m}c_{p0}\,ln\left(\frac{T_6}{T_7}\right) + \dot{m}R\,ln\left(\frac{P_6}{P_7}\right) + \frac{\dot{Q}_{loss,6-7}}{T_\infty}\right]_{duct\,6-7} \\
&+ \left[-\dot{m}c_{p0}\,ln\left(\frac{T_8}{T_9}\right) + \dot{m}R\,ln\left(\frac{P_8}{P_9}\right) + \frac{\dot{Q}_{loss,8-9}}{T_\infty}\right]_{duct\,8-9}
\end{aligned}
\tag{3.13}
$$

Equation (3.13) was then substituted into equation (3.12) to find the net power output of the solar-dish Brayton cycle as a function of the entropy generation rate of each component in the cycle as well the temperatures and pressures. The combination of equation (3.12) and equation (3.13) led to the net power output, which would be useful in comparing the cycle with the window to the cycle without the window (see Le Roux and Sciacovelli (2019)).

3.4 Receiver and window modelling

The receiver phase-change temperature, chosen turbocharger, turbocharger operating point, and the cooling channel width were parameters in the study, while the recuperator dimensions were chosen to be variables. The dimensions of the open-cavity tubular solar receiver stayed constant in the analysis and are the same as in the study by Le Roux and Sciacovelli (2019).

33

3.4.1 SolTrace model

SolTrace can model CSP systems using Monte Carlo ray-tracing methodologies (Wendelin et al., 2013). SolTrace has a fast and powerful script engine that allows the user to automate the code and run multiple different geometries, sun definitions, or optical properties (Wendelin et al., 2013). The script was written in such a way that when the dish size was changed, the receiver position relative to the solar dish would be adjusted accordingly to have the parabolic dish's focal point on the receiver with minimal spillage (see Appendix C for the code). A pillbox sunshape was assumed with the parameter for the pillbox chosen as the half-angle width of 4.65 mrad. The cavity walls were modelled as oxidised stainless steel with an assumed reflectance of 15% (Le Roux et al., 2014a). The glass panes had an assumed reflectivity of 8%, transmissivity of 86% and absorptivity of 6% for solar radiation (Çengel & Ghajar, 2015). Each of the glass panes was modelled with a refraction index of 1.5 and a thickness of 3 mm, each with an air entity on both sides with a refraction index of 1 (see Figure 3.1). This was done to capture the refraction of light as it travelled through the glass, as recommended by Wendelin et al. (2013).
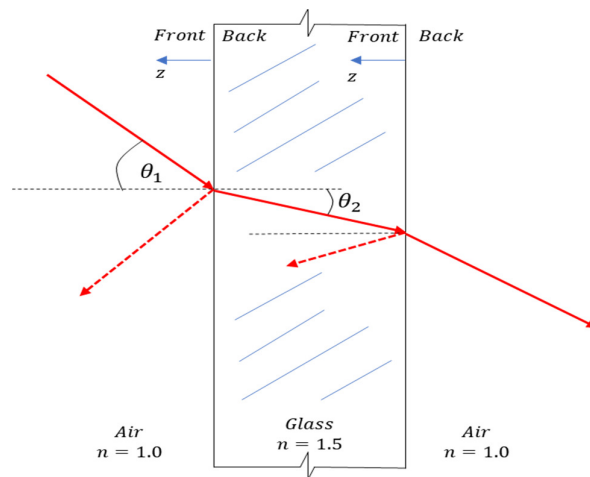
Figure 3.1 Glass elements to be modelled in SolTrace (Wendelin et al., 2013)

The dish surface was modelled as having a reflectivity of 85%, a rim angle of 45° and both a specularity and slope error of 2 mrad. Since SolTrace uses ray tracing to compute heat flux, more sunrays mean increased accuracy of the solutions and therefore 1 million sunrays were used with a seed value of '123' throughout the simulations. Figure 3.2 shows an example of some of the SolTrace analysis results.
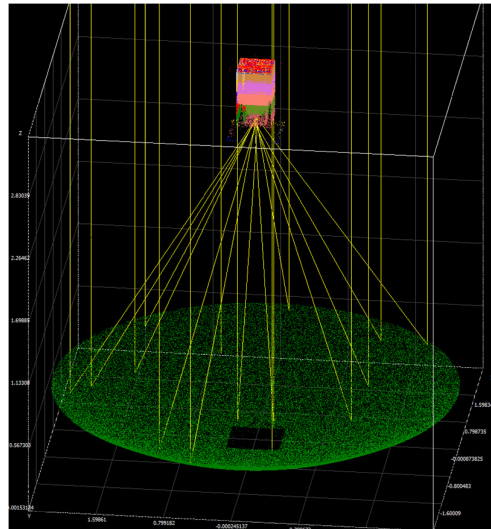
Figure 3.2 SolTrace analysis with paths of rays

3.4.2 Receiver modelling

Figure 3.3 shows a zoomed-in view of a cross-section of the receiver with the window cooling channel. The heat losses from the receiver included radiation, convection and conduction heat losses and the net heat transfer on the receiver was defined by equation (3.14). Figure 3.3 indicates that the radiation and convection heat losses from the receiver were absorbed by the window and are included as such in the window model. The aperture area of the receiver was fixed at 0.25 m × 0.25 m and the inner diameter of the receiver coil (surrounded by phase-change material) was 0.0833 m.

$$\dot{Q}_{net,rec} = \dot{Q}^*_{rec} - \dot{Q}_{loss,cond,rec} - \dot{Q}_{loss,conv,rec} - \dot{Q}_{loss,rad,rec} \tag{3.14}$$
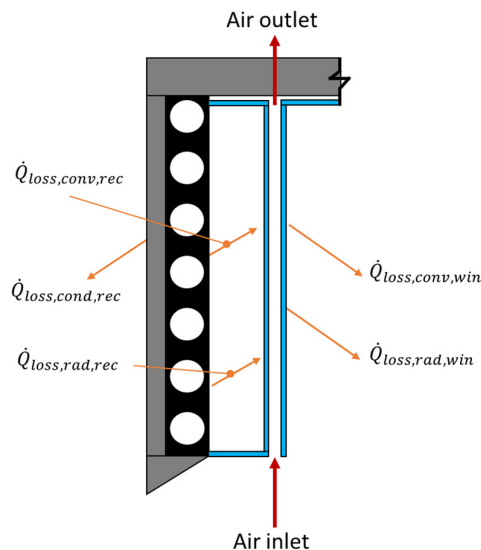
Figure 3.3 Receiver heat losses

35

3.4.2.1 Radiation heat transfer

Equation (3.15) is a modified form of equation (2.11), which was used to calculate the radiation heat losses from the receiver to the window. The radiation heat loss rate from the receiver depended on the emissivity of the receiver wall. The emissivity of the inner-cavity wall was assumed to be 0.7 for oxidised stainless steel at 1000 K (Le Roux & Sciacovelli, 2019). However, since the receiver wall was insulated with a phase-change thermal storage material, an effective emissivity had to be used and equation (3.16) was used to calculate the effective emissivity (Jilte et al., 2013). Since the window was parallel to the inner-cavity wall, the view factor of the receiver wall to the window was equal to 1, due to the window absorbing almost all of the radiation from the receiver wall.

$$\dot{Q}_{loss,rad,rec} = \varepsilon_{eff} A_{win} \sigma \left(T_{s,rec}^4 - T_{s,win}^4 \right) \tag{3.15}$$

$$\varepsilon_{eff} = \frac{1}{1 + \left(\dfrac{1 - \varepsilon_{wall}}{\varepsilon_{wall}} \right) \dfrac{A_{glass}}{A_{wall}}} \tag{3.16}$$

3.4.2.2 Convection heat transfer

The space between the inner-cavity wall and the window was considered to be an enclosure and the convection heat transfer in the enclosure depended on the aspect ratio and Rayleigh number of the enclosure. In CFD simulations by Pendyala et al. (2015), the authors developed Nusselt number correlations which are applicable to air as HTF and are given by equation (3.17):

$$Nu = 1.46 \times 10^{-5} (AR)^{0.19} (\ln(Ra))^{3.228} \tag{3.17}$$

The Nusselt number that was calculated by equation (3.17) was used in the standard equation of the Nusselt number (equation (2.3)) to find the heat transfer coefficient in the enclosure, called h_{enc} in equation (3.18). The convection heat loss from the inner-cavity wall to the window was then calculated by equation (3.18):

$$\dot{Q}_{loss,conv,rec} = h_{enc} A_{wall} \left(T_{s,rec} - T_{s,win} \right) \tag{3.18}$$

3.4.2.3 Conduction heat transfer

The conduction heat losses from the receiver to the environment were calculated as suggested by Le Roux et al. (2014a), in which work the authors used high-temperature ceramic fibre insulation with a thickness of 0.1 m and an average insulation conductivity of 0.061 W/mK at 550 °C. Equation (2.14) was used to calculate the conduction heat losses. Le Roux et al. (2014a) assumed an average wind speed of 2.5 m/s and an average receiver inclination angle of 45°. A combination of natural and forced

convection Nusselt number equations were used to calculate the heat transfer coefficient on the outside of the receiver. From these Nusselt number equations, in the range of receiver apertures of up to 2 m and assuming an average heat transfer coefficient across the whole receiver, Le Roux et al. (2014a) found that the total resistance of the insulation (R_{total} in equation (2.14)) could be approximated as $(1/h_{outer} + t_{ins}/k_{ins}) \approx 1.86 \ m^2 K/W$.

3.4.2.4 Pressure drop in coiled tube

The pressure drop in a circular pipe is given by equation (3.19):

$$\Delta P = f \frac{L}{D} \frac{\rho_f V_{avg}^2}{2} \tag{3.19}$$

In addition to the Moody-type friction losses that are computed for the length of the pipe, there are other losses such as bends in the pipe. White (2017) suggests adding a dimensionless loss coefficient, K, to equation (3.19). Therefore, Equation (3.20) presents a more applicable form of equation (3.19):

$$\Delta P = \frac{8\dot{m}^2}{\rho_f \pi^2 d^4} \left(f \frac{L}{D} + \sum_y K_y \right) \tag{3.20}$$

The friction factor, f, in equation (3.20) was calculated with the Colebrook equation for turbulent flow in a rough stainless steel tube and the K-values could be found for the specific tube diameter that is used (White, 2017).

3.4.3 **Window modelling**

Each of the four sides of the cooling channels was divided into sections and the temperature and heat transfer on each of the sections were calculated using a similar methodology as Le Roux et al. (2014a). The receiver and the glass window were modelled using the first law of thermodynamics. Figure 3.4 shows the main heat losses from the glass window that were considered in this study as well as the proposed arrangement of the glass-cooling channels. The net heat transfer rate at the glass window is given by equation (3.21):

$$\dot{Q}_{net,win} = \dot{Q}_{win}^* + \dot{Q}_{gain} - \dot{Q}_{loss,rad,win} - \dot{Q}_{loss,conv,win} \tag{3.21}$$

Note that $\dot{Q}_{gain} = \dot{Q}_{loss,rad,rec} + \dot{Q}_{loss,conv,rec,}$ which represents the heat gain on the window from the inner-receiver wall, while $\dot{Q}_{win}^*$ represents the absorbed solar heat as found from SolTrace.
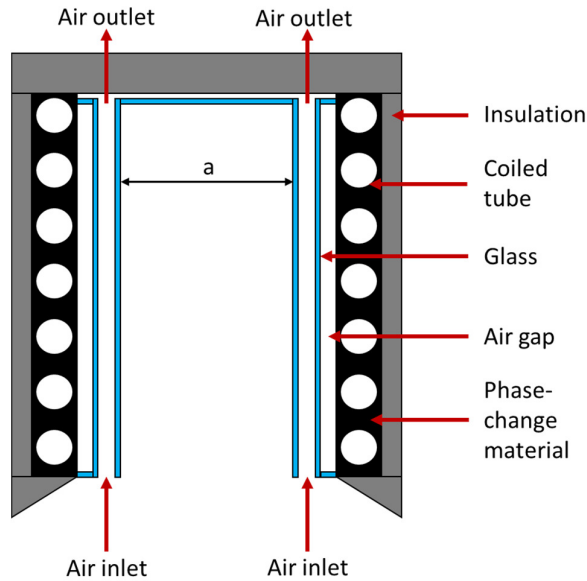
Figure 3.4 Window cover concept

3.4.3.1 Radiation heat transfer

The radiation heat loss rate from a surface could be calculated with equation (2.11). The radiation heat losses from the window to the environment through the receiver aperture depend on the emissivity of the window, the area of the window and the view factor of the window to the aperture. The view factor determines how much a certain part of the glass is exposed to the aperture (environment), inner-cavity wall or the other glass panes. In addition to the radiation heat transfer that the window will absorb from the cavity walls, it will also absorb radiation from other windows around it, which could be calculated by equation (3.22):

$$\dot{Q}_{loss,rad,win} = A_n \sum_{j=1}^{N} F_{n \rightarrow j} \left(\varepsilon_n \sigma T_{s,n}^4 - \varepsilon_j \sigma T_{s,j}^4 \right) \tag{3.22}$$

When calculating the surface temperature of the glass, equation (3.22) was used. Equation (3.22) includes the view factor (sometimes called the shape factor), which was a very important aspect to consider. A detailed explanation of the view factors that were used is provided in Appendix A.

3.4.3.2 Convection heat transfer

Natural convection on the inside of the cavity is a relatively complex phenomenon. Paitoonsurikarn and Lovegrove (2006) showed good agreement between their newly developed correlation and numerical simulation results. Their Nusselt number correlation, based on the Rayleigh and Prandtl numbers for receivers, was derived from free convection heat loss simulations. It was shown that a

38

parameter described as the ensemble cavity length scale, L_s, could be used to account for the effects of cavity geometric parameters and inclination (Paitoonsurikarn & Lovegrove, 2003, Paitoonsurikarn et al., 2004). The ensemble length, L_s, is shown in equation (3.23):

$$L_s = \left| \bar{a}_i \cos^{\bar{b}_i}(\theta + \bar{\psi}_i) L_i \right|$$

(3.23)

The index, i, in equation (3.23) depends on three length scales of the receiver, namely the width (L_1), depth (L_2) and aperture size (L_3), shown in Figure 3.5, which are represented with the symbol L_i in equation (3.23). The constants $\bar{a}_i$, $\bar{b}_i$ and $\bar{\psi}_i$ was found by Paitoonsurikarn and Lovegrove (2006) and are summarised in Table 3.1. Equation (3.23) depends on the cavity dimensions as well as the inclination angle (θ) of the receiver. Paitoonsurikarn and Lovegrove (2003) found the constants, shown in Table 3.1, by fitting a curve to CFD simulation results.

Table 3.1 Constants used in equation (3.23) (Paitoonsurikarn & Lovegrove, 2006)

i	$\bar{a}_i$ (−)	$\bar{b}_i$ (−)	$\bar{\psi}_i$ (−)
1	4.08	5.41	-0.11
2	-1.17	7.17	-0.30
3	0.07	1.99	-0.08
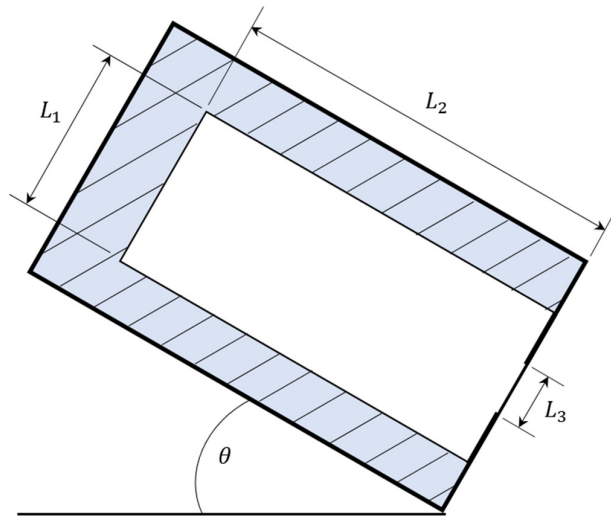
Figure 3.5 Cavity geometric parameters used in the definition of equation (3.23) (Paitoonsurikarn & Lovegrove, 2006)

The modified Nusselt number correlation had the form as given by equation (3.24) (Paitoonsurikarn & Lovegrove, 2006):

39

$$Nu_L = 0.0196 \, Ra_L^{0.41} \, Pr^{0.13} \qquad (3.24)$$

The Rayleigh and Prandtl numbers in equation (3.24) were evaluated at the film temperature, which was taken to be the average between the glass surface temperature, T_s, and the ambient temperature, T_∞. The heat transfer coefficient on the inside of the cavity, h_{cav}, was calculated by rearranging equation (2.3). The heat loss per window section due to convection from the glass surface to the air in the cavity was calculated using an equation similar to equation (3.18). The average heat transfer coefficient for the whole cavity was used, along with the area of the glass as well as the glass surface temperature and environment temperature.

An enclosure is created between the glass pane and the receiver wall, as shown in Figure 3.4. The receiver wall was in direct contact with thermal storage material that provided a constant surface temperature to the receiver wall. The glass panes are heated by concentrated solar irradiation, depending on the absorption coefficient of the glass. Therefore, the receiver wall will be the hotter surface, and the glass pane the cooler surface. The relations for natural convection in an enclosure are subject to strict validity parameters, especially aspect ratio (H/L_c), Prandtl and Rayleigh numbers. The receiver's height was 0.5 m, and the characteristic length was the distance between the glass pane and the receiver wall. The aspect ratio was about 8 for this study which is in the validity range of aspect ratios for the Nusselt correlation given by Pendyala et al. (2015).

The channel's forced internal convection heat transfer rate was calculated with the equations that were presented in Section 2.3.1.2. It must be noted that there were different Nusselt number correlations, and thus different heat transfer coefficients, for the different flow regimes. The code that calculated the heat transfer coefficient used an if-statement to determine the appropriate Nusselt number based on the Reynolds number. The hydrodynamic entrance length for turbulent flow is significantly shorter than laminar flow, when compared to the total length of the channel or tube. A check was thus implemented in the code to check the entry lengths. It was found that the flow was turbulent for a channel width of 6.8 mm; thus, the entry length is much shorter than the total length of the cooling channel. Therefore, it was assumed that the flow was fully developed.

3.4.3.3 Pressure drop in cooling channel

For fully developed flow in a circular duct, the pressure drop is influenced by friction, length of the duct, density and velocity and is given by equation (3.19). The only difference for a rectangular duct is that the hydraulic diameter, D_h, was calculated by equation (2.7) and was used instead of the diameter, D.

The symbols a and b in equation (2.7) refer to the channel height and width respectively. For laminar

flow in a duct with constant heat flux, the friction factor can be interpolated from Table 2.1 at the specific ratio, a/b. For turbulent flow, equation (2.9) can be used to calculate the friction factor in the rectangular duct. The friction factor can then be used with equation (3.19) to calculate the pressure drop in the duct.

3.5   Recuperator geometry

The same counterflow plate-type heat exchanger was considered for the recuperator in this study as the one used by Le Roux and Sciacovelli (2019). Figure 3.6 shows the recuperator dimensions and layout. The pressure drop through the recuperator was calculated according to the same method as the method used by Le Roux and Sciacovelli (2019). The forced convection heat transfer coefficients for the hot and cold sides of the channel (h_h and h_c) were calculated to find the overall heat transfer coefficient, U. The overall heat transfer coefficient depended on the Reynolds number, aspect ratio and average temperature (Le Roux & Sciacovelli, 2019). The effectiveness, ε, of the recuperator was found by using the $\varepsilon - NTU$ method, which included heat loss to the environment, as proposed by Nellis and Pfotenhauer (2005). The number of transfer units (NTU) for the hot side of the recuperator was found with equation (3.25) (Le Roux & Sciacovelli, 2019). The heat loss from the hot and cold recuperator channels was calculated according to the work of Le Roux et al. (2014b).

$$NTU_h = \frac{U a_{reg} L_{reg} (2n - 1)}{\dot{m}_h c_{p0,h}} \tag{3.25}$$
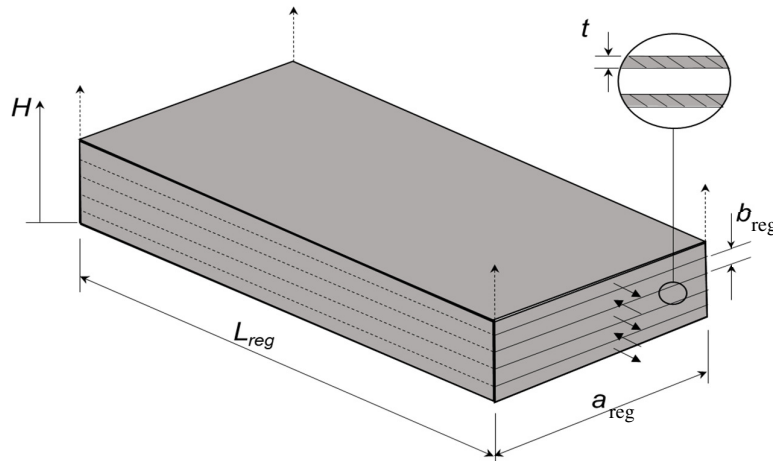
Figure 3.6 Plate-type counterflow heat exchanger (Le Roux, 2011)

3.6   Parameters

Le Roux and Sciacovelli (2019) suggested that the turbine pressure ratio be used as a parameter. This allows for either the net power output of the cycle or the solar-to-mechanical efficiency to be

41

maximised while finding the optimum geometry of the recuperator for each pressure ratio of the turbine. To keep cost and computational time to a minimum, specific turbine and compressor pairings were not done in this study. Rather, as was done in Le Roux and Sciacovelli (2019), three off-the-shelf turbochargers from Garrett Motion in the USA were considered, each with a high-speed generator coupled directly to the shaft (assuming for this to be possible). The three off-the-shelf turbochargers that were used, were the *GT2052*, the *GT1241* and the *GT2850RS*. Turbine maps were used where the pressure ratio was given as a function of the corrected mass flow rate, as shown in Appendix D. According to Le Roux and Sciacovelli (2019), the actual mass flow rate was found with equation (3.26), where the unit of P_7 is pounds per square inch and the unit of T_7 is degrees Fahrenheit:

$$\dot{m}_t = \frac{\dot{m}_{tCF} \times \frac{P_7}{14.7}}{\sqrt{\frac{(T_7 + 460)}{519}}} \tag{3.26}$$

The turbine efficiency depended on the blade speed ratio (*BSR*) as well as the maximum turbine efficiency ($\eta_{t,max}$), which was available from the turbine map and was in line with typical values for automotive applications, i.e of $\eta_{t,max} \approx 0.65 - 0.75$ (Guzzella & Onder, 2010). The *BSR* and turbine efficiency was calculated by equation (3.27) and equation (3.28) respectively, according to Le Roux and Sciacovelli (2019).

$$BSR = \frac{\frac{2\pi N'}{60}\left(\frac{D_t}{2}\right)}{\left[2h_{in}\left(1 - r_t^{\frac{1-k}{k}}\right)\right]^{1/2}} \tag{3.27}$$

$$\eta_t = \eta_{t,max}\left(1 - \left(\frac{BSR - 0.6}{0.6}\right)^2\right) \tag{3.28}$$

Using *Octave*, the shaft speed and isentropic compressor efficiency was determined by interpolation from a compressor map (see Appendix C), using the compressor ratio and the corrected mass flow rate. The corrected compressor mass flow rate was found by equation (3.29), according to Le Roux and Sciacovelli (2019). The units of P_1 and T_1 were pounds per square inch and degrees Fahrenheit respectively. It was assumed that $\dot{m}_t = \dot{m}_c$. To prevent flow surge and choking, the compressor was only allowed to operate within the range of its compressor map (Le Roux & Sciacovelli, 2019).

$$\dot{m}_{cCF} = \frac{\dot{m}_c \times \sqrt{\frac{(T_1 + 460)}{545}}}{\frac{P_1}{13.95}} \tag{3.29}$$

Another parameter that was considered in this study was the width of the cooling channel, which was

42

formed by the two glass panes (see Figure 3.7). Four different channel widths were considered, and the net power output, solar-to-mechanical efficiency and glass surface temperatures were investigated for each channel width. However, the channel width was a constant in the main analysis and only used as a parameter in a parametric analysis and not as a variable to reduce computational time. The channel width was varied in the parametric analysis from 4.8 mm to 6.8 mm in increments of 1 mm. The receiver phase-change temperature was also used as a parameter in the study, with a temperature of 900 K, 1000 K, 1100 K or 1200 K. (See Table 3.2 for a summary of the parameters.)

Table 3.2 Parameters used in the analysis (Le Roux & Sciacovelli, 2019)

Parameter	*Range*
Receiver phase-change temperature, T_s (K)	900-1200
Turbocharger number, MT	1-3
Turbine pressure ratio, r_t	According to turbine map of turbocharger (see Appendix D)
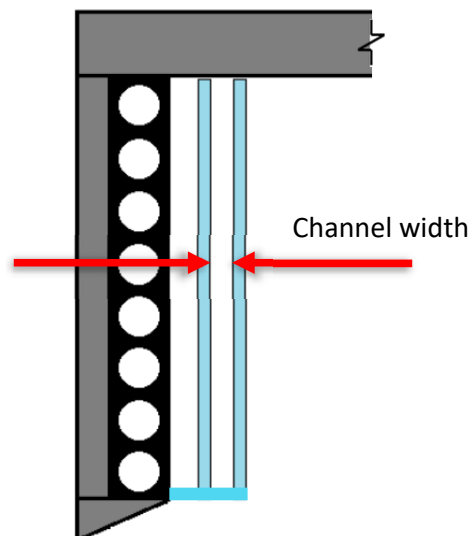
Figure 3.7 Section showing channel width

3.7 Geometric variables and objective function

The geometric variables were used in equation (3.12) and equation (3.13) to calculate the net power output of the cycle. The net power output and the total absorbed solar heat rate were then used in the objective function, which was the solar-to-mechanical efficiency. The temperatures and pressures at each state in the cycle (Figure 1.3) were written in terms of the geometric variables. Similar geometric variables were used as those considered by Le Roux and Sciacovelli (2019) to allow for a comparison

43

between the results to determine the impact of the window on the cycle. The geometric variables are shown in Table 3.3.

Table 3.3 Geometric variables (Le Roux & Sciacovelli, 2019)

Variable	*Range*
Width of recuperator channel, a_{reg} (mm)	150-450 (step size: 75)
Recuperator channel height, b_{reg} (mm)	1.5-4.5 (step size: 0.75)
Length of recuperator, L_{reg} (m)	0.5-3.5 (step size: 0.75)
Recuperator number of parallel flow channels, n	15-45 (step size: 7.5)

When combining equations (3.12) and (3.13), the net power output function was found and is shown in equation (3.30):

$$
\begin{aligned}
\dot{W}_{net} = {} & \left(1 - \frac{T_0}{T^*}\right)\dot{Q}^* + \dot{m}c_{p0}(T_1 - T_{11}) - T_0\dot{m}c_{p0}\ln\left(\frac{T_1}{T_{11}}\right) \\
& -T_0\left[-\dot{m}c_{p0}\ln\left(\frac{T_1}{T_2}\right) + \dot{m}R\ln\left(\frac{P_1}{P_2}\right)\right]_{compressor} \\
& -T_0\left[\dot{m}c_{p0}\ln\left[\frac{T_{10}T_4}{T_9T_3}\left(\frac{P_{10}P_4}{P_9P_3}\right)^{-\frac{R}{c_{p0}}}\right] + \frac{\dot{Q}_{loss,reg}}{T_\infty}\right]_{recuperator} \\
& -T_0\left[-\frac{\dot{Q}^*_{rec}}{T^*} + \frac{\dot{Q}_{loss,cond,rec}}{T_\infty} + \dot{m}c_{p0}\ln\left(\frac{T_6}{T_5}\right) - \dot{m}R\ln\left(\frac{P_6}{P_5}\right)\right]_{receiver} \\
& -T_0\left[-\dot{m}c_{p0}\ln\left(\frac{T_7}{T_8}\right) + \dot{m}R\ln\left(\frac{P_7}{P_8}\right)\right]_{turbine} \\
& -T_0\left[-\dot{m}c_{p0}\ln\left(\frac{T_2}{T_3}\right) + \dot{m}R\ln\left(\frac{P_2}{P_3}\right) + \frac{\dot{Q}_{loss,win}}{T_\infty} - \frac{\dot{Q}^*_{win}}{T^*}\right]_{window} \\
& -T_0\left[-\dot{m}c_{p0}\ln\left(\frac{T_4}{T_5}\right) + \dot{m}R\ln\left(\frac{P_4}{P_5}\right) + \frac{\dot{Q}_{loss,4-5}}{T_\infty}\right]_{duct\ 4-5} \\
& -T_0\left[-\dot{m}c_{p0}\ln\left(\frac{T_6}{T_7}\right) + \dot{m}R\ln\left(\frac{P_6}{P_7}\right) + \frac{\dot{Q}_{loss,6-7}}{T_\infty}\right]_{duct\ 6-7} \\
& -T_0\left[-\dot{m}c_{p0}\ln\left(\frac{T_8}{T_9}\right) + \dot{m}R\ln\left(\frac{P_8}{P_9}\right) + \frac{\dot{Q}_{loss,8-9}}{T_\infty}\right]_{duct\ 8-9}
\end{aligned}
\tag{3.30}
$$

Equation (3.30) was then used along with the total absorbed solar heat, $\dot{Q}^*_{tot} = \dot{Q}^*_{win} + \dot{Q}^*_{rec}$, to find the solar-to-mechanical efficiency, which was used as the objective function in this study (see equation (3.31)). The maximum solar-to-mechanical efficiency was found for each micro-turbine and each pressure ratio by considering all the possible recuperator geometries.

$$\eta_{sol} = \frac{\dot{W}_{net}}{\dot{Q}_{tot}^*} \tag{3.31}$$

The energy utilisation factor (*EUF*) is an important cycle performance metric that had to be considered. The *EUF* indicates the extent to which the cycle could convert the available solar power into useful power and heat (Le Roux, 2018). The *EUF* is given by equation (3.32),

$$EUF = \frac{\left(\dot{W}_{net} + \eta_{reg}\dot{Q}_{max,T_{11-1}}\right)}{\dot{Q}_{tot}^*} \tag{3.32}$$

where the quantity $\dot{Q}_{max,T_{11-1}}$ is given by equation (3.33), which describes the maximum water-heating potential. The temperature at the inlet, T_1, was taken to be 300 K and the outlet temperature, T_{11}, was calculated with the numerical analysis as described in this section. The constant pressure specific heat, c_{p0}, was calculated at the average temperature between T_1 and T_{11} for air, which was about 1016 J/kgK. The mass flow rate was calculated according to equation (3.26). The effectiveness of the recuperator, η_{reg}, was assumed to be 65% (Le Roux, 2018) and the term $\eta_{reg}\dot{Q}_{max,T_{11-1}}$ in equation (3.32) is referred to as $\dot{Q}_w$ further in the study.

$$\dot{Q}_{max,T_{11-1}} = \dot{m}c_{p0}(T_{11} - T_1) \tag{3.33}$$

The mass of the recuperator was restricted to 500 kg to limit its cost, weight and size (Le Roux & Sciacovelli, 2019). The mass of the recuperator was calculated by equation (3.34), where ρ_{steel} was assumed to be 8000 kg/m^3:

$$Mass = 2n\left(2a_{reg}L_{reg} + 2b_{reg}L_{reg}\right) \times \rho_{steel} \tag{3.34}$$

3.8   Constants and assumptions

3.8.1   Assumptions

1) It was assumed that the phase-change material in the solar receiver, as well as the inner-cavity walls and the receiver tube surface, was at a constant temperature (the melting temperature).

2) It was assumed that each glass window was 3 mm thick.

3) In this conceptual study, the temperature distribution across the thickness of the glass panes was not taken into consideration and it was assumed that the two sides of each of the glass panes were at the same average temperature. Since there were two glass panes per channel, the effective transmissivity for infrared radiation became negligible. Therefore, it was

45

assumed in this work that for infrared radiation, the reflectivity and absorptivity of the double-glass window were 90% and 10% respectively.

4) The emissivity of the glass was assumed to be constant at 0.88 (Subedi et al., 2019).

5) Equation (3.15) and equation (3.22) have a term raised to the fourth power. To be able to use Gaussian elimination, the term $T_{s,n}^4$ was assumed to have the form $m_1 T_{s,N} + c_1$ for radiation heat loss between 500 K and 800 K (a linear regression line – see Figure 3.8) (Le Roux et al., 2014a).

6) It was assumed that $T_{10} = T_{11}; T_8 = T_9$ and $P_8 = P_9$ (it was assumed that the recuperator and turbine were close to each other); $\dot{Q}_{loss,6-7} = 0$ (it was assumed that the heat losses in the duct from State 6 to State 7 were negligible).

7) Conduction heat losses from the air-cooled window were not considered in this study and were expected to be negligible.

8) The width between the two glass panes forming the channel was arbitrarily chosen as 6.8 mm. The simulations were initially carried out with this channel width and later changed to see its effect.

9) It was also assumed that the solar dish had a 0° tracking error.
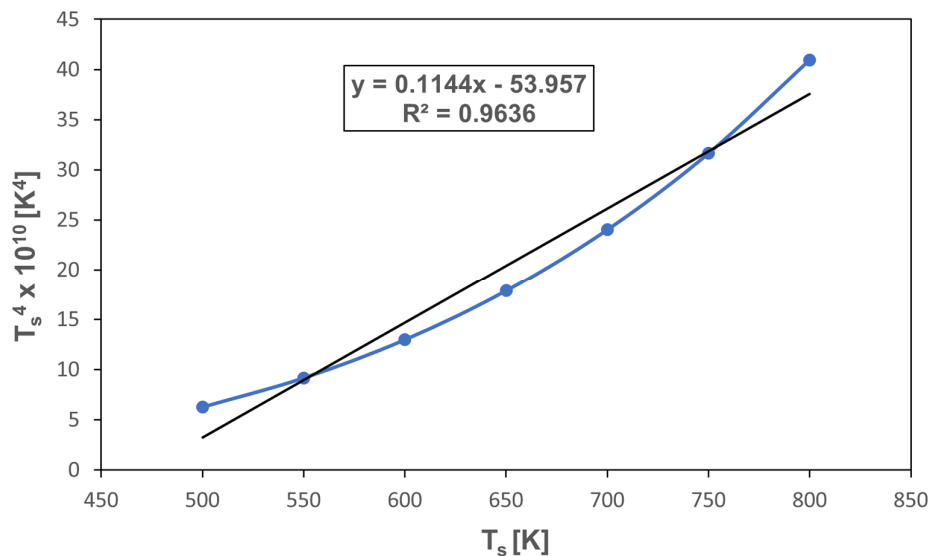
Figure 3.8 The regression line for $T_{s,n}{}^4$

3.8.2 Constants

Table 3.4 shows the recuperator constants, which were used in the analysis. Most of these constants were kept the same as those used in previous work by Le Roux and Sciacovelli (2019). The atmospheric pressure for Pretoria (South Africa) was taken as 85 kPa.

46

Table 3.4 Constants used in the analysis (Le Roux & Sciacovelli, 2019)

Constant	*Value*
Recuperator plate thickness, t_{reg} (mm)	0.5
Conductivity of stainless steel, k_{ss} (W/mK)	18.3 (600 K) (Çengel & Ghajar, 2015)
Recuperator insulation thickness, t_{ins} (m)	0.05
Recuperator insulation conductivity, k_{ins} (W/mK)	0.18
Recuperator outer convection heat transfer coefficient, h_{out} (W/m²K)	25
Receiver aperture area, $a_{aper} \times a_{aper}$ (m²)	$0.25 \times 0.25 = 0.0625$
Receiver height, H (m)	0.5
Tube diameter of receiver coil, d (m)	0.0833
Ambient temperature, T_0 (K)	300
Ambient pressure, P_0 (kPa)	85
Glass thickness, t_{gl} (m)	0.003
Average elevation angle of the receiver, θ	45°

3.9   Numerical methods

The numerical methods that are described in this section were used to calculate the glass surface temperature and the net heat transfer rates to the air travelling through the glass channels. These numerical methods were then integrated into the methodology of Le Roux and Sciacovelli (2019) to model and optimise the full cycle (see Appendix E and Appendix F for the code).

The temperature profile of the glass was determined by dividing each of the four glass panes into several equally sized sections (see Figure 3.9). Each of the four sides of the rectangular receiver was divided into five sections, which gave each section a height of 0.1 m. The top section was also covered with glass in the simulation (with its air inlet from the compressor) to account for the view factor to the top. The top glass pane was not divided into sections to limit computational time.
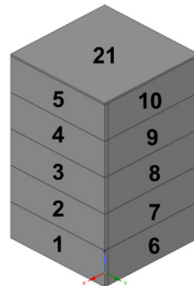
Figure 3.9 The numbering system used for glass sections

Figure 3.9 shows the numbering system used for the glass sections, where the top section was added to the end of the numbering system. The proposed method was based on the method put forward by Le Roux et al. (2014a), the main difference being that the flow was not modelled to flow in a coil but rather from the bottom to the top of each window. The temperature profile and the net heat transfer rate at the various sections of each glass window were derived by equation (3.35). It must be noted that each window's mass flow rate, $\dot{m}_{chn}$, was equal to the mass flow rate at State 1 in Figure 1.3 divided by five.

$$\dot{Q}_{net,n,win} = \frac{\left(T_{s,n} - \sum_{i=1}^{n-1}\left(\frac{\dot{Q}_{net,i}}{\dot{m}_{chn}c_{p0}}\right) - T_{in,0}\right)}{\left(\frac{1}{h_{chn}A_n} + \frac{1}{2\dot{m}_{chn}c_{p0}}\right)} \tag{3.35}$$

Equation (3.35) was derived from the definition of fluid temperature at the centre of a control volume as well as the definition of convection heat transfer, according to equation (3.36) and equation (3.37) respectively:

$$T_{f,n} = T_{in,n} + \frac{T_{out,n} - T_{in,n}}{2} = T_{in,n} + \frac{\dot{Q}_{net,n,win}}{2\dot{m}_{chn}c_{p0}} \tag{3.36}$$

$$\dot{Q}_{net,n,win} = h_{chn}A_n(T_{s,n} - T_{f,n}) \tag{3.37}$$

Equation (3.35) used the outlet temperature of the compressor as the inlet, $T_{in,0}$. The outlet air temperature from each section, $T_{out,n}$, was calculated from the heat gained at the previous glass sections. Equation (2.8) and equation (2.9) were used to calculate the heat transfer coefficient in equation (3.35). By using equation (3.18) and equation (3.22) and substituting into equation (3.21), equation (3.38) could be found, which was written in terms of the unknown net heat transfer rates and surface temperatures of each glass section according to Figure 3.9. Note that for the radiation heat loss term, the radiation heat transfer from one glass side to another and the radiation heat loss to the aperture were included. This equation could be simplified further by using a linear approximation (as mentioned in Section 3.8.1):

$$\begin{aligned}
\dot{Q}_{net,n,win} = {} & \dot{Q}_{n,win}^* + \dot{Q}_{abs,n} - A_n\varepsilon\sigma(m_1 T_{s,n} + c_1) \\
& + A_n\varepsilon\sigma\sum_{j=1}^{N} F_{n\to j}(m_1 T_{s,j} + c_1) \\
& + A_n\varepsilon_\infty\sigma F_{n\to\infty}T_\infty^4 - h_{n,cav}A_n(T_{s,n} - T_\infty)
\end{aligned} \tag{3.38}$$

The $\dot{Q}_{abs,n}$ term in equation (3.38) is the radiation and convection heat transfer, which was transferred

48

from a section of the inner-receiver wall to a section of the window directly in front of it. Equation (3.24) was used to calculate the heat transfer coefficient, $h_{n,cav}$, in equation (3.38). By using Gaussian elimination in *Octave*, the surface temperatures ($T_{s,n}$) and net heat transfer rates ($\dot{Q}_{net,n,win}$) of each window could be calculated by solving equation (3.35) and equation (3.38) simultaneously. The outlet air temperature of the air-cooled window is State 3, shown in Figure 1.3. The outlet air temperature was calculated by rearranging equation (3.39) and solving for $T_{a,out}$:

$$\dot{Q}_{net,win} = \dot{m}_{chn}c_{p0}\left(T_{a,out} - T_{a,in}\right)$$
<div align="right">(3.39)</div>

The mass flow rate in equation (3.39) was calculated based on the corrected mass flow rate of each turbocharger (see Section 3.6) divided by five. Equation (3.39) could also be used to check whether the Gaussian elimination function had been calculated correctly because $\dot{Q}_{net,win}$ had to be equal to the sum of the heat transfer rates that were calculated at each section of the window using equation (3.38). The outlet air temperature was used in modelling the complete cycle. A summary of the code structure that was used as well as the full *Octave* code is shown in Appendix E and Appendix F. The SolTrace model was run with five different solar dish sizes, namely dish diameters of 4.8, 6, 7.2, 8.4 and 9.6 m. From the SolTrace analysis, a relationship was found between the solar flux on the glass panes and the inner-receiver walls (the relationship between $\dot{Q}^*_{win}$ and $\dot{Q}^*_{rec}$). The relationship was found to be linear and had the form as given by equation (3.40):

$$\dot{Q}^*_{win} = m\dot{Q}^*_{rec} + c$$
<div align="right">(3.40)</div>

It is important to note that $\dot{Q}^*_{win}$ only includes the solar heat flux contribution and not the reradiation from the inner-cavity wall. The total required solar power is used further in the analysis and is given by equation (3.41), which is a function of the dish size and can be used to estimate the dish size required for steady-state cycle operation:

$$\dot{Q}^*_{tot} = \dot{Q}^*_{win} + \dot{Q}^*_{rec}$$
<div align="right">(3.41)</div>

However, the code that calculated the temperature profile of the window (see Appendix E and Appendix F) required the solar flux on the window to be a distribution (per window section) instead of a total value. From the five SolTrace cases, the ratio of the solar flux distribution on each glass division could be found. This ratio was calculated as:

$$\Gamma = \frac{Heat\ flux\ per\ division}{Total\ heat\ flux\ per\ side}$$
<div align="right">(3.42)</div>

A function was written that interpolates between the five different dish-size heat flux ratios. This

distribution was then used as an input in the code (see Appendix E and Appendix F).

3.10 **Summary**

This chapter outlined the physical models of the receiver and the window to be analysed. The entropy generation rate for each component in the cycle led to an exergy analysis, which provided the net power output, and the solar-to-mechanical efficiency of the cycle. The receiver and window models to form the base of the simulation were presented. The parameters and constraints of the analysis were listed along with the most important constants and assumptions. This chapter also summarised the numerical methods that were used to calculate the glass surface temperature and net heat transfer rates and a function interpolating between solar heat fluxes for different parabolic dish sizes.

Chapter 4

Results and discussion

4.1 Introduction

Preliminary results demonstrate the numerical methods used to calculate the glass's surface temperatures and net heat flux. Furthermore, the full analysis results provide insight into each turbocharger's performance at its most efficient pressure ratio and mass flow rate. Furthermore, analysing the various performance metrics show the effect of changing the window-cooling channel's width. Finally, the results of the current and previous work by Le Roux and Sciacovelli (2019) are compared, which provides significant insight into the performance of the cooling window.

4.2 Window model demonstration

A demonstration of the numerical methods proposed in Section 3.9 provides insight into the functionality of the numerical method. The constants used in the demonstration are shown in Table 4.1.

Table 4.1 Constants used in the demonstration

Constant	*Value*
Dish diameter, D_{dish} (m)	4.8
Solar irradiance, I (W/m^2)	1 000
Dish reflectivity, ρ_{dish}	85 %
Total solar heat flux, $\dot{Q}_{tot}^*$ $(W) = I \frac{D^2}{4} \pi \rho_{dish}$	15 381
Cooling channel width, t_{chn} (mm)	6.8
Inlet temperature to window, T_2 (K)	400
Total mass flow rate, $\dot{m}_{tot}$ (kg/s)	0.05
Glass division area, A_{div} (m^2)	0.025
Top glass area, A_{top} (m^2)	0.0625

A SolTrace model with the dish constants shown in Table 4.1 was used to find the solar heat flux on each glass segment. Since a 0° dish tracking error was assumed, the results for all four sides of the receiver were the same. This subsection used a standard numbering procedure to display the results. The side glass panes had the numbers 1 to 5 (bottom to top), and the top glass pane had the number 6.

This numbering system was only for display purposes, and the numbering system used in the main simulations is described in Figure 3.9. Figure 4.1 shows the available solar flux distribution (in kW/m^2) on the glass segments for one side of the receiver glass and the top glass. The available solar flux data was produced by SolTrace, as discussed in section 3.4.1. The heat flux of the side and top glass panes in Figure 4.1, Figure 4.3 and Figure 4.4 was found by dividing the heat rate by the area of the division (0.025 m^2 and 0.0625 m^2, respectively).
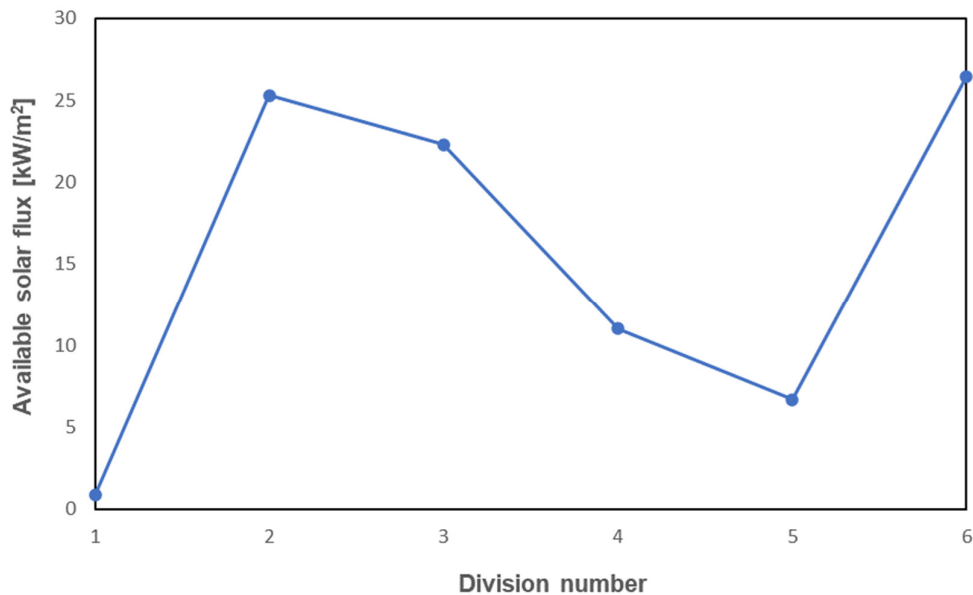
Figure 4.1 Solar heat flux for one side glass and the top glass

Figure 4.2 and Figure 4.3 show the glass surface temperatures and net heat flux to the air flowing through the glass channel as a function of the receiver phase-change temperature for one side glass and the top glass. As the receiver phase-change temperature was increased, the glass surface temperature and net heat flux increased. This was due to the receiver having higher radiation and convection heat losses at higher receiver phase-change temperatures and thus the glass absorbed more heat from the receiver.

The difference in heat flux between the different receiver phase-change temperatures was relatively small. The top glass pane had the highest surface temperature and net heat flux due to the larger portion of solar flux that it received, as shown in Figure 4.1 (Division 6). However, when considering only the glass panes parallel to the receiver walls, Division 3 had the highest surface temperature and Division 2 had the highest heat flux to the air (Figure 4.3). Division 2 had the highest heat flux to the air because it received the largest amount of solar flux compared to all the other side divisions (see Figure 4.1). Therefore, the air has gained significant heat when flowing from Divisions 1 and 2, which is why Division 3 has a higher surface temperature.

52
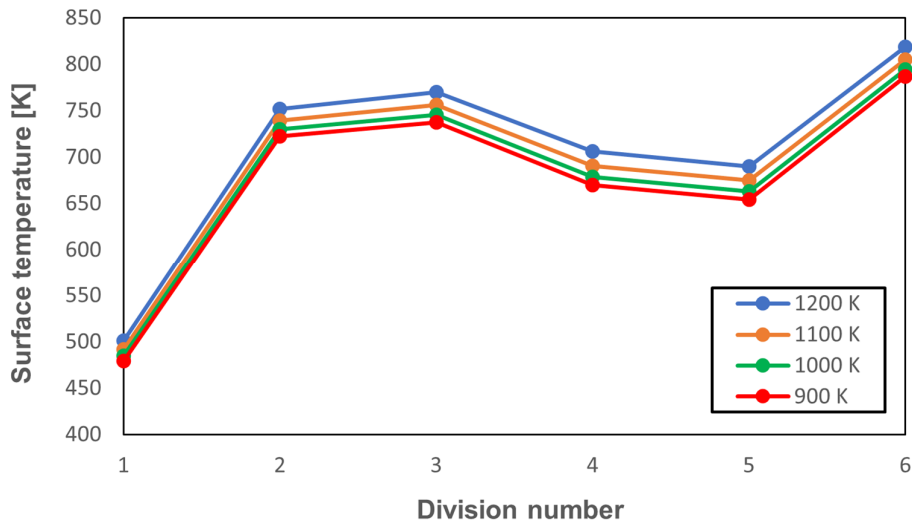
Figure 4.2 Glass surface temperature for one side glass and the top glass as a function of receiver phase-change temperature
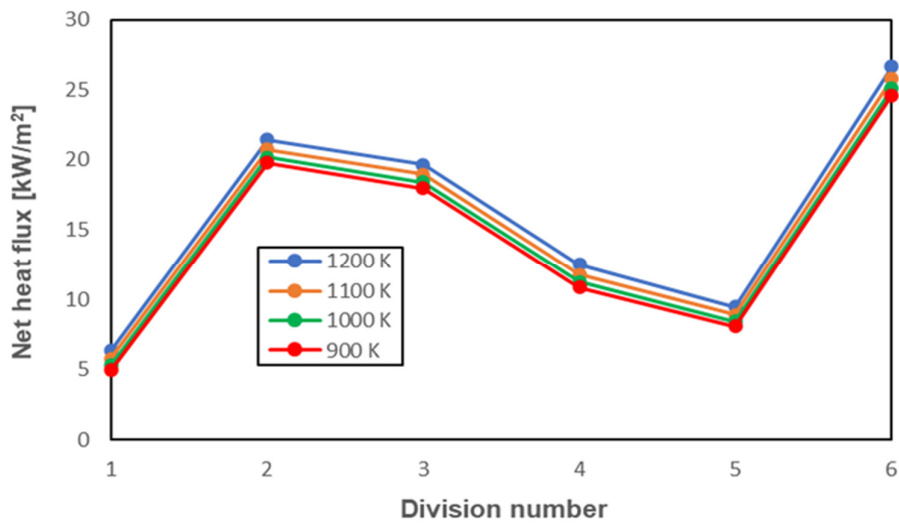
Figure 4.3 Net heat flux for one side glass and the top glass as a function of receiver phase-change temperature

Figure 4.4 shows the glass surface temperatures, the HTF temperatures, and the glass net heat flux for one side of the receiver at a receiver phase-change temperature of 1200 K. It must be noted that the inlet temperature of the HTF at each glass division was equal to the outlet temperature of the last division. Only the outlet temperatures are plotted in Figure 4.4. The air gained heat as it flowed from the bottom to the top of the cooling channel. The air had a change in temperature of about 156 °C and gained about 1.7 kW of heat from the glass as it moved through the cooling channel for one side of the receiver for a receiver temperature of 1200 K.

53
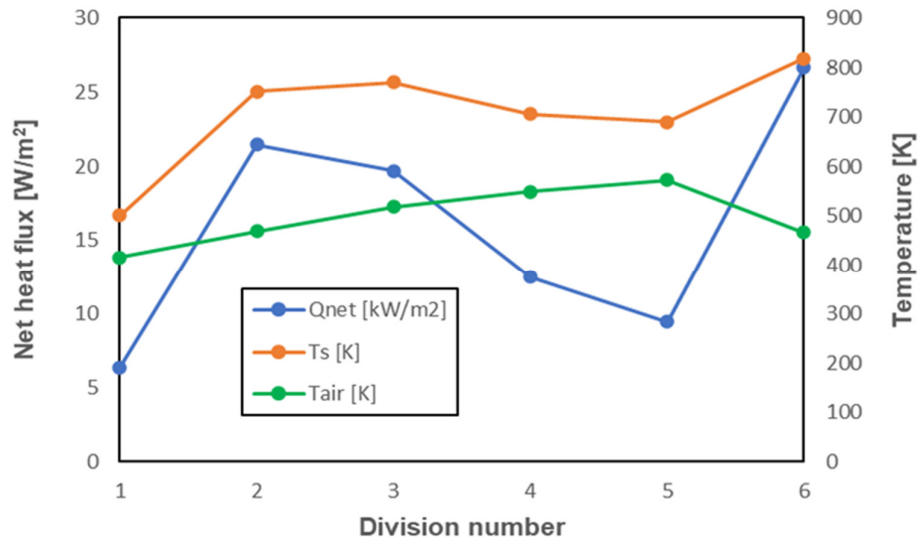
Figure 4.4 Temperatures and heat flux at a receiver phase-change temperature of 1200 K for one side of the receiver

The calculated heat transfer rate using equation (3.39) and the sum of each division's net heat transfer rates were compared, and the average difference was found to be 1e-13. Therefore, based on this demonstration, the numerical method used to calculate the surface temperature and net heat transfer rates of the glass could be used in the full analysis of the cycle. The results also indicated that the receiver phase-change temperature did make a difference in the glass surface temperature and net heat transfer rate. The effect of mass flow rate, cooling channel width and receiver phase-change temperature on the glass was investigated in the full analysis and the results are shown in the following section.

4.3 Full analysis

This section presents the results of the numerical analysis with a focus on the impact of the air-cooled window on the performance of the system. The results of the required solar input power, net power output, and cycle temperatures at maximum solar-to-mechanical efficiency are presented. The impact of different cooling window channel widths on the pressure drop, heat transfer, temperature change and glass surface temperature is also presented. Finally, the impact of the cooling window on the performance of the cycle was evaluated. It must be noted that the code used to obtain the following results was based on the work of Le Roux and Sciacovelli (2019) with the only difference being an increased resolution of the while loop (hereinafter referred to as tolerance) as well as some minor adjustments in the initial assumed values (see Appendix E and Appendix F for a complete explanation of the code).

54

The parameters, variables, constraints, assumptions, as well as constants that were used in the analysis, are described in Chapter 3. It must be noted that the results in this section were produced with a cooling channel width of 6.8 mm. This specific channel width was chosen based on initial pressure drop calculations to keep the pressure drop below 1 kPa. The code was used to iterate through all the turbochargers' different pressure ratios as well as the different recuperator geometries. The maximum solar-to-mechanical efficiency was then found for each turbine pressure ratio as well as the net power output and required solar input power at that specific maximum solar-to-mechanical efficiency.

4.3.1 Maximum solar-to-mechanical efficiency

Figure 4.5 to Figure 4.7 show that the maximum solar-to-mechanical efficiency increased as the receiver phase-change temperature increased, especially at higher turbine pressure ratios. Figure 4.5 to Figure 4.7 indicate that maximum solar-to-mechanical efficiencies of up to 12% could be achieved. Figure 4.5 to Figure 4.7 also show that there were some outliers (or dips) in the solar-to-mechanical efficiency at certain pressure ratios, which could be due to the code not solving within the specified number of iterations or tolerance.
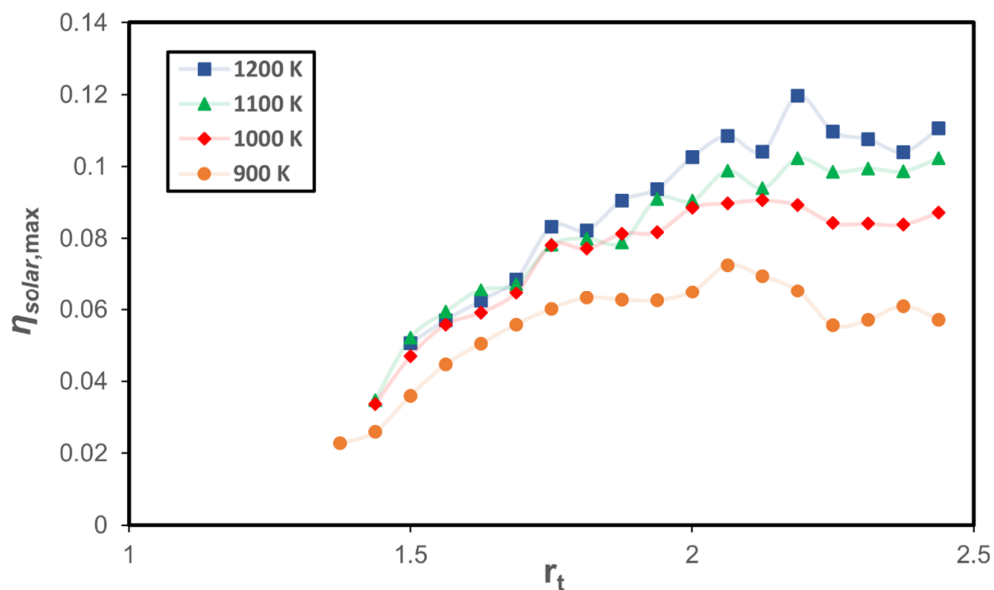
Figure 4.5 Maximum solar-to-mechanical efficiency of the cycle for different turbine pressure ratios and receiver phase-change temperatures from 900 K to 1200 K (for *GT1241*).
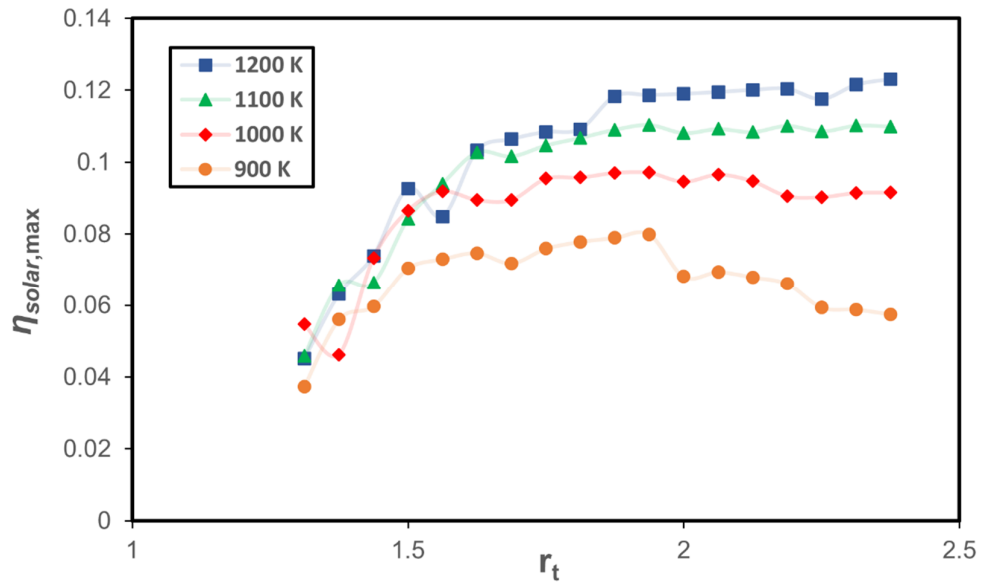
Figure 4.6 Maximum solar-to-mechanical efficiency of the cycle for different turbine pressure ratios and receiver phase-change temperatures from 900 K to 1200 K (for *GT2052*).
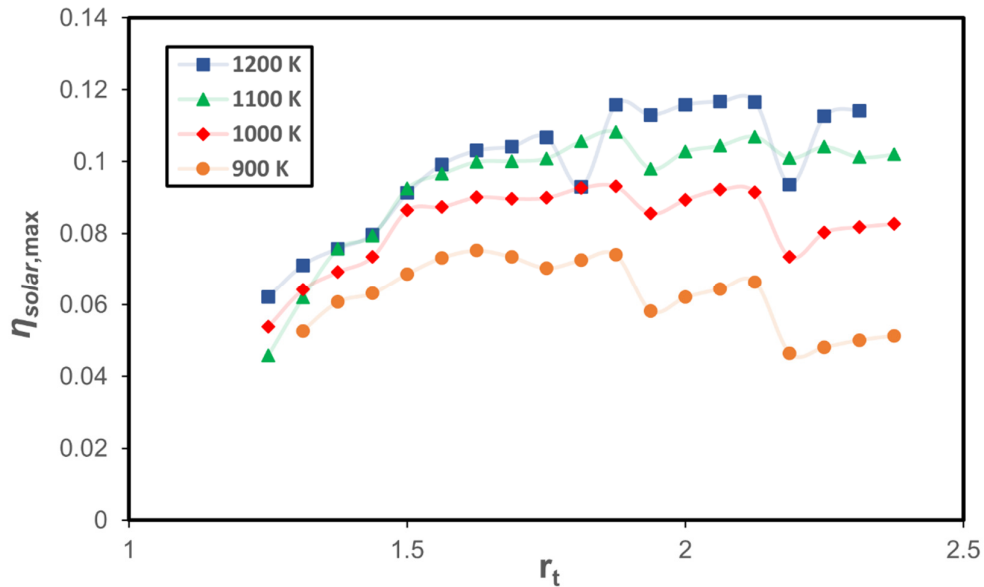
Figure 4.7 Maximum solar-to-mechanical efficiency of the cycle for different turbine pressure ratios and receiver phase-change temperatures from 900 K to 1200 K (for *GT2860RS*).

Table 4.2 to Table 4.4 show the results of the maximum solar-to-mechanical efficiency for each turbocharger, which correlates to Figure 4.5 to Figure 4.7. Figure 4.5 to Figure 4.7 show that, at a receiver temperature of 900 K, the solar-to-mechanical efficiencies decreased as the pressure ratio was increased, which led to the relatively low optimum pressure ratios observed in Table 4.3 and Table 4.4.

56

Table 4.2 to Table 4.4 show that for the assumed receiver phase-change temperatures, most of the optimum recuperators had the following dimensions: a channel width of 450 mm, channel height of 1.5 mm, channel length of 0.5 m, and 45 parallel flow channels in a single direction (90 in total). Model validation was done by calculating the difference between the $\dot{W}_{net}$ calculated with the exergy analysis, first law of thermodynamics and first law heat balance. Essentially this difference indicated how well the numerical methods solved the relevant equations. A detailed explanation of this validation is given in Appendix B.

Table 4.2 Maximum solar-to-mechanical efficiency for *GT1241* and different surface temperatures

T_s (K)	$r_{t,opt}$	a_{reg} (mm)	b_{reg} (mm)	L_{reg} (m)	n	$\dot{W}_{net}$ (W)	$Mass$ (kg)	$\dot{Q}_{tot}^*$ (kW)	$\eta_{sol,max,max}$
900	2.063	375	2.25	0.5	45	1262	272	17.4	0.072
1000	2.125	450	1.5	0.5	45	1811	325	20.0	0.091
1100	2.438	300	1.5	0.5	45	2859	217	27.9	0.102
1200	2.188	300	2.25	1.25	30	3064	363	25.6	0.120

Table 4.3 Maximum solar-to-mechanical efficiency for *GT2052* and different surface temperatures

T_s (K)	$r_{t,opt}$	a_{reg} (mm)	b_{reg} (mm)	L_{reg} (m)	n	$\dot{W}_{net}$ (W)	$Mass$ (kg)	$\dot{Q}_{tot}^*$ (kW)	$\eta_{sol,max,max}$
900	1.938	450	1.5	0.5	45	1985	325	24.8	0.080
1000	1.938	450	1.5	0.5	45	2703	325	27.8	0.097
1100	1.938	450	1.5	0.5	45	3454	325	31.3	0.110
1200	2.375	450	2.25	0.5	45	6098	326	49.6	0.123

Table 4.4 Maximum solar-to-mechanical efficiency for *GT2860RS* and different surface temperatures

T_s (K)	$r_{t,opt}$	a_{reg} (mm)	b_{reg} (mm)	L_{reg} (m)	n	$\dot{W}_{net}$ (W)	$Mass$ (kg)	$\dot{Q}_{tot}^*$ (kW)	$\eta_{sol,max,max}$
900	1.625	450	2.25	0.5	45	1939	326	25.8	0.075
1000	1.875	450	1.5	0.5	45	3656	325	39.3	0.093
1100	1.875	450	1.5	0.5	45	4705	325	43.5	0.108
1200	2.063	450	1.5	0.5	45	6804	325	58.3	0.117

Considering Table 4.2 to Table 4.4, the *GT2052* turbocharger had the highest solar-to-mechanical efficiency of 12.3% at a receiver phase-change temperature of 1200 K; however, it also had a required solar input power of 50 kW. The *GT1241* turbocharger had the second-highest solar-to-mechanical efficiency of 12% at a receiver phase-change temperature of 1200 K, with a required solar input power of 26 kW. The *GT2860RS* turbocharger had a maximum solar-to-mechanical efficiency of 11.7% at a receiver phase-change temperature of 1200 K and required 58 kW of solar input power. For similar solar-to-mechanical efficiencies and receiver phase-change temperatures, a cycle with the *GT1241* turbocharger would require a much smaller solar dish than for a cycle with the *GT2052* or *GT2860RS* turbocharger. However, the net power output that could be produced by the *GT1241* turbocharger was lower than for the other two turbochargers.

For each micro-turbine, Figure 4.8 to Figure 4.10 indicate the cycle's net power output at the maximum solar-to-mechanical efficiency, dependent on the turbine pressure ratio, together with the required solar power at the receiver aperture, $\dot{Q}^*$. The lines of constant solar-power requirement was drawn by selecting a $\dot{Q}^*$ that appeared in the data for each of the four receiver phase change temperatures. The pressure ratio and net power associated with each of these $\dot{Q}^*$ values was then plotted. These net power output figures followed the same trends as the solar-to-mechanical efficiency (Figure 4.5 to Figure 4.7) since they were directly related.
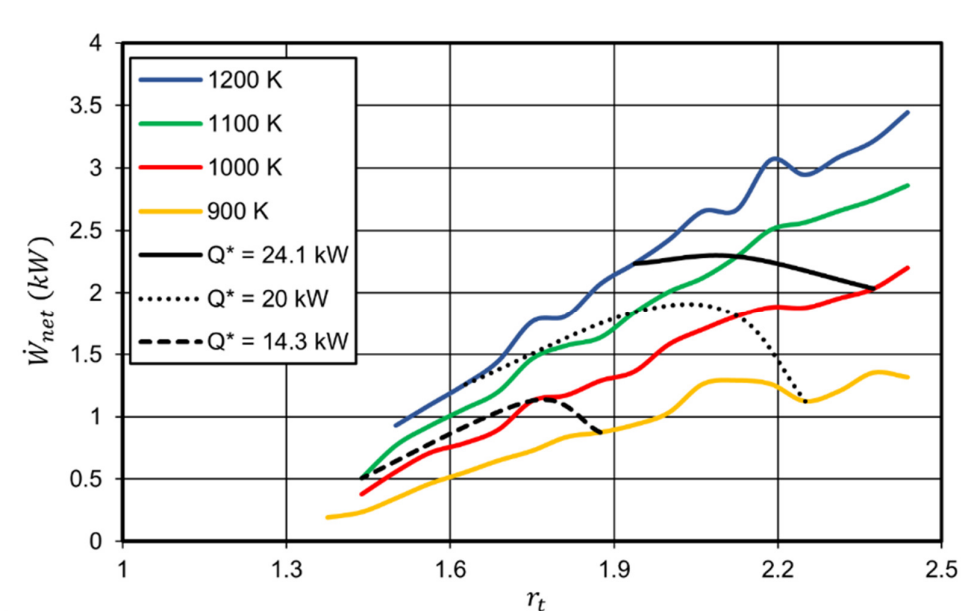
Figure 4.8 Net power output at maximum solar-to-mechanical efficiency as a function of turbine pressure ratio, receiver phase-change temperatures (900 K - 1200 K) and solar input power (for *GT1241*)

58
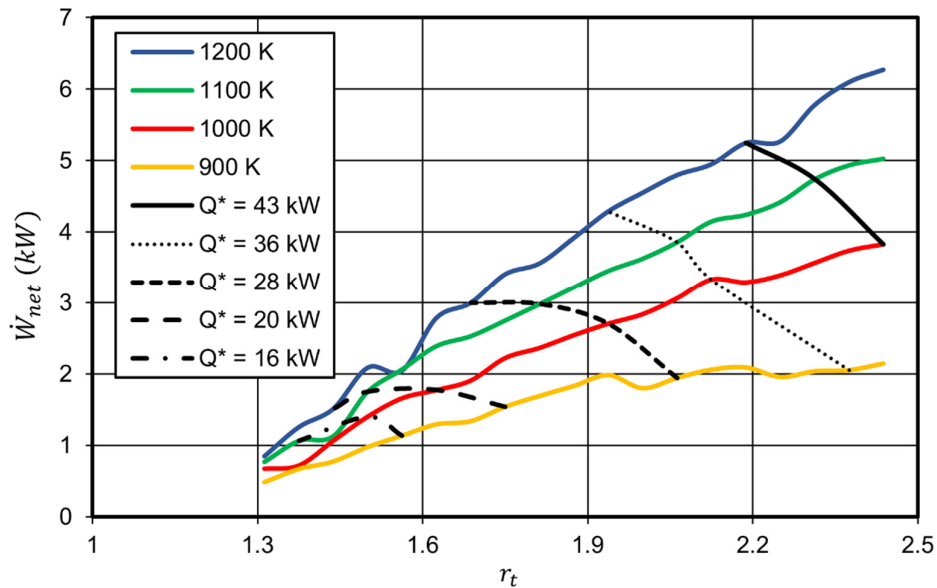
Figure 4.9 Net power output at maximum solar-to-mechanical efficiency as a function of turbine pressure ratio, receiver phase-change temperatures (900 K - 1200 K) and solar input power (for *GT2052*)
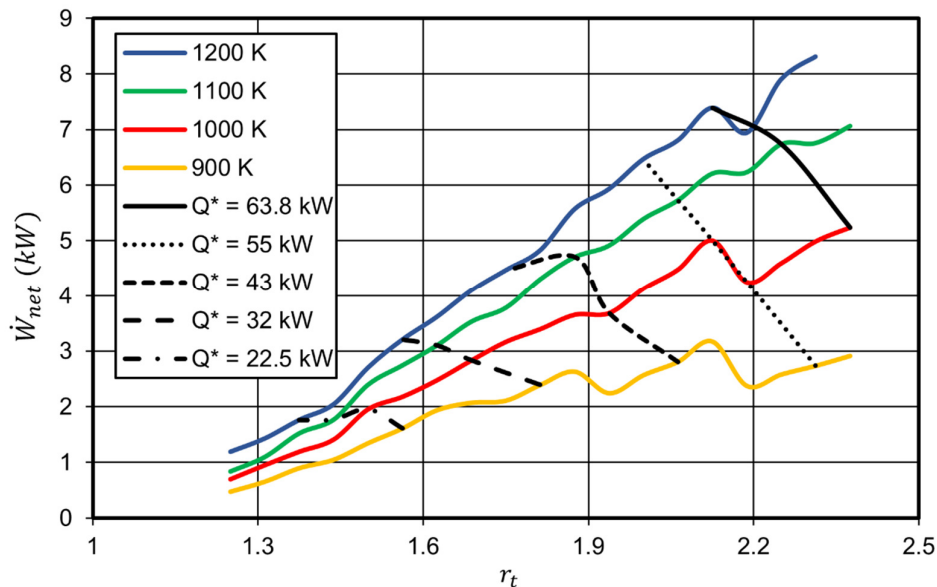
Figure 4.10 Net power output at maximum solar-to-mechanical efficiency as a function of turbine pressure ratio, receiver phase-change temperatures (900 K - 1200 K) and solar input power (for *GT2860RS*)

Figure 4.8 to Figure 4.10 indicate that a larger net power output could be produced by the cycle at higher pressure ratios and higher receiver phase-change temperatures. The required solar input power is an indication of the cost of the solar dish because the aperture of the receiver was fixed at

59

0.25 m × 0.25 m (Le Roux & Sciacovelli, 2019) in this study. Therefore, an increased required solar input represents a larger solar dish and thus increased cost. Figure 4.8 to Figure 4.10 can thus be treated as performance maps as they can be used to select specific dish sizes to achieve a certain net power output at a preferred receiver phase-change temperature. As an example, in Figure 4.9 (for the *GT2052*), for a solar dish with solar input power of $\dot{Q}^* = 28\ kW$, the expected shaft power output is 2 kW at a receiver phase-change temperature of 900 K and turbine pressure ratio of 2.06, while 3 kW of shaft power can be produced at 1200 K and a much lower pressure ratio of 1.69. Figure 4.9 also shows that for a receiver at 1000 K, 3.8 kW of net power can be produced at a required solar input of 43 kW and a pressure ratio of 2.4. However, at a lower pressure ratio of 1.94 and a receiver temperature of 1200 K, 4.3 kW can be produced, but at a smaller required solar input of 36 kW. This shows the significance of these performance maps for a possible future cost analysis study.

Figure 4.11 to Figure 4.13 show the temperatures at the different positions throughout the cycle (see Figure 1.3 for the position numbering) for performance at maximum solar-to-mechanical efficiency when using either the *GT1241, GT2052* or *GT2860RS* turbocharger with the recuperator geometries mentioned in Table 4.2 to Table 4.4.

Figure 4.11 Temperature in the cycle at different receiver phase-change temperatures at maximum solar-to-mechanical efficiency (for *GT1241*)

Figure 4.12 Temperature in the cycle at different receiver phase-change temperatures at maximum solar-to-mechanical efficiency (for *GT2052*)

Figure 4.13 Temperature in the cycle at different receiver phase-change temperatures at maximum solar-to-mechanical efficiency (for *GT2860RS*)

Figure 4.12 shows that the temperatures in the cycle between the four different phase-change temperatures differed on average by 5 K to 110 K. These figures show how the temperature rose from State 1 to State 6, which includes the compressor, window, recuperator and the coiled tube. Furthermore, the air leaving the cycle (at Position 10) was still at a relatively high temperature, leaving much potential for cogeneration. Figure 1.3 indicates that the window was between States 2

61

and 3, thus, considering Figure 4.11 to Figure 4.13, the window increased the air temperature on average by about 210 K. The window thus preheated the air before it entered the recuperator and receiver.

Figure 4.14 to Figure 4.16 show the pressure at different positions in the cycle. Comparing the pressures of the three turbochargers, the *GT2052* had the highest pressure at the window inlet (State 2). For the *GT1241* turbocharger (Figure 4.14), the receiver phase-change temperature of 1100 K had a higher overall pressure than for all the other receiver phase-change temperatures. This was due to a higher optimum turbine pressure ratio at a receiver phase-change temperature of 1100 K, as shown in Table 4.2. The turbochargers considered in this study were very sensitive to differences in pressure and it was thus important to have the highest possible inlet pressure at the turbine of the turbocharger (State 7 in Figure 4.14 to Figure 4.16).
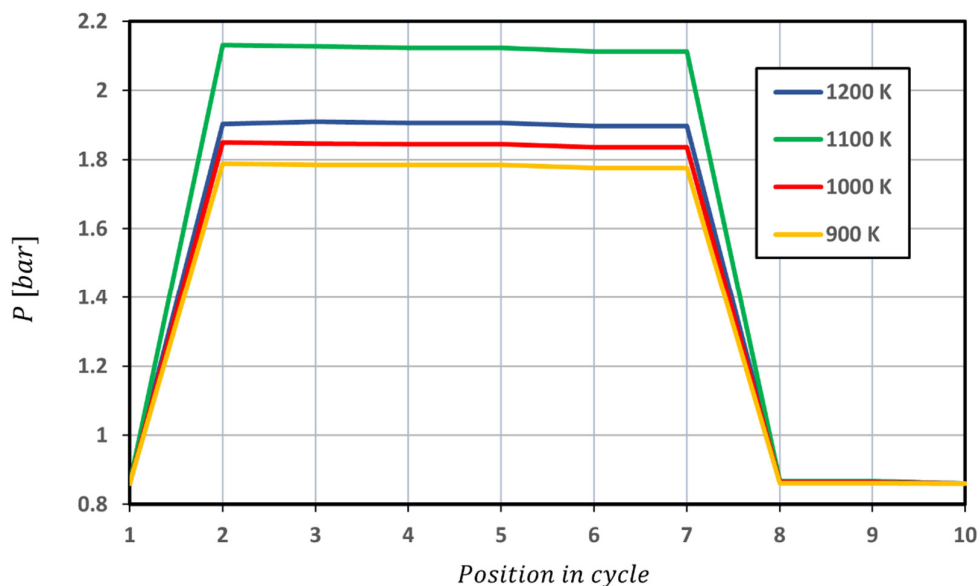
Figure 4.14 Pressure in the cycle at different receiver phase-change temperatures at maximum solar-to-mechanical efficiency (for *GT1241*)

Figure 4.15 shows, for example, that the compressor of the *GT2052* turbocharger compressed the air to about 2.1 bar from the ambient pressure of 0.86 bar at a receiver phase-change temperature of 1200 K. As the air flowed through the window, the recuperator and the coiled tube (States 2 to 7), the pressure drop ranged on average between 1.3 kPa and 6.4 kPa for each of the three turbochargers. On average, there was a relatively small pressure drop between the window and the coiled tube and this allowed for maximum inlet pressure at the turbine (State 7). The window accounted for between 0.4 kPa and 1.3 kPa of the total pressure drop in the cycle, which was considered acceptable in this study. It must be noted that for some of the receiver phase-change temperatures, the pressure in the cycle

62

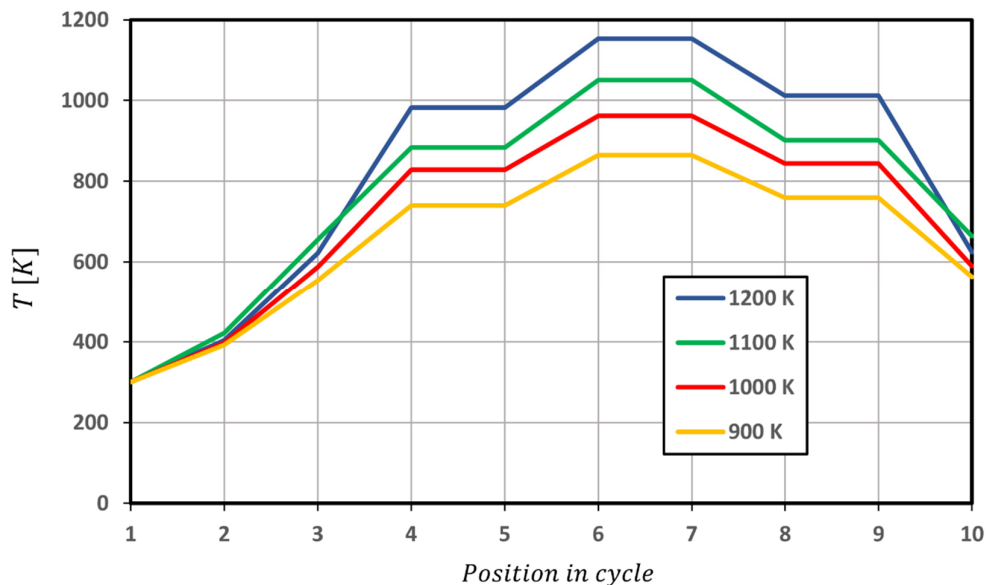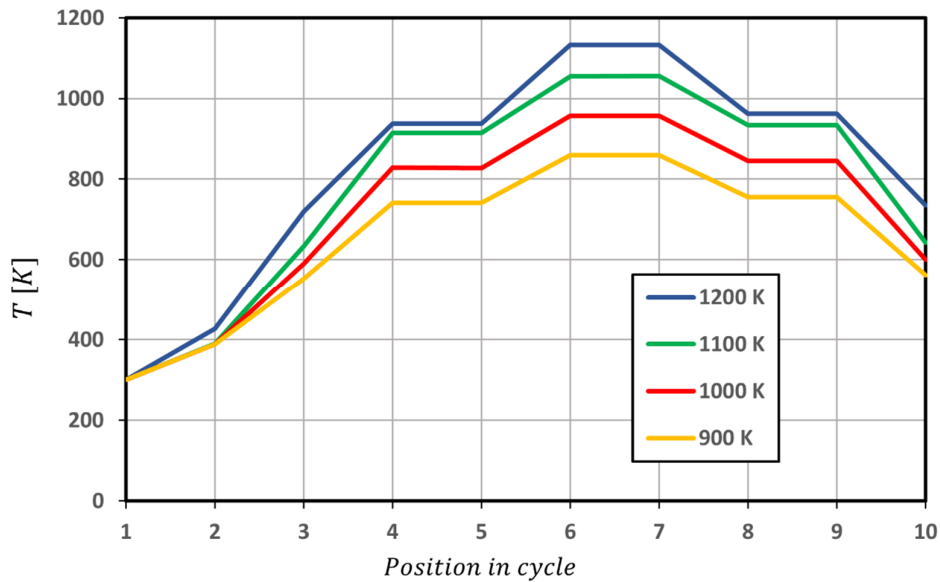was the same as for the other receiver phase-change temperatures and is thus not shown.
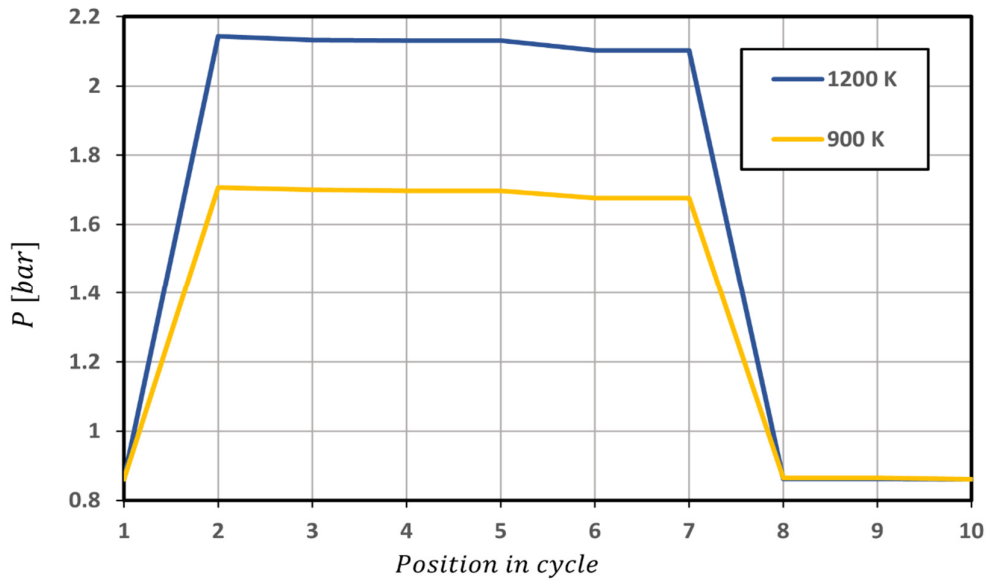
Figure 4.15 Pressure in the cycle at different receiver phase-change temperatures at maximum solar-to-mechanical efficiency (for *GT2052*)

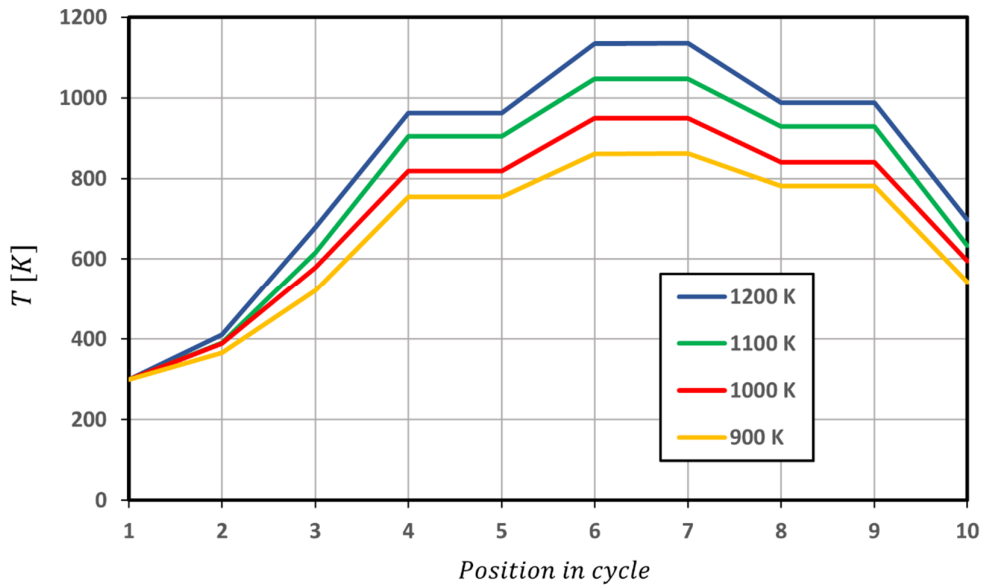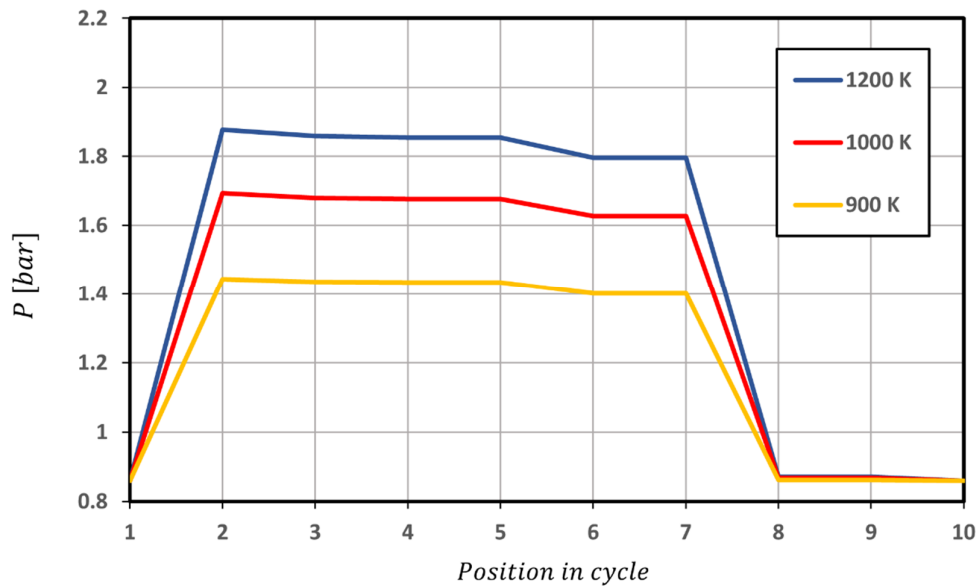**Figure 4.16 Pressure in the cycle at different receiver phase-change temperatures at maximum solar-to-mechanical efficiency (for *G2860RS*)**

Table 4.5 Performance at maximum solar-to-mechanical efficiency for *GT2052* at different surface temperatures

	900 K	1000 K	1100 K	1200 K
N **(rpm)**	135 000	135 000	135 000	162 000
$\dot{m}$ **(kg/s)**	0.0771	0.0731	0.0696	0.0878
η_t	0.692	0.681	0.669	0.671
η_c	0.736	0.729	0.723	0.704
r_c	1.992	1.9918	1.9926	2.4932
r_t	1.9375	1.9375	1.9375	2.4375
h_{rec} **(W/m²K)**	55.5	54.7	53.9	65.6
$h_{reg,h}$ **(W/m²K)**	135.8	145.7	155.4	109.8
$h_{reg,c}$ **(W/m²K)**	134.1	144.0	154.0	107.9
$h_{chn,ave}$ **(W/m²K)**	49.88	49.22	46.17	58.26

Table 4.5 shows the *GT2052* turbocharger's shaft speed, compressor and turbine efficiencies, compressor and turbine pressure ratios, and the heat transfer coefficients at different positions in the cycle when the cycle ran at maximum solar-to-mechanical efficiency and the recuperator had the dimensions shown in Table 4.3. The optimum speed at receiver temperatures of 900 K to 1100 K was 135 000 rpm and the optimum turbocharger speed at a receiver temperature of 1200 K was 162 000 rpm. The optimum mass flow rate for each receiver surface temperature at the maximum solar-to-mechanical efficiency was fairly the same at an average of about 0.07 kg/s. The turbine and compressor efficiencies were also relatively constant at an average of about 68% and 72% respectively.

4.3.2 Effect of channel width

The channel width of the air-cooled window should have a significant impact on the heat transfer rate between the window and the air due to a change in the velocity, Reynolds number, and heat transfer coefficient. A parametric analysis was conducted with the *GT2052* micro-turbine at a fixed pressure ratio of 1.938 and recuperator dimensions of $a = 450$ mm, $b = 1.5$ mm, $L_{reg} = 0.5\ m$ and $n = 45$ channels (90 channels in total). This allowed for easier comparison between the different receiver surface temperatures. The channel width was thus treated as a parameter and the air-cooled window's

64

pressure drop (from Positions 2 to 3 in Figure 1.3), temperature change, and the glass surface temperature were compared. The channel width that is mentioned in the results refers to the distance between two glass panes where the HTF passes in-between (see Figure 3.7). It was expected that as the channel width was increased, the pressure drop across the channel would decrease and the cooling effectiveness of the HTF would also decrease.

Figure 4.17 to Figure 4.20 show the results of the parametric analysis, which includes the pressure drop and temperature change across the cooling channel as well as the solar-to-mechanical efficiency and glass surface temperature.
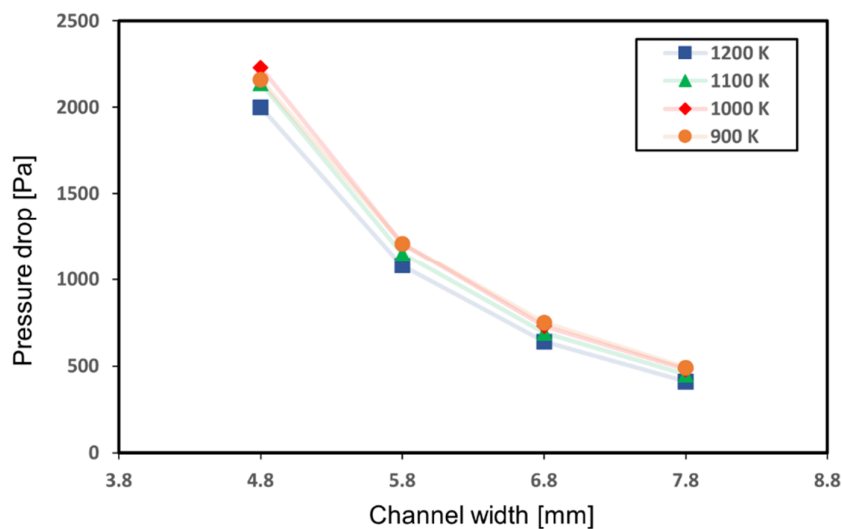
Figure 4.17 Pressure drop across the air-cooled window for different cooling channel widths and receiver phase-change temperatures (for *GT2052*)
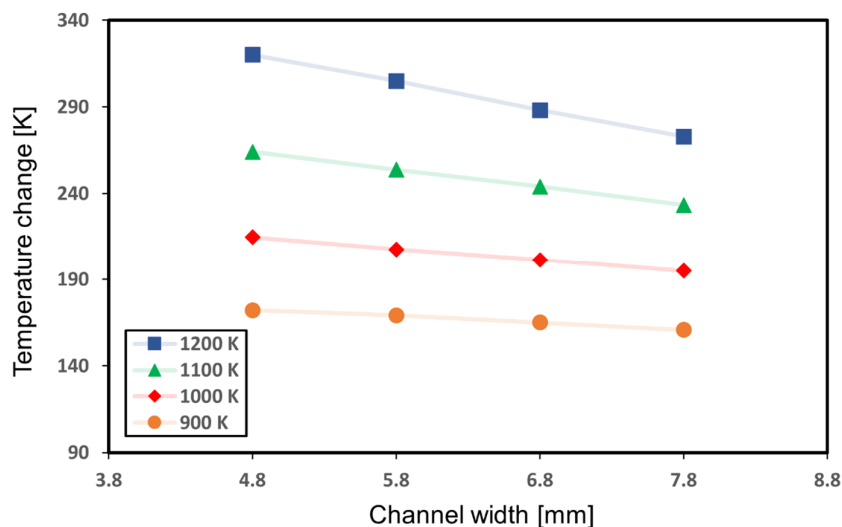
Figure 4.18 Temperature change of the HTF across the air-cooled window for different cooling channel widths and receiver phase-change temperatures (for *GT2052*)

65

Figure 4.17 shows that the pressure drop decreased as the channel width increased, whereas Figure 4.18 shows that the temperature change of the air as it flowed through the cooling channel decreased as the channel width increased. Thus, a smaller channel width will cool the glass panes better than a larger channel width; however, a smaller channel width will lead to an increased pressure drop across the air-cooled window, which can be detrimental to the micro-turbines considered in this cycle. A trade-off must be made between having effective cooling of the glass and having a low enough pressure drop to ensure maximum inlet pressure at the turbine.
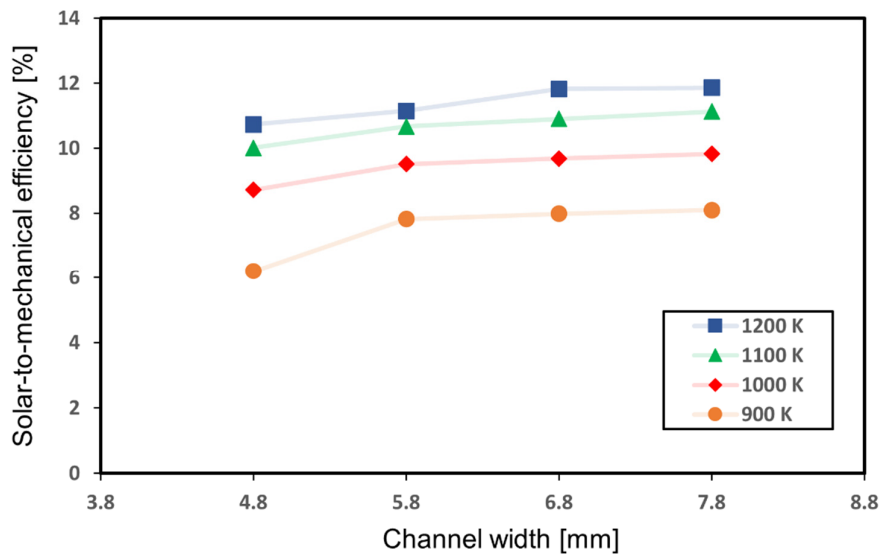
Figure 4.19 Solar-to-mechanical efficiency for different cooling channel widths and receiver phase-change temperatures (for *GT2052*)
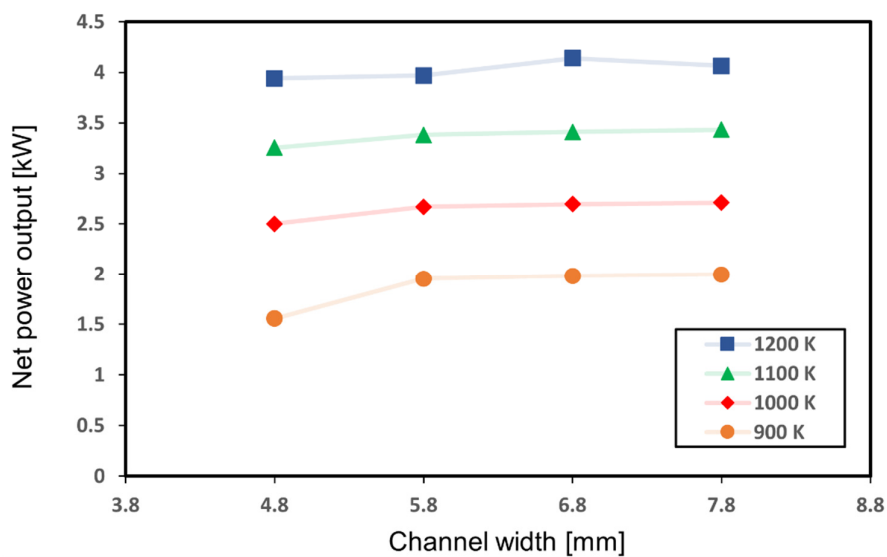
Figure 4.20 Net power output for different cooling channel widths and receiver phase-change temperatures (for *GT2052*)

66

Figure 4.19 and Figure 4.20 show the solar-to-mechanical efficiency and net power output as a function of the channel width. The solar-to-mechanical efficiency increased on average by about 1.3% and the net power output by about 0.24 kW as the channel width was varied from 4.8 mm to 7.8 mm. A larger channel width will thus be favourable when a large solar-to-mechanical efficiency and net power output are desired. Figure 4.19 and Figure 4.20 also indicate that for a channel width of above 5.8 mm, the change in the solar-to-mechanical efficiency and net power output between the different channel widths became small.

Figure 4.21 to Figure 4.24 show the average glass surface temperature for each division on one of the four sides of the receiver for a receiver phase-change temperature of 900 K to 1200 K. The top glass temperature is not included for display purposes. Only one of the four sides is shown because all four of the sides would have the same temperature due to the 0° dish tracking error assumption that was made. The glass surface temperature shown in Figure 4.21 to Figure 4.24 is an average over the two glass panes forming the cooling channel. A smaller channel width showed a lower average surface temperature per glass division and a lower receiver surface temperature also showed a lower average glass surface temperature. This was expected since the smaller channel width increased the velocity of the air and thus the Reynolds number of the flow. An increased Reynolds number led to an increased heat transfer coefficient on the inside of the cooling channel. As an example, if quartz glass was used for this application, with an average working temperature of about 1100 K, a channel width of 7.8 mm and a receiver phase-change temperature of 1200 K would produce a maximum glass surface temperature of 1115 K, which might be too high for the glass to handle (see Figure 4.24).
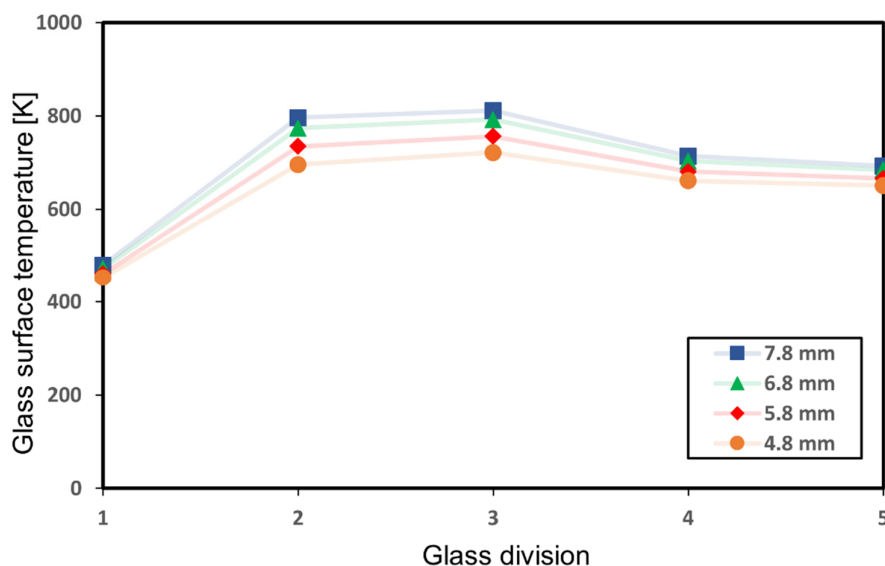
Figure 4.21 Glass surface temperature as a function of channel width for receiver phase-change temperature of 900 K (for *GT2052*)
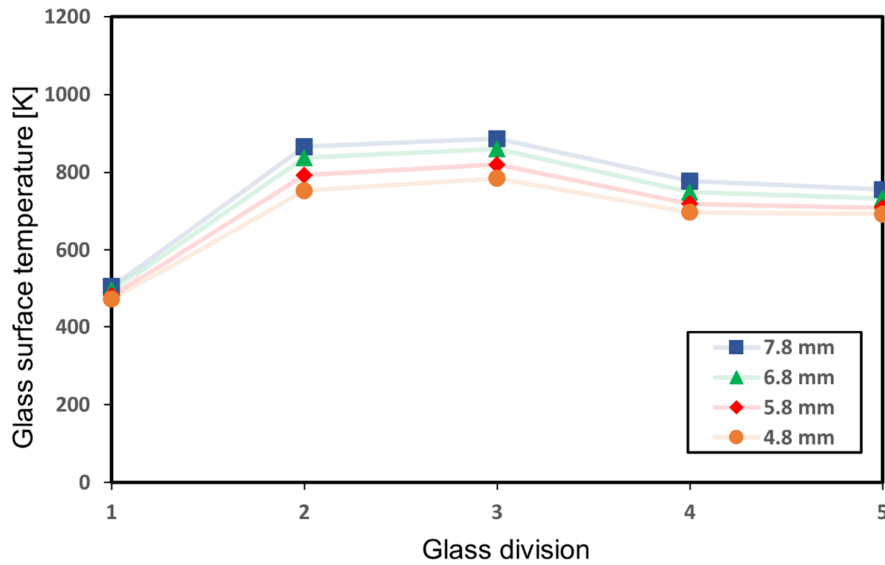
Figure 4.22 Glass surface temperature as a function of channel width for receiver phase-change temperature of 1000 K (for *GT2052*)
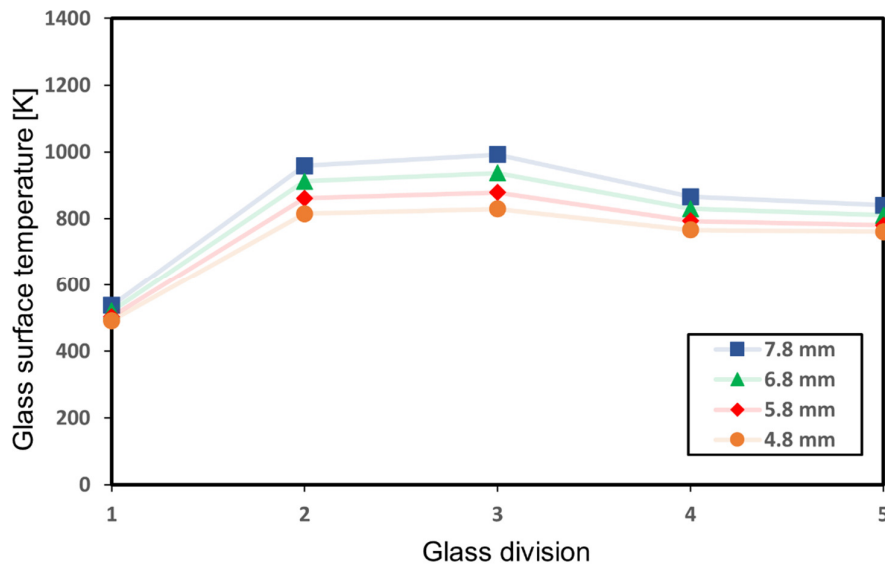
Figure 4.23 Glass surface temperature as a function of channel width for receiver phase-change temperature of 1100 K (for *GT2052*)

Figure 4.23 shows that for a channel width of 7.8 mm and receiver phase-change temperature of 1100 K, the highest average glass surface temperature was about 990 K, which would ensure that the glass average surface temperature was kept below 1100 K. Figure 4.21 indicates that for a 7.8 mm channel width and receiver phase-change temperature of 900 K, the highest average glass surface temperature was about 800 K, significantly lower than when a receiver temperature of 1100 K was used. Another interesting observation is that the highest glass surface temperature was on average

68

100 K lower than the relevant receiver phase-change temperature.
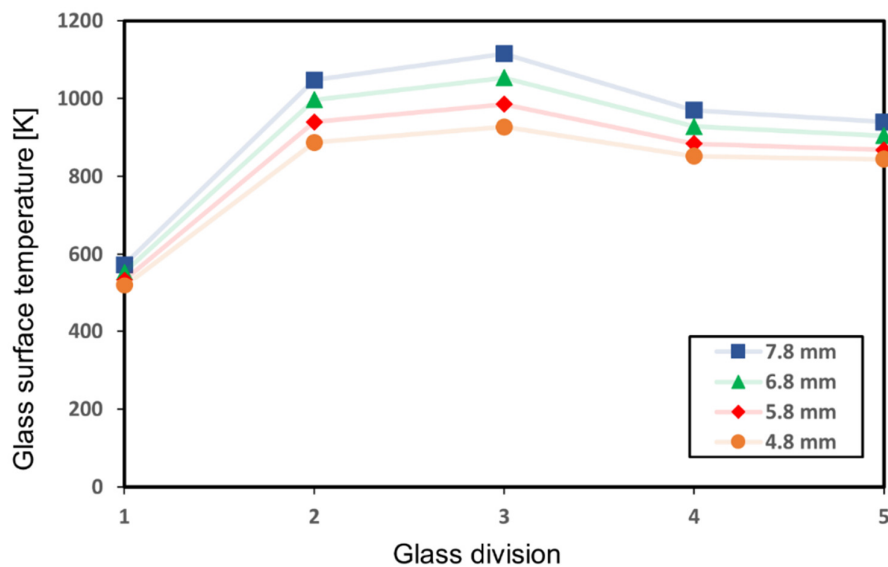
Figure 4.24 Glass surface temperature as a function of channel width for receiver phase-change temperature of 1200 K (for *GT2052*)

4.3.3 **Performance impact of window**

Table 4.6 to Table 4.8 summarise the optimum cycle properties with and without the proposed cooling window for each of the three different turbochargers. To compare the results of this study with the results of previous work by Le Roux and Sciacovelli (2019), in which the cycle had no window, the window code was simply added to the original code of Le Roux and Sciacovelli (2019) with the only modifications being that the recuperator length was allowed to range from 0.5 m to 3.5 m (instead of from 1.5 m to 4.5 m), as indicated in Table 3.3. In addition, lower tolerance of 0.01 for the iterations (higher resolution) was used (see Appendix F). The *EUF* was calculated as described in Section 3.7. Each row compares the results of the cycle without the window with the results of the cycle with the window for each turbocharger and receiver phase-change temperature. It should be noted that the properties given in Table 4.6 to Table 4.8 are for the optimum performance of the cycle (for maximum solar conversion efficiency).

For each of the turbochargers, a higher solar input power was required to reach maximum solar conversion efficiency than for the cycle without the window. Results also show that the maximum solar-to-mechanical efficiency was on average between 41% and 45% lower than that of the cycle without a window. However, the *EUF* was on average 9% to 11% higher than for the cycle without the cooling window. Note that a higher cycle exhaust temperature could lead to a higher *EUF* according to equation (3.32). The cycle exhaust temperature was on average 46%, 50% and 43%

69

higher (with temperature in Kelvin) for the *GT1241*, *GT2052* and *GT2860RS* turbochargers respectively. A higher *EUF* means that the cycle converts the available solar power more efficiently into usable power and heat. The window essentially also acts as a heat exchanger that preheats the air before it goes into the recuperator.

The optimum recuperator dimensions are shown in Table 4.6 to Table 4.8. Compared with the optimal recuperators in the cycles without the window, the optimal recuperators in the current study had the same dimensions for most of the results presented. The exceptions were at a receiver phase-change temperature of 900 K or 1200 K for all three turbochargers, where the recuperator channel height was about 0.8 mm larger than for the cycle without the window. Table 4.6 to Table 4.8 show that the optimum turbine pressure ratios were slightly different from the cycles without the cooling window, except for the *GT2052* turbocharger, which had the same optimum turbine pressure ratios.

Table 4.6 Comparison of cycle properties between the cycle with and without a cooling window for the *GT1241* turbo

Turbo	T_s (K)		$r_{t,opt}$	a_{reg} (mm)	b_{reg} (mm)	L_{reg} (m)	n	Mass (kg)	$\eta_{sol,max}$	$\dot{Q}^*_{tot}$ (kW)	$\dot{Q}_w$ (kW)	$\dot{W}_{net}$ (kW)	EUF
GT1241	900	Without window	2.063	450	1.5	0.5	45	325	0.127	9.0	3.5	1.1	51%
		With window	2.063	375	2.3	0.5	45	272	0.072	17.4	8.8	1.3	58%
	1000	Without window	2.188	450	1.5	0.5	45	325	0.158	11.5	3.9	1.8	50%
		With window	2.125	450	1.5	0.5	45	325	0.091	20.0	9.6	1.8	57%
	1100	Without window	2.188	450	1.5	0.5	45	325	0.175	13.3	3.8	2.3	46%
		With window	2.438	300	1.5	0.5	45	217	0.102	27.9	13.5	2.9	58%
	1200	Without window	2.438	450	1.5	0.5	45	325	0.182	17.8	4.9	3.3	46%
		With window	2.188	300	2.3	1.3	30	363	0.120	25.6	10.2	3.1	52%

Table 4.7 Comparison of cycle properties between the cycle with and without a cooling window for the *GT2052* turbo

Turbo	T_s (K)		$r_{t,opt}$	a_{reg} (mm)	b_{reg} (mm)	L_{reg} (m)	n	$Mass$ (kg)	$\eta_{sol,max}$	$\dot{Q}^*_{tot}$ (kW)	$\dot{Q}_w$ (kW)	$\dot{W}_{net}$ (kW)	EUF
GT2052	900	Without window	1.938	450	1.5	0.5	45	325	0.152	13.0	5.5	2.0	58%
		With window	1.938	450	1.5	0.5	45	325	0.080	24.8	13.3	2.0	62%
	1000	Without window	1.938	450	1.5	0.5	45	325	0.182	14.6	5.4	2.7	55%
		With window	1.938	450	1.5	0.5	45	325	0.097	27.8	14.5	2.7	62%
	1100	Without window	1.938	450	1.5	0.5	45	325	0.201	16.6	5.3	3.3	52%
		With window	1.938	450	1.5	0.5	45	325	0.110	31.3	15.8	3.5	61%
	1200	Without window	2.375	450	1.5	0.5	45	325	0.220	26.5	8.9	5.8	56%
		With window	2.375	450	2.3	0.5	45	326	0.123	49.6	25.2	6.1	63%

Table 4.8 Comparison of cycle properties between the cycle with and without a cooling window for the *GT2860RS* turbo

Turbo	T_s (K)		$r_{t,opt}$	a_{reg} (mm)	b_{reg} (mm)	L_{reg} (m)	n	$Mass$ (kg)	$\eta_{sol,max}$	$\dot{Q}^*_{tot}$ (kW)	$\dot{Q}_w$ (kW)	$\dot{W}_{net}$ (kW)	EUF
GT2860RS	900	Without window	1.625	450	1.5	0.5	45	325	0.149	12.8	5.5	1.9	57%
		With window	1.625	450	2.3	0.5	45	326	0.075	25.8	14.1	1.9	62%
	1000	Without window	2.125	450	1.5	0.5	45	325	0.176	27.9	12.6	4.9	63%
		With window	1.875	450	1.5	0.5	45	325	0.093	39.3	21.2	3.7	63%
	1100	Without window	1.875	450	1.5	0.5	45	325	0.198	23.2	8.8	4.6	58%
		With window	1.875	450	1.5	0.5	45	325	0.108	43.5	22.8	4.7	63%
	1200	Without window	2.125	450	1.5	0.5	45	325	0.215	33.5	12.6	7.2	59%
		With window	2.063	450	1.5	0.5	45	325	0.117	58.3	30.2	6.8	63%

The turbocharger that would produce the highest solar-to-mechanical efficiency for the cycle with a cooling window while still having acceptable required solar input was found to be the *GT2052*. The *GT2052* turbocharger allowed for the best performance at a turbine pressure ratio of 1.94 and a mass flow rate of 0.07 kg/s, with the recuperator dimensions being as follows: a channel width of 450 mm, channel height of 1.5 mm, channel length of 0.5 m, and 45 parallel flow channels (90 channels in total). A receiver phase-change temperature of 1100 K or below would achieve the maximum solar-to-mechanical efficiency while having an acceptable required solar input power (and thus dish size) and keeping the glass window cool enough for it to not shatter. It was also found that the cooling channel width had to be between 5 mm and 5.8 mm to keep the glass cool enough while maintaining an acceptable pressure drop across the cooling window. However, this conceptual study showed that it might not be feasible to implement the cooling window, except where a higher cycle exhaust temperature was preferred for cogeneration.

4.4   Summary

The demonstration of the numerical methods showed that the third glass division had the highest surface temperature, and the second glass division had the highest heat transfer rate to the air. The results showed that the air had gained significant heat as it moved through the channel. The results also indicated that the receiver phase-change temperature did make a difference in the glass surface temperature and net heat transfer rate. On average, the maximum solar-to-mechanical efficiencies of the cycle with the cooling window were between 41% and 45% lower than the cycle without a cooling window. The cycle with the window required a higher solar input power to produce the same net power as the cycle without a window. Results showed that a smaller cooling channel width (gap size) increased the cooling effectiveness and pressure drop while also decreasing the solar-to-mechanical efficiency of the cycle. However, a smaller cooling channel width also produced lower glass surface temperatures, which was very important for the structural integrity of the glass. The higher exhaust temperature of the cycle with the window led to a higher energy utilisation factor (*EUF*) than for the cycle without the window. The *EUF* was, on average, 9% to 11% higher; therefore, the cycle with the window had more potential for cogeneration, such as water heating or thermal energy storage.

Chapter 5

Conclusion

5.1 **Summary**

Small-scale solar thermal systems can provide renewable energy solutions to areas where grid access is limited. For the solar-dish Brayton cycle, off-the-shelf turbochargers were considered to reduce overall cycle costs (Le Roux et al., 2014a, Le Roux et al., 2014b). This research study analysed the impact of a cooling window, mounted on the inside of the solar receiver, on the performance of a solar-dish Brayton cycle using numerical methods. SolTrace was used to determine the solar heat flux on the window and the solar receiver. The entropy generation rate for each component in the cycle was identified and the total entropy generation rate of the cycle was derived. Using the total entropy generation rate and an exergy analysis on a control volume of the cycle, the net power output and the solar-to-mechanical efficiency were found. Various recuperator dimensions and various steady-state turbocharger operating points were considered, which allowed for finding the maximum solar-to-mechanical efficiencies. The optimum results were then compared with the optimum results of a cycle without a cooling window (Le Roux & Sciacovelli, 2019).

Results showed that a smaller cooling channel width (gap size) increased the cooling effectiveness as well as the pressure drop, while also decreasing the solar-to-mechanical efficiency of the cycle. However, a smaller cooling channel width also produced lower glass surface temperatures, which was very important for the structural integrity of the glass. Results showed that the maximum solar-to-mechanical efficiencies of the cycle with the cooling window were, on average, between 41% and 45% lower than for the cycle without a cooling window. The results also showed that the required solar input power and the cycle's exhaust temperature were higher than for the cycle without the window. The higher exhaust temperature of the cycle with the window led to a higher energy utilisation factor (*EUF*) than for the cycle without the window. The *EUF* was on average 9% to 11% higher, and therefore the cycle with the window had more potential for cogeneration, such as water heating or thermal energy storage.

73

The results showed that the *GT2052* turbocharger would produce the highest solar-to-mechanical efficiency in a cycle with a cooling window and a recuperator, while still having acceptable required solar input power. The *GT2052* turbocharger performed the best at a turbine pressure ratio of 1.94 and a mass flow rate of 0.07 kg/s, with the recuperator dimensions being as follows: a channel width of 450 mm, channel height of 1.5 mm, channel length of 0.5 m, and 45 parallel flow channels (90 channels in total). A receiver phase-change temperature of 1100 K or below would achieve the maximum solar-to-mechanical efficiency while having an acceptable required solar input power (and thus dish size) and keeping the glass window cool enough for it to not shatter (lower than 1100 K). The results also showed that the cooling channel width had to be between 5 mm and 5.8 mm to keep the glass at a temperature of 1100 K or lower while maintaining an acceptable pressure drop across the cooling window. However, this conceptual study showed that it might not be feasible to implement the cooling window, except where a higher cycle exhaust temperature was preferred for cogeneration.

5.2   Limitations

This conceptual study was limited to open and recuperated Brayton cycles using a parabolic solar dish (with a rim angle of 45°) to concentrate the solar irradiation onto an integrated open-cavity coiled-tube rectangular receiver with thermal storage, using an off-the-shelf Garret turbocharger as micro-turbine. For this study, two inner-cavity receiver windows were considered to form a cooling channel. A window thickness of 3 mm was considered to ensure that verifiable properties of the glass could be found. It was assumed that the glass panes that formed the channel had the same temperature on both sides of the glass pane. The conduction heat losses from the glass were assumed to be negligible. The width of the cooling channel was used as a parameter rather than a variable in the study to limit computational time. Various assumptions were also made in terms of the transmissivity, reflectivity and absorptivity of the glass, which could influence the overall performance impact of the window on the system. The linearisation of the radiation heat transfer terms used in the numerical method could also introduce small inaccuracies. Furthermore, it should be noted that the use of a glass channel has some practical implications. The glass has the potential to shatter or crack during long periods of high-temperature loads or very high-temperature gradients. The glass has to be cleaned regularly to ensure that the optical properties do not change and negatively impact the cycle.

74

5.3 **Recommendations for future work**

This research served as an initial conceptual study from which further work could be done. There are a few possibilities regarding future work. This study only investigated the cooling channel width as a parameter and future work could include the cooling channel width as a variable in the study. The recuperator variables in this study were limited to a specific range (for the sake of comparison with previous work) and possible future work could include a larger range of the variables to ensure a broader analysis of the cycle with the cooling window. A non-linear routine such as Newton's method could be used in future work to increase the accuracy of the glass surface temperature and net heat transfer rate calculations. The results of this study could be compared with CFD simulations to further validate the approach. Flow solver packages such as *Flownex* or *SimuPACT* could also be used to validate the numerical approach. Furthermore, future work could include experimentally testing the air-cooled window concept and comparing it with the results of this study. Lastly, it is recommended that a cost analysis and optimisation be done to further compare the cycle with and without the cooling window.

References

Bansal, N. P. & Doremus, R. H. 1986. Handbook of glass properties. Orlando: Academic Press.

Bejan, A. 1982. Extraction of exergy from solar collectors under time-varying conditions. *International Journal of Heat and Fluid Flow,* 3**,** 67-72.

Borgnakke, C. & Sonntag, R. E. 2014. *Fundamentals of thermodynamics,* 8th ed, Hoboken, NJ, John Wiley & Sons, Inc.

Çengel, Y. A. & Ghajar, A. J. 2015. *Heat and Mass Transfer: Fundamentals and Applications,* 5th ed, New York, McGraw Hill Education.

Clausing, A. M. 1981. An analysis of convective losses from cavity solar central receivers. *Solar Energy,* 27**,** 295-300.

Clausing, A. M. 1983. Convective losses from cavity solar receivers - comparisons between analytical predictions and experimental results. *Journal of Solar Energy Engineering,* 105**,** 29-33.

Coventry, J. & Andraka, C. 2017. Dish systems for CSP. *Solar Energy,* 152**,** 140-170.

Craig, K. J., Slootweg, M., Le Roux, W. G., Wolff, T. M. & Meyer, J. P. 2020. Using CFD and ray tracing to estimate the heat losses of a tubular cavity dish receiver for different inclination angles. *Solar Energy,* 211**,** 1137-1158.

Cui, F., He, Y., Cheng, Z. & Li, Y. 2013. Study on combined heat loss of a dish receiver with quartz glass cover. *Applied Energy,* 112**,** 690-696.

Dittus, F. W. & Boelter, L. M. K. 1930. Heat transfer in automobile radiators of the tubular type. *University of California Publications in Engineering,* 2**,** 443-481.

Fischer, S. & Hahne, E. 2000. The effect of different glass covers on the yearly energy gain of a solar collector. Stuttgart, Germany: University of Stuttgart.

Fuqiang, W., Jianyu, T., Lanxin, M. & Chengchao, W. 2014. Effects of glass cover on heat flux distribution for tube receiver with parabolic trough collector system. *Energy Conversion and Management,* 90**,** 47-52.

Garrett. 2009. *Garrett by Honeywell: Turbochargers, Intercoolers, Upgrades, Wastegates, Blow-Off Valves, Turbo Tutorials* [Online]. Available at: http://www.TurboByGarrett.com [Accessed 5 May 2022].

Garrett. 2021. *Garret Performance Turbo* [Online]. Available at: https://www.garrettmotion.com/racing-and-performance/performance-turbos/ [Accessed 7 June 2021].

76

Gavagnin, G., Rech, S., Sánchez, D. & Lazzaretto, A. 2018. Optimum design and performance of a solar dish microturbine using tailored component characteristics. *Applied Energy,* 231**,** 660-676.

Ghiaasiaan, S. M. 2011. Convective Heat and Mass Transfer. Cambridge University Press.

Glass Dynamics LLC. 2015. *Heat Resistant Glass* [Online]. Glass Dynamics LLC,. Available at: http://www.glassdynamicsllc.com/heatresistantglass.html [Accessed 29 October 2021].

Gnielinski, V. 1976. New equations for heat and mass transfer in turbulent pipe and channel flow. *International Chemical Engineering,* 16**,** 359-368.

Guzzella, L. & Onder, C. 2010. *Introduction to Modeling and Control of Internal Combustion Engine Systems,* 2nd ed, Heidelberg, Springer-Verlag Berlin

Harris, J. A. & Lenz, T. G. 1985. Thermal Performance of Solar Concentrator/Cavity Receiver Systems. *Solar Energy,* Vol. 34, No. 2**,** 135-142.

Jilte, R. D., Kedare, S. B. & Nayak, J. K. 2013. Natural convection and radiation heat loss from open cavities of different shapes and sizes used with dish concentrator *Mech Eng Res,* 3(1)**,** 25-43.

Karni, J., Kribus, A., Doron, P., Rubin, R., Fiterman, A. & Sagie, D. 1997. The DIAPR: A High-Pressure, High-Temperature Solar Receiver. *Journal of Solar Energy Engineering,* 119**,** 74-78.

Kribus, A. 1994. Optical Performance of Conical Windows for Concentrated Solar Radiation. *ASME Journal of Solar Energy Engineering,* 116**,** 47-52.

Lanchi, M., Montecchi, M., Crescenzi, T., Mele, D., Miliozzi, A., Russo, V., Mazzei, D., Misceo, M., Falchetta, M. & Mancini, R. 2015. Investigation into the Coupling of Micro Gas Turbines with CSP Technology: OMSoP Project. *Energy Procedia,* 69**,** 1317-1326.

Le Quere, P., Penot, F. & Mirenayat, M. 1981. Experimental study of heat loss through natural convection from an isothermal cubic open cavity. 40 avenue du Recteur Pineau, 86022 Poitiers Cédex, France: Laboratoire d'Energétique Solaire.

Le Roux, W. G. 2011. *Maximum Net Power Output from an Integrated Design of a Small-Scale Open and Direct Solar Thermal Brayton Cycle.* Dissertation: University of Pretoria.

Le Roux, W. G. 2015. *Thermodynamic optimisation and experimental collector of a dish-mounted small-scale solar thermal Brayton cycle.* Thesis: University of Pretoria.

Le Roux, W. G. 2018. Feasibility study of a hybrid small-scale dish-mounted solar thermal Brayton cycle with cogeneration. Proceedings of the 16th International Heat Transfer Conference (IHTC16-24185), Beijing, China. 7929-7936.

Le Roux, W. G., Bello-Ochende, T. & Meyer, J. P. 2011. Operating conditions of an open and direct

solar thermal Brayton cycle with optimised cavity receiver and recuperator. *Energy,* 36**,** 6027-6036.

Le Roux, W. G., Bello-Ochende, T. & Meyer, J. P. 2012a. Optimum performance of the small-scale open and direct solar thermal Brayton cycle at various environmental conditions and constraints. *Energy,* 46**,** 42-50.

Le Roux, W. G., Bello-Ochende, T. & Meyer, J. P. 2012b. Thermodynamic optimisation of an integrated design of a small-scale solar thermal Brayton cycle. *International Journal of Energy Research,* 36**,** 1088-1104.

Le Roux, W. G., Bello-Ochende, T. & Meyer, J. P. 2013. A review on the thermodynamic optimisation and modelling of the solar thermal Brayton cycle. *Renewable and Sustainable Energy Reviews,* 28**,** 667-690.

Le Roux, W. G., Bello-Ochende, T. & Meyer, J. P. 2014a. The efficiency of an open-cavity tubular solar receiver for a small-scale solar thermal Brayton cycle. *Energy Conversion and Management,* 84**,** 457-470.

Le Roux, W. G., Bello-Ochende, T. & Meyer, J. P. 2014. Optimisation of an open rectangular cavity receiver and recuperator used in a small-scale solar thermal Brayton cycle with thermal losses. 10th International Conference on Heat Transfer, Fluid Mechanics and Thermodynamics, Orlando, Florida. 499-507.

Le Roux, W. G. & Sciacovelli, A. 2019. Recuperated solar-dish Brayton cycle using turbocharger and short-term thermal storage. *Solar Energy,* 194**,** 569-580.

Li, X. L., Xia, X. L., Li, Z. H. & Chen, X. 2019. Effects of double windows on optical and thermal performance of solar receivers under concentrated irradiation. *Solar Energy,* 184**,** 331-344.

Lienhard IV, J. H. & Liendhard V, J. H. 2020. *A Heat Transfer Textbook,* 5th ed, Cambridge, Massachusetts, Phlogiston Press.

Lovegrove, K. & Pye, J. 2012. 2 - Fundamental principles of concentrating solar power (CSP) systems. *In:* LOVEGROVE, K. & STEIN, W. (eds.) *Concentrating Solar Power Technology.* Cambridge, United Kingdom: Woodhead Publishing.

MacGregor, R. K. & Emery, A. P. 1969. Free Convection Through Vertical Plane Layers: Moderate and High Prandtl Number Fluids. *Journal of Heat Transfer,* 91**,** 391.

Martínez, I. 2020. *Radiative View Factors* [Online]. Isidoro Martínez Academic web-site. Available at: http://webserver.dmt.upm.es/~isidoro/tc3/Radiation%20View%20factors.pdf [Accessed].

McDonald, C. G. 1995. Heat loss from an open cavity. *Report SAND95-2939.* Sandia Laboratory.

Mills, D. 2004. Advances in solar thermal electricity technology. *Solar Energy,* 76**,** 19-31.

78

Nellis, G. F. & Pfotenhauer, J. M. 2005. Effectiveness-NTU relationship for a counterflow heat exchanger subjected to an external heat transfer. *Journal of Heat Transfer,* 127**,** 1071-1073.

Paitoonsurikarn, S. & Lovegrove, K. 2003. On the study of convection loss from open cavity receivers in solar paraboloidal dish applications. Proceedings of the 40th ANZSES Conference, 26-29 November, Melbourne, Australia.

Paitoonsurikarn, S. & Lovegrove, K. 2006. A new correlation for predicting the free convection loss from solar dish concentrating receivers. Proceedings of 44th ANZSES Conference, 13-15 September, Canberra, Australia.

Paitoonsurikarn, S., Taumofeloau, T. & Lovegrove, K. 2004. Estimation of convection loss from paraboloidal dish cavity receivers. Proceedings of the 42nd ANZSES Conference, 28 November - 1 December, Perth, Australia.

Pendyala, R., Wong, Y. S. & Ilyas, S. U. 2015. CDF Simulations of Natural Convection Heat Transfer in Enclosures with Varying Aspect Ratios. *Chemical Engineering Transactions,* 45**,** 793-799.

Petukhov, B. S. 1970. Heat Transfer and Friction in Turbulent Pipe Flow with Variable Physical Properties. *In:* HARTNETT, J. P. & IRVINE, T. F. (eds.) *Advances in Heat Transfer.* Elsevier.

Pietsch, A. & Brandes, D. J. 1989. Advanced solar Brayton space power systems. Proceedings of the 24th Intersociety Energy Conversion Engineering Conference, 6-11 Aug. 1989. 911-916

Prakash, M., Kedare, S. B. & Nayak, J. K. 2009. Investigations on heat losses from a solar cavity receiver. *Solar Enegy,* 83**,** 157-170.

Röger, M., Pfänder, M. & Buck, R. 2006. Multiple Air-Jet Window Cooling for High-Temperature Pressurized Volumetric Receivers: Testing, Evaluation, and Modeling. *Journal of Solar Energy Engineering,* 128**,** 265-274.

Samanes, J., García-Barberena, J. & Zaversky, F. 2015. Modelling solar cavity receivers: a review and comparison of natural heat loss correlations *Energy Procedia,* 69**,** 543 - 552.

Schiel, W. & Keck, T. 2012. 9 - Parabolic dish concentrating solar power (CSP) systems. *In:* LOVEGROVE, K. & STEIN, W. (eds.) *Concentrating Solar Power Technology.* Cambridge, United Kingdom: Woodhead Publishing.

Schott. 2014. *Technical Glasses Brochure* [Online]. Mainz, Germany: Schott. Available at: https://www.schott.com/d/tubing/c3fb6f14-beae-4571-82bb-a989308ffe2a/1.3/schott-brochure-technical-glasses_english.pdf [Accessed].

Schott. 2021. *Robax Technical Details* [Online]. Available at: https://www.schott.com/en-hr/products/robax-p1000332/technical-details?tab=18d4d6cddc8d48988205f993579042c2

[Accessed 29 October 2021].

Shelby, J. E. & Lopes, M. 2005. *Introduction to Glass Science and Technology,* Cambridge, United Kingdom, Royal Society of Chemistry.

Stine, W. B. & Harrigan, R. W. 1985. *Solar energy fundamentals and design,* New York, USA, John Wiley and Sons, Inc.

Subedi, I., Silverman, T. J., Deceglie, M. G. & Podraza, N. J. 2019. Emissivity of solar cell cover glass calculated from infrared reflectance measurements. *Solar Energy Materials and Solar Cells,* 190**,** 98 - 102.

Too, Y. C. S., López, M. D., Cassard, H., Duffy, G., Benito, R. & Navio, R. 2017. Thermal performance and operation of a solar tubular receiver with CO2 as the heat transfer fluid. *Journal of Solar Energy Engineering,* 139**,** 041004-2 - 041004-9.

Uhlig, R., Flesch, R., Gobereit, B., Giuliano, S. & Liedke, P. 2014. Strategies Enhancing Efficiency of Cavity Receivers. *Energy Procedia,* 49**,** 538-550.

Uhlig, R. & Röger, M. 2004. Development of a window cooling for high-temperature solar receivers. *22nd CAD-FEM Users' Meeting 2004.* Germany: International Congress on FEM Technology.

Wang, P., Li, J. B., Bai, F. W., Liu, D. Y., Xu, C., Zhao, L. & Wang, Z. F. 2016. Experimental and theoretical evaluation on the thermal performance of a windowed volumetric solar receiver. *Energy,* 117**,** 652-661.

Wendelin, T., Dobos, A. & Lewandowski, A. 2013. SolTrace: a ray-tracing code for complex solar optical systems. National Renewable Energy Laboratory.

White, F. M. 2017. *Fluid mechanics,* 8th ed, New York, USA, McGraw Hill.

Appendix A

View factors

A.1 Rectangle 1 to Rectangle 2 in a parallel plane

This view factor relation is for the cells from one side of the cavity directly to the opposite side of the cavity. It can be from any cell to any cell if they are parallel to each other. Symmetry plays an important role and reduces the amount of code that is needed. This also includes the view factor from the back wall of the cavity to the aperture and vice versa. The rectangle's dimensions are described with the coordinate system shown in Figure A.1 and the view factor can be calculated by using equation (A.1) (Martínez, 2020):

$$F_{12} = \frac{1}{2\pi A_1} \sum_{l=1}^{2} \sum_{e=1}^{2} \sum_{j=1}^{2} \sum_{i=1}^{2} \left[(1)^{(i+j+e+l)} B(x_i, y_j, \delta_k, \xi_l) \right] \tag{A.1}$$

with:

$$A_1 = (x_2 - x_1)(y_2 - y_1) \tag{A.2}$$

$$B = vp \arctan\left(\frac{v}{p}\right) + uq \arctan\left(\frac{u}{p}\right) - \frac{z^2}{2} \ln(u^2 + v^2 + z^2) \tag{A.3}$$

and

$$\begin{aligned}
v &= y - \delta \\
u &= x - \xi \\
p &= \sqrt{u^2 + z^2} \\
q &= \sqrt{v^2 + z^2}
\end{aligned} \tag{A.4}$$

A.2 Rectangle 1 at 90° to Rectangle 2

This view factor applies to all the cells that share a common edge and are 90° to one another. This also includes all the view factors from the cells to the aperture or from the cells to the back wall. Equation (A.1) is also used for this view factor as well as equation (A.2) for the area A_1. However, the B function changes, which is given by equation (A.5) (Martínez, 2020). The dimensions and coordinate system used in the equations are shown in Figure A.2.

A.1

$$B = (y - \delta)\sqrt{x^2 + z^2} \arctan\left(\frac{(y - \delta)}{\sqrt{x^2 + z^2}}\right)$$

$$-\frac{1}{4}(x^2 + z^2 - (y - \delta)^2)\ln(x^2 + z^2 + (y - \delta)^2)$$

(A.5)
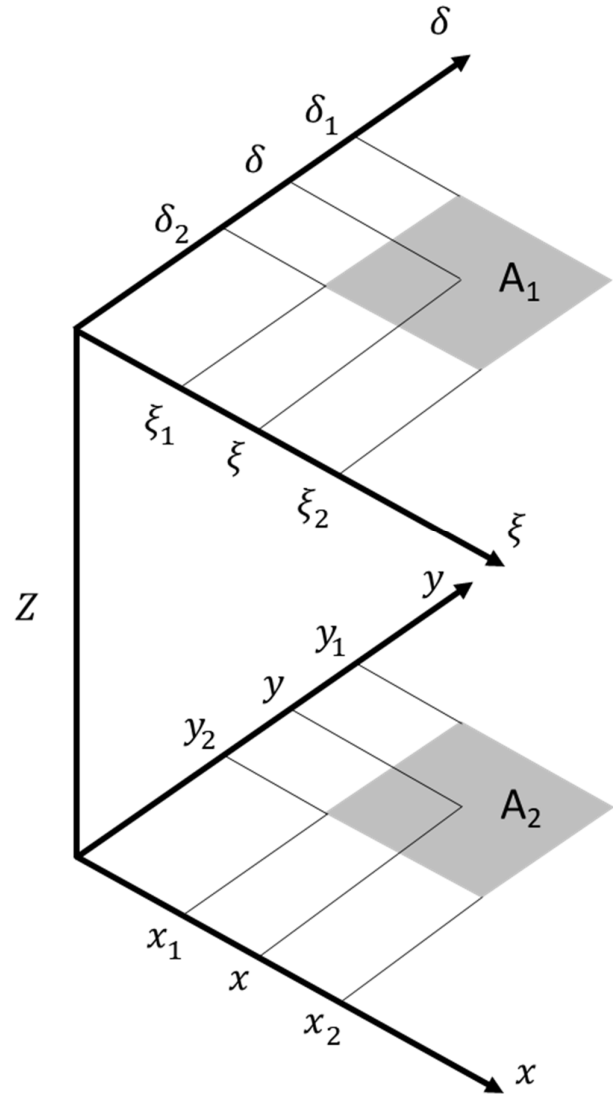
Figure A.1 View factor from Rectangles A_1 to A_2 in parallel plane (Martínez, 2020)
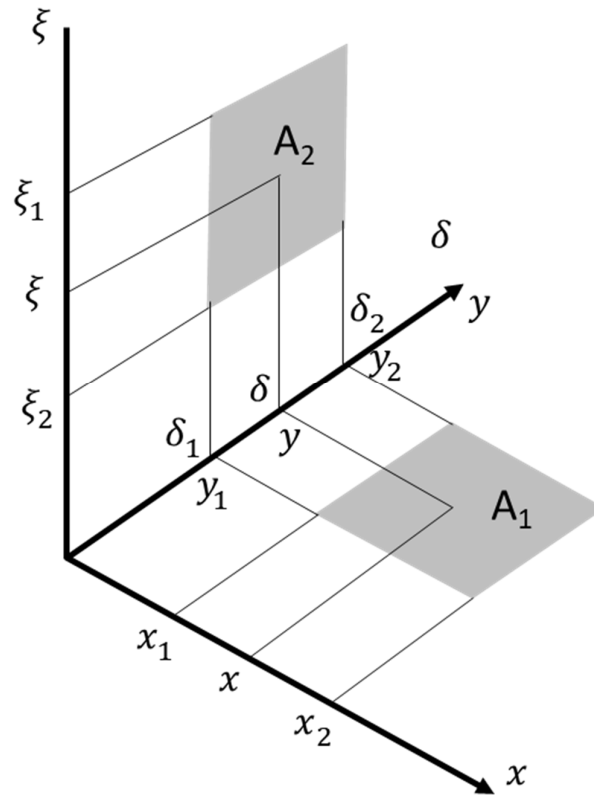
Figure A.2 View factor from Rectangles A_1 at 90° to A_2 (Martínez, 2020)

Appendix B
Model verification

The numerical method was verified by considering the difference between the calculation of the net power output with the exergy analysis, first law of thermodynamics and a heat balance. Equation (B.1) gives the net power output calculation using the first law of thermodynamics (with all the relevant assumptions). Equation (B.2) gives the net power output calculation using a heat balance on the control volume of the cycle. Note that F_1 and F_2 in equation (B.1) and (B.2) were merely identifiers used in the code and have no meaning inside the dissertation. Thus, equation (3.12) which was generated using an exergy analysis can be compared to equations (B.1) and (B.2) to validate to what accuracy the simulation is solving the relevant equations.

$$F_1 = \dot{m}c_{p,0}(T_7 - T_8) - \dot{m}c_{p,0}(T_2 - T_1)$$

(B.1)

$$F_2 = \dot{Q}_{tot}^* - \dot{m}c_{p,0}(T_{10} - T_1) - (\dot{Q}_{loss,win} + \dot{Q}_{loss,rec} + \dot{Q}_{loss,reg})$$

(B.2)

The parameters D_1 and D_2 were created in the code to represent the difference between the different calculations of $\dot{W}_{net}$.

$$D_1 = \left((\dot{W}_{net} - F_1)/F_1\right) * 100$$

(B.3)

$$D_2 = \left((\dot{W}_{net} - F_2)/F_2\right) * 100$$

(B.4)

Figure B.1 and Figure B.2 show the differences D_1 and D_2 as a function of the pressure ratio for the *GT2052* turbocharger. It is clear that both differences are almost the same and thus follow the same pattern. For the 900 K and 1000 K receiver phase-change temperatures, the differences have a steep decline from pressure ratios of 1.3 to about 1.5, from where the differences steadily climb to about 4 % at a pressure ratio of 2 and above. For the 1100 K and 1200 K receiver phase-change temperatures, the differences have a less steep decline at pressure ratios of 1.6 to 1.8, from where the differences again level off at about 4 %. The *GT2052* turbocharger calculations therefore have a much smaller difference at higher pressure ratios. This observation is also shown in Table 4.3, where the pressure ratio is high (2.38) which produces the optimum recuperator geometry and solar-to-mechanical efficiency.
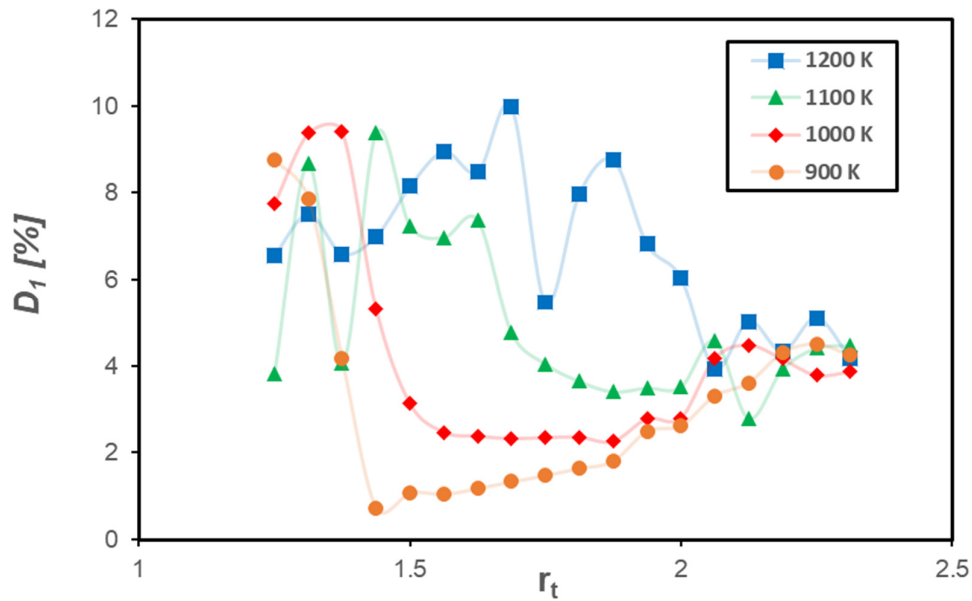
Figure B.1 Difference D_1 as a function of pressure ratio for *GT2052* turbocharger at maximum solar-to-mechanical efficiency
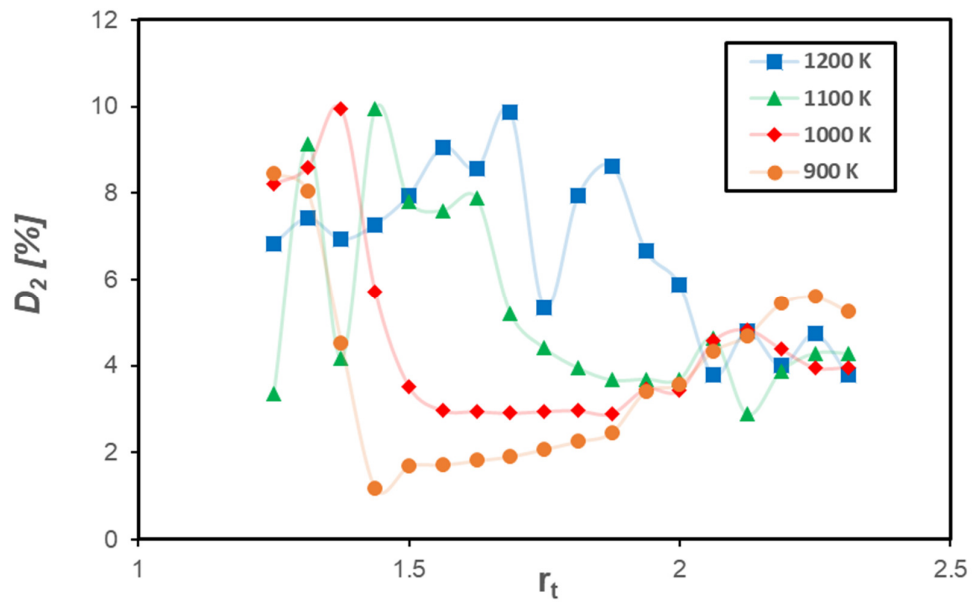
Figure B.2 Difference D_2 as a function of pressure ratio for *GT2052* turbocharger at maximum solar-to-mechanical efficiency

Table B.1 shows the differences D_1 and D_2 for different receiver temperatures and turbochargers corresponding to the geometries given in Table 4.2 to Table 4.4. The *GT1241* turbocharger's differences are on average larger than the other two turbochargers. The *GT2052* and *GT2860RS*

B.2

turbochargers have lower differences at lower receiver temperatures. The differences are attributed to the constant pressure specific heat values that were used throughout the simulations, instead of using enthalpy values. The constant pressure specific heat values were calculated at the average temperature of a specific point (as was done in the original code (Le Roux & Sciacovelli, 2019)). A difference of 10 % (for either D_1 or D_2) was considered to be acceptable to limit computational time. It took on average about 24 hours to run the code for one receiver temperature. The model was therefore verified based on the fact that the differences D_1 and D_2 were smaller than 10 % for each of the optimal points for each of the turbochargers.

Table B.1 Differences D_1 and D_2 for different receiver temperatures and turbochargers at optimal performance

	GT1241		GT2052		GT2860RS	
T_s [K]	D_1 [%]	D_2 [%]	D_1 [%]	D_2 [%]	D_1 [%]	D_2 [%]
900	9.1	9.8	1.8	2.5	1.1	1.7
1000	4.3	4.9	2.3	2.9	2.2	2.9
1100	9.7	9.7	3.4	3.7	2.6	3.0
1200	5.4	5.6	4.2	3.8	2.5	2.4

Appendix C

SolTrace script

```
// Directory where text file is saved
dir1 = "D:/ING/M-Ing/SolTrace/";
dir2 = "G:/SolTrace/";

cwd(dir1); // remember to change

start_timer();
/* ****************************************
              MAIN CONFIG
   **************************************** */
a_cav = 0.25; // cavity dimensions
t_gap = 0.065; // air gap width
t_gl = 3e-3; // glass thickness
t_chn = 6.8e-3; // channel width
R = 2.4;
D_dish = R*2; // Dish diameter
/* ****************************************
              SUN CONFIG
   **************************************** */
Sun.useldh = false;
Sun.hour = 10;

Sun.x = 0; //0 degree tracking error
Sun.y = 0;

//Sun.x = 1.746; //1 degree tracking error
//Sun.y = 1.746;
Sun.z = 100;
Sun.day = 0;
Sun.shape = 'p';
Sun.sigma = 2.67;
Sun.halfwidth = 4.65;
sunopt( Sun );

seed = 123;
amount_of_rays = 1000000;

/* ****************************************
        OPTICAL PROPERTIES CONFIG
   **************************************** */
clearoptics(); // remove any optical properties currently defined

addoptic('AL');
opticopt('AL', 1, {'refl'=0.9,'trans'=0.0,'errslope'=2,'errspec'=2});
opticopt('AL', 2, {'refl'=0.0,'trans'=0.0,'errslope'=2,'errspec'=2});

addoptic('Pipes');
opticopt('Pipes', 1, {'refl'=1.0,'trans'=1.0,'errslope'=2,'errspec'=2});
opticopt('Pipes', 2, {'refl'=1.0,'trans'=1.0,'errslope'=2,'errspec'=2});
```

```
opticopt('Glass_2', 2, {'refl'=0.0,'trans'=0.8,'errslope'=2,'errspec'=2,
    'refractr'=1.0});
addoptic('SS');
opticopt('SS', 1, {'refl'=0.15,'trans'=0.0,'errslope'=3,'errspec'=2});
opticopt('SS', 2, {'refl'=0.15,'trans'=0.0,'errslope'=3,'errspec'=2});

addoptic('SS-2');
opticopt('SS-2', 1, {'refl'=0.15,'trans'=0.0,'errslope'=3,'errspec'=2});
opticopt('SS-2', 2, {'refl'=1.0,'trans'=0.0,'errslope'=3,'errspec'=2});

/* ******************************************
                ADD ELEMENTS
   ****************************************** */
clearstages(); // clear the system
addstage( 'Stage_Complete' );

// we need to set the current stage to be active so we can add elements to
it
activestage( 'Stage_Complete' );

fc = sqrt((R^2*(1+cosd(45))^2)/(4*sind(45)^2));
c = 1/(2*fc);

addelement(); // adds parabolic dish element
elementopt( 0, {'en'=true, 'x'=0, 'y'=0, 'z'=0 ,
    'ax'=0, 'ay'=0, 'az'=1,
    'zrot'=0, 'aper'=['c',D_dish,0,0,0,0,0,0,0],
    'surf'=['p',c,c,0,0,0,0,0,0],
    'interact'='reflection',
    'optic'='AL',
    'comment'='parabolic dish'} );

zw = fc - 0.1 + 0.11715*sind(45)+0.5;

addelement(); // adds top wall element
elementopt( 1, {'en'=true, 'x'=0, 'y'=0, 'z'=zw+t_chn+0.005 ,
    'ax'=0, 'ay'=0, 'az'=1,
    'zrot'=0, 'aper'=['r',0.6278,0.6278,0,0,0,0,0,0],
    'surf'=['f',0,0,0,0,0,0,0,0],
    'interact'='reflection',
    'optic'='SS-2',
    'comment'='Top wall 1'} );

addelement(); // adds inner top glass element
tt = 2*((a_cav/2)+2*t_gl+t_chn+t_gap);
elementopt( 2, {'en'=true, 'x'=0, 'y'=0, 'z'=zw ,
    'ax'=0, 'ay'=0, 'az'=1,
```

C.2

```
'comment'='Top Glass 2'} );
tx = [-1,1,0,0];
ty = [0,0,-1,1];
sw1 = 0.3139;
sw2 = fc + sw1 - 0.07;
zr = [0,0,90,90];
for (i=4;i<8;i++){
    addelement(); // adds side wall elements
    elementopt( i, {'en'=true, 'x'=-1*sw1*tx[i-4], 'y'=-1*sw1*ty[i-4],
        'z'=sw2,
        'ax'=tx[i-4], 'ay'=ty[i-4], 'az'=sw2,
        'zrot'=zr[i-4], 'aper'=['r',0.67639,0.6278,0,0,0,0,0,0],
        'surf'=['f',0,0,0,0,0,0,0,0],
        'interact'='reflection',
        'optic'='pipes',
        'comment'='Side wall-'+(i-3)} );
    }
aa = 31;
x = 0.11715*sind(59);
sw3 = 0.1625;
sw4 = fc - 0.1 + x/2;
ab = sw3*tan(aa*pi()/180);
az = sw4 - ab;
zr1 = [0,0,90,90];
for (j=8;j<12;j++){
    addelement(); // adds aperture inclined elements
    elementopt( j, {'en'=true, 'x'=-1*sw3*tx[j-8], 'y'=-1*sw3*ty[j-
8],'z'=sw4,
        'ax'=0, 'ay'=0, 'az'=az,
        'zrot'=zr1[j-8], 'aper'=['r',0.11715,0.5,0,0,0,0,0,0],
        'surf'=['f',0,0,0,0,0,0,0,0],
        'interact'='reflection',
        'optic'='SS',
        'comment'='Aperture-'+(j-7)} );
    }
sw5 = 0.2535;
sw6 = fc-0.1;
for (j=12;j<16;j++){
    addelement(); // adds aperture flat elements
    elementopt( j, {'en'=true, 'x'=sw5*tx[j-12], 'y'=sw5*ty[j-12], 'z'=sw6
',
        'ax'=sw5*tx[j-12], 'ay'=sw5*ty[j-12], 'az'=0,
        'zrot'=zr1[j-12], 'aper'=['r',0.107,0.6278,0,0,0,0,0,0],
        'surf'=['f',0,0,0,0,0,0,0,0],
        'interact'='reflection',
        'optic'='SS',
        'comment'='Aperture,flat-'+(j-11)} );
```

C.3

```
        'surf'=['f',0,0,0,0,0,0,0,0],
            'interact'='reflection',
            'optic'='SS-2',
            'comment'='Bottom ins-'+(j-15)} );
        }
// adds glass division elements for outer pane
hg = 0.1;
sw7 = a_cav/2;
sw8 = [sb2+hg/2,sb2+3/2*hg,sb2+5/2*hg,sb2+7/2*hg,sb2+9/2*hg,
    sb2+hg/2,sb2+3/2*hg,sb2+5/2*hg,sb2+7/2*hg,sb2+9/2*hg,
    sb2+hg/2,sb2+3/2*hg,sb2+5/2*hg,sb2+7/2*hg,sb2+9/2*hg,
    sb2+hg/2,sb2+3/2*hg,sb2+5/2*hg,sb2+7/2*hg,sb2+9/2*hg];
txg = [1,1,1,1,1,-1,-1,-1,-1,-1,0,0,0,0,0,0,0,0,0,0];
tyg = [0,0,0,0,0,0,0,0,0,0,1,1,1,1,1,-1,-1,-1,-1,-1];
zrg = [0,0,0,0,0,0,0,0,0,0,90,90,90,90,90,90,90,90,90,90];
for (j=20;j<40;j++){
    addelement();
    elementopt( j, {'en'=true, 'x'=sw7*txg[j-20], 'y'=sw7*tyg[j-20],
        'z'=sw8[j-20] ,'ax'=-1*txg[j-20], 'ay'=-1*tyg[j-20], 'az'=sw8[j-
20],
        'zrot'=zrg[j-20], 'aper'=['r',hg,a_cav,0,0,0,0,0,0],
        'surf'=['f',0,0,0,0,0,0,0,0],
        'interact'='refraction',
        'optic'='Glass_1',
        'comment'='Glass_outer_A_'+(j-19)} );
    }
sw9 = sw7+t_gl;
t1 = a_cav+2*t_gl;
for (j=40;j<60;j++){
    addelement();
    elementopt( j, {'en'=true, 'x'=sw9*txg[j-40], 'y'=sw9*tyg[j-40],
        'z'=sw8[j-40] ,'ax'=-1*txg[j-40], 'ay'=-1*tyg[j-40], 'az'=sw8[j-
40],
        'zrot'=zrg[j-40], 'aper'=['r',0.1,t1,0,0,0,0,0,0],
        'surf'=['f',0,0,0,0,0,0,0,0],
        'interact'='refraction',
        'optic'='Glass_2',
        'comment'='Glass_outer_B'+(j-39)} );
    }
// adds glass division elements for inner pane
sw10 = sw9+t_chn;
t2 = t1+2*t_chn;
for (j=60;j<80;j++){
    addelement();
    elementopt( j, {'en'=true, 'x'=sw10*txg[j-60], 'y'=sw10*tyg[j-60],
        'z'=sw8[j-60] ,'ax'=-1*txg[j-60], 'ay'=-1*tyg[j-60], 'az'=sw8[j-
60],
        'zrot'=zrg[j-60], 'aper'=['r',0.1,t2,0,0,0,0,0,0],
        'surf'=['f',0,0,0,0,0,0,0,0],
```

C.4

```
'surf'=['f',0,0,0,0,0,0,0,0],
        'interact'='refraction',
        'optic'='Glass_2',
        'comment'='Glas_inner_B'+(j-79)} );
    }
sw12 = sw11+t_gap;
for (j=100;j<120;j++){
    addelement(); // adds receiver wall division elements
    elementopt( j, {'en'=true, 'x'=sw12*txg[j-100], 'y'=sw12*tyg[j-100],
        'z'=sw8[j-100] ,'ax'=-1*txg[j-100], 'ay'=-1*tyg[j-100],
        'az'=sw8[j-100],'zrot'=zrg[j-100],
        'aper'=['r',0.1,sw12*2,0,0,0,0,0,0],
        'surf'=['f',0,0,0,0,0,0,0,0],
        'interact'='reflection',
        'optic'='SS',
        'comment'='Rec wall-'+(j-99)} );
    }
/* ******************************************
                START TRACE
   ****************************************** */
traceopt({'rays'=amount_of_rays,'maxrays'=10*amount_of_rays,
    'cpus'=4,'seed'=seed } );
trace();
n = nelements();
ppr = 0.0180952; // MUST CHANGE EACH TIME!!!!
ppr_ar = "";
fileID = 'Power_of_rays_1.txt';
if (file_exists(fileID)){
    remove_file(fileID);}
for (i=1;i<n;i++){
    ppr_ar = ppr_ar + to_string(rayhits( 0, i, true )*ppr) + "\n";
    ok = write_text_file(dir1+fileID,ppr_ar); // remember to change
    if (!ok) outln("Error writing text file.");
}
out('Script took ' + elapsed_time()/1000+' seconds to complete');
```

Appendix D

Compressor and turbine maps

D.1 *GT1241* **turbocharger turbine map**
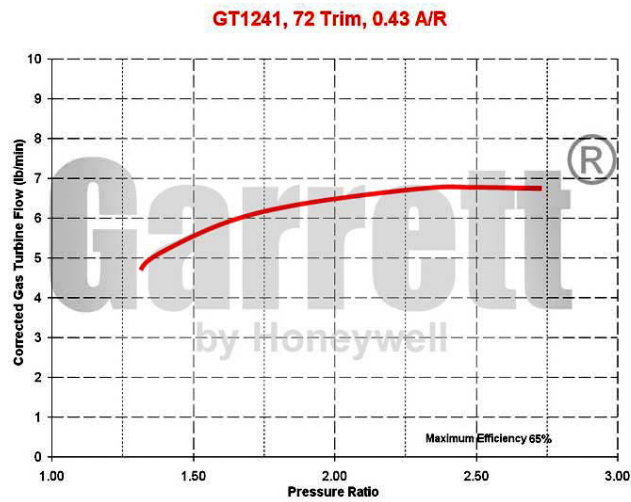
Figure D.1 *GT1241* **turbocharger turbine map (Garrett, 2009)**

D.2 *GT1241* **turbocharger compressor map**
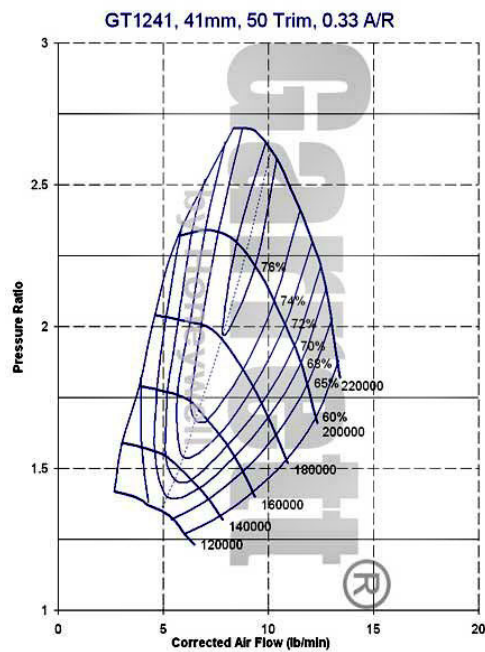
Figure D.2 *GT1241* **turbocharger compressor map (Garrett, 2009)**

D.1

D.3   GT2052 turbocharger turbine map
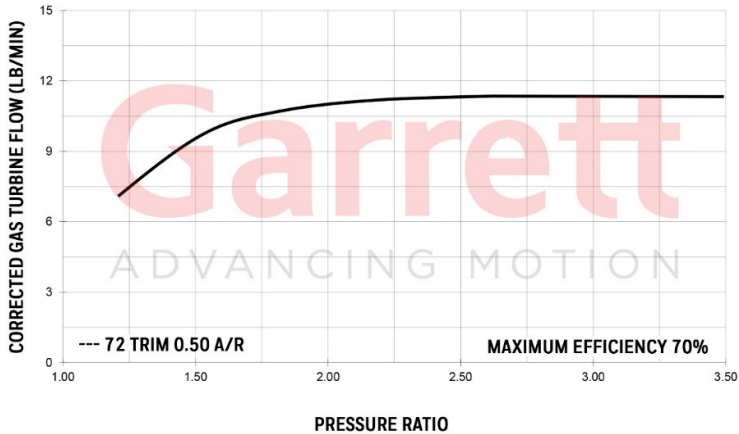
Figure D.3 *GT2052* **turbocharger turbine map (Garrett, 2021)**

D.4   GT2052 turbocharger compressor map
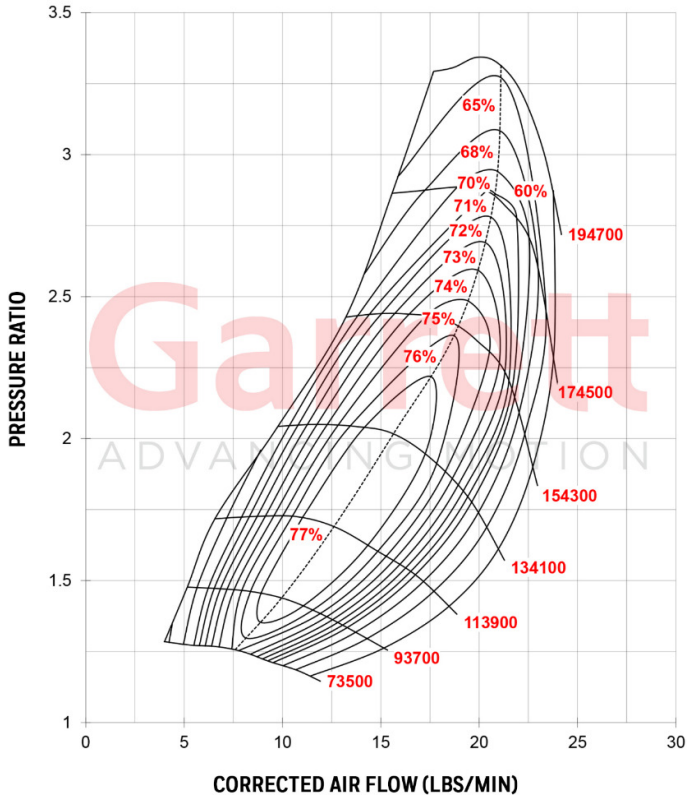
Figure D.4 *GT2052* **turbocharger compressor map (Garrett, 2021)**

D.5 *GT2860RS* turbocharger turbine map
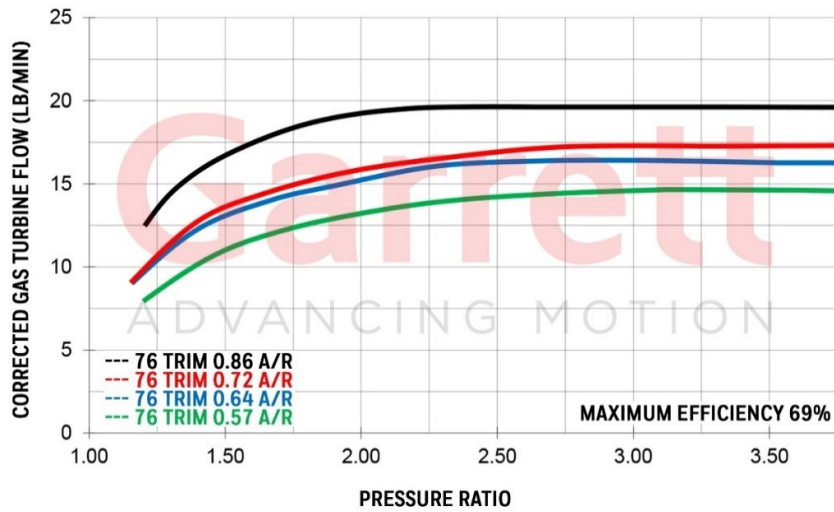
Figure D.5 *GT2860RS* **turbocharger turbine map (Garrett, 2021)**

D.6 *GT2860RS* turbocharger compressor map
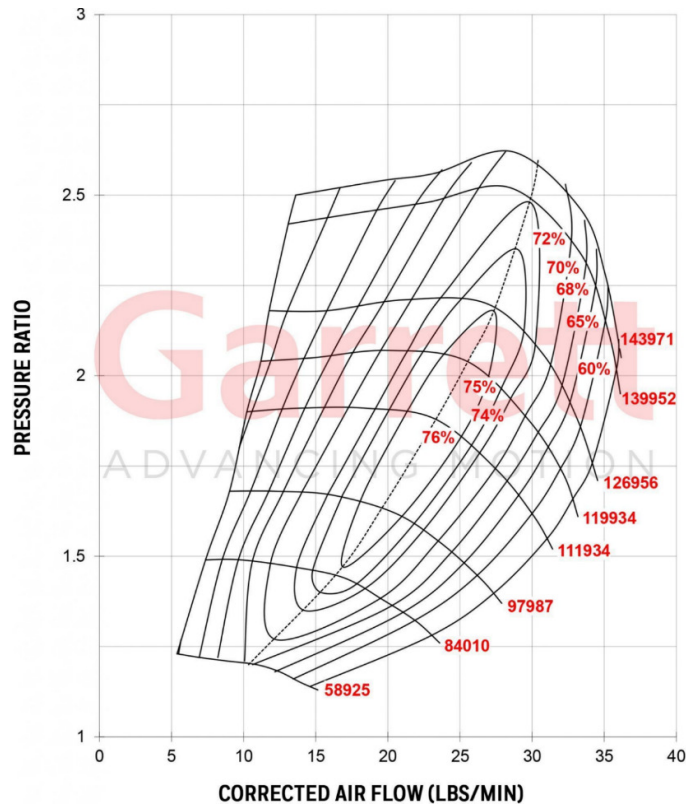
Figure D.6 *GT2860RS* **turbocharger compressor map (Garrett, 2021)**

Appendix E

Code structure

E.1   Glass model code structure

The glass is divided into several cells to calculate a temperature profile. Figure 3.9 shows the numbering system that was used. The number of divisions was calculated using the height of the receiver and dividing it by the number of divisions desired, this was then multiplied by four, to account for the four sides. This simple formula is shown in equation (D.1):

$$N = \frac{H}{N_{div}} * 4 \tag{D.1}$$

For this study, the number of divisions was taken as $N = \frac{0.5}{5} * 4 = 20$. Equation (D.1) allows the user to increase the number of divisions, thus increasing the accuracy of the surface temperature calculation. This is like a CFD computation where the user increases the mesh cell count to increase the solution accuracy.

The code that was used to solve the glass surface temperatures and net heat transfer rates was written in terms of functions because this enabled the user much more thorough debugging. The functions had the following form:

```
function [Outputs] = Function_name(Inputs)
        % Execute code
end
```

The function was then called by using the line: `[Outputs] = Function_name(Inputs)`. The heat transfer coefficient calculations used the equations as described in Section 3.4.3, the inputs were the fluid properties, which were also found by functions that were dependent on temperature. The full code is shown in Appendix F and a summary of the code is shown in Table E.2. The view factor function was coded with a certain structure, which is summarised in Table E.3 and the complete code can be found in Appendix F.

Table E.2 Heat transfer coefficient in cavity code structure

```matlab
function [Outputs] = HT_coeff_cavity(Inputs)
      % Define know values such as
        the constants a, b and ψ
      % See section 3.4.3
      % Calculate the ensemble length
            % use equation (3.23)
      % Calculate Rayleigh number
            % Ra = Gr*Pr
      % Calculate Nusselt number
            % use equation (3.24)
      % Calculate heat transfer coefficient
            % use equation (2.3)
end
```

Table E.3 View factor code structure

```matlab
function [Outputs] = View_Factor(Inputs)
      % Define coordinates of each cell
      % Calculate areas of cells
      % Calculate parallel rectangle view factors
            % use equation (A.1) and (A.3)
      % Calculate perpendicular rectangle view factors
            % use equation (A.1) and (A.5)
      % Calculate view factor to backwall/aperture
            % use equation (A.1) and (A.5)
      % Use symmetry to set up view factor matrix
            % matrix size depends on number of cells
end
```

The Gauss matrix that was used to solve the net heat transfer rates and the surface temperatures also had a degree of symmetry and for-loops could be used extensively to increase the coding efficiency. The Gauss matrix was set up in the following manner $\bar{A}x = \bar{B}$, where x consisted of the number of unknown surface temperatures and net heat transfer rates, the exact number depended on the number of divisions that were chosen (equation (D.1)). For the number of unknowns of 20, the coefficient matrix, $\bar{A}$ had a size of 40×40, and the constant matrix, $\bar{B}$ had a size of 40×1. Equation (3.35) and

E.2

equation (3.38) were rewritten in the form of $Ax = B$ and is given by equation (D.2) and equation (D.3):

$$\dot{Q}_{net,n} + T_{s,n}(A\varepsilon\sigma m_1) - A\varepsilon\sigma \sum_{j=1}^{N} F_{n-j} m_1 T_{s,j} + h_{air} A T_{s,n} =$$

$$\dot{Q}^* - A\varepsilon\sigma c_1 + A\varepsilon\sigma c_1 \sum_{j=1}^{N} F_{n-j} - A\varepsilon\sigma F_{n-\infty} T_\infty^4 + h_{air} A T_\infty \qquad (D.2)$$

$$T_{s,n} - \dot{Q}_{net,n}\left(\frac{1}{hA} + \frac{1}{2\dot{m}c_{p,0}}\right) - \sum_{i=1}^{N-1}\left(\frac{\dot{Q}_{net,i}}{\dot{m}c_{p0}}\right) = T_{in,0} \qquad (D.3)$$

The above equations were then used to set up the matrices in Octave. The code structure is shown in Table E.4 (the complete code can be found in Appendix F).

Table E.4 Code structure for Gauss matrix set-up

```
function [A,B] = Gauss_Matrix(Inputs)
      % Set up B matrix
            % Matrix size is 1 x Number of divisions
            % Use constants from equation (D.2) and equation (D.3)
      % Set up A Matrix
            % First half consists of the unknown
              coefficients of equation (D.3)
            % Second half consists of the unknown
              coefficients of equation (D.2)
            % Only the top diagonal are setup
            % Matrix is then mirrored about diagonal
end
```

All the above-mentioned functions were then used in the '*main*' code to calculate the surface temperatures and net heat transfer rates. Various other quantities were also calculated such as radiation and convection heat losses and air outlet temperatures at each 'cell'. The code structure for the full code is shown in Table E.5 (the full code is also displayed in Appendix F).

Table E.5 Main code structure

E.3

```matlab
function [Outputs] = window(Inputs)

%=====================================================%
%%%%%%%%%%%%%%%%%%%%% INPUTS %%%%%%%%%%%%%%%%%%%%%%%%
%=====================================================%
% All inputs are defined based on their name
%=====================================================%
%%%%%%%%%%%%%%%%%% ASSUMPTIONS %%%%%%%%%%%%%%%%%%%%%%%%
%=====================================================%
% All assumptions are defined/stated


%=====================================================%
%%%%%%%%%%%%%%%%%%%%%% KNOWNS %%%%%%%%%%%%%%%%%%%%%%%%
%=====================================================%
% All the known values are defined
%=====================================================%
%%%%%%%%%%%%%%%%%%%%%%% CALCS %%%%%%%%%%%%%%%%%%%%%%%%
%=====================================================%
% All the calculations are performed here
% Solar radiation heat flux imported from SolTrace

% The relevant functions are called such as:
%% Heat transfer coefficients, fluid properties,
%% View factors and Gauss Matrix functions

% The surface temperature and net
% heat transfer is calculated
%% Octave's backslash command is used, i.e., X = A\B

% The outlet air temperature is calculated
%% Use equation (3.39)

% The heat losses from the glass are calculated
%% Radiation and convection heat losses
%=====================================================%
%%%%%%%%%%%%%%%%%% SANITY CHECKS %%%%%%%%%%%%%%%%%%%%%
%=====================================================%
% Sanity checks are done to ensure Gauss Elimination
% worked correctly
%% Equation (3.39) is used
```

E.4

```
%=======================================================%
%%%%%%%%%%%%%%%%%%%%%% OUTPUTS %%%%%%%%%%%%%%%%%%%%%%%%%
%=======================================================%
% Plot necessary graphs and print console outputs
% for better reading and understanding
end
```

E.2   Complete cycle code structure

The turbine pressure ratio was used as a parameter in the code. A function called '*once*' was used to initialise all the turbocharger's turbine maps, the recuperator starting geometry and some of the environmental constants as well as calling the optimisation functions and saving the results to a text file. This function had a similar structure to the one written by Le Roux and Sciacovelli (2019), with a few changes to include the window. The function '*once*' allows the user to select one of three different settings. The first setting allows the user to input a specific turbine pressure ratio and recuperator geometry, which verifies the code's results. The second setting allows the user to run through all the different pressure ratios for a specific turbocharger, and the third setting allows the user to run through all the different pressure ratios for a specific turbocharger and find the maximum net power output. However, for this study, the second set was used and the maximum solar-to-mechanical efficiency and the net power output at that efficiency were found manually instead of rewriting the whole code to find the maximum solar-to-mechanical efficiency. Table E.6 summarises the structure for the '*once*' function.

Table E.6 Code structure summary of '*once*' function

```
%======================================================%
%%%%%%%%%%%%%%%%%%%%%% KNOWNS %%%%%%%%%%%%%%%%%%%%%%%%%%
%======================================================%
% All the known values are defined
% Such as environment properties
%======================================================%
%%%%%%%%%%%%%%%%%%%%%% CALCS %%%%%%%%%%%%%%%%%%%%%%%%%%
%======================================================%
% The code asks the user if the default settings should
be changed.


% The turbine pressure ratios and correct mass flow
rates are presented in a matrix


% The user selects which turbocharger to be run


% The user can choose one of the following:
1) Choose a specific operating point and recuperator
geometry
2) Run for all the turbine pressure ratios
3) Run for all the turbine pressure ratios and find
max efficiency



% For this study choice 1) and 2) was used.
% Choice 1):
rt = input('Turbine pressure ratio: ')
mtcf = input('Mass flow rate: ')
start = input('Recuperator geometry [a b L n] (example
[2 2 2 2]): ')
a_chn = input('Window channel thickness (m): ')


% Choice 2):
For MT = 1:1:3 (see Table 3.2),
      For Ts = 900:100:1200,
            For each turbine pressure ratio in
operating range of turbine
                  For each recuperator design (625
different combinations)
                        - Find $\dot{W}_{net}$ (equation (3.30)) and
```

```
                              η_sol (equation (3.31)) of cycle
                        -  Find  required  Q̇*  for  steady-
                           state operation at the phase-
                           change temperature.
                     end
                end
         end
 end
```

The objective function was maximised in the function called '*fun*'. This function had a similar structure as the one used by Le Roux and Sciacovelli (2019); however, the window's heat transfer and pressure drop were added in-between State 2 and State 3, as shown in Table E.7. The '*fun*' function is also used in an optimisation algorithm; however, in this study, the function was only used to output all of the cycle's performance parameters and find the maximum solar-to-mechanical efficiency manually. A summary of the code's structure is presented in Table E.7. The function called 'solar_flux', shown in Table E.7, is a function that interpolates between a few different solar heat fluxes on the receiver for various parabolic dish sizes.

Table E.7 Code structure summary of '*fun*' function

```
function [Function] = fun(Inputs)


% All the recuperator variables are defined
% a, b, Lreg and n


% Function of ratio between solar fluxes of different dish diameters is called
[mfn,cfn] = solar_flux()


% Initial values are assumed
% Main while loop uses temperature at state 7 with iterations less than 20 and
tolerance of 5
While (abs(T7(i) – T7(i-1)) > 5 && (i < 20)


% While loop in which temperatures and pressures are iterated


% Pressure at state 2 is calculated with pressure at state 3 plus pressure drop
```

E.7

```
across window


P2 = P3 + dP_win


% Temperature change across window is calculated with
dT23 = Q23/mfr/cp


% Temperature  at  state  3  is  calculated  with  temperature  at  state  2  plus
temperature change across window.


T3 = T2 + dT23
endwhile


% outside temp and press while loop calculate heat transfer across window
[outputs] = window(inputs)
% update while loop with new calculated values


endwhile


%outside main while loop calculated
% Entropy generation
% Net Power output, $\dot{W}_{net}$


% Display few important results


Function = -1*Wnet
if iteration > 15
      Make Wnet = 1
endif
endfunction
```

Appendix F

Octave code

F.1   Heat transfer functions

```octave
                % CAVITY HEAT TRANSFER COEFFICIENT
 function [h_cav] = HT_coeff_cavity(phi,L1,L2,L3,Tw,Tinf,v,Pr,k)
   % FROM S. Paitoonsurikan and K. Lovegrove, 2006
   %% KNOWNS
   Tf = (Tinf + Tw)/2;
   a = [4.08 -1.17 0.07];
   b = [5.41 7.17 1.99];
   c = [-0.11 -0.3 -0.08];
   L = [L1 L2 L3];
   g = 9.81;
   B = 1/Tf;
   %% CALCULATIONS
   for i = 1:length(L)
     Ls(i) = abs(a(i)*(cos((phi*pi/180) + c(i)))^(b(i))*L(i));
   end
   Ls = sum(Ls);
   Ra = ((g*B*(Tw-Tinf)*Ls^3)/(v^2))*Pr;
   Nu = 0.0196*Ra^0.41*Pr^0.13;
   h_cav = (Nu*k)/Ls;
 end
```

```
% Channel heat transfer coefficient %
function h_chn = HT_coeff_chn_R2(Dh,Re,Pr,k,ratio)
  Re_ave = mean(Re)
  for i = 1:length(Re)
    if Re(i) > 3000
      % check entry length turbulent
      L = 10*Dh;
      Nu_chn(i) = Nusturb(f(ratio,Re(i)),Re(i), Pr(i));
      h_chn(i) = (Nu_chn(i)*k(i))/Dh;
      L_ave = mean(L)
    endif

    if Re(i) <= 3000
      % check entry length laminar
      L_h = 0.05*Re*Dh
      L_t = 0.12*Re*Pr*Dh
      Nu_chn(i) = Nuslam(ratio);
      h_chn(i) = (Nu_chn(i)*k(i))/Dh;
      L_tave = mean(L_t)
      L_have = mean(L_h)
    endif
  endfor
endfunction
```

F.2   View factor function

```
function [F,F5] = view_fact(a_gl,L_div,L,N,N_div)

  %% Based on Martínez, I. Radiative View Factors. [cited 2020 5 October]; Available
from: http://webserver.dmt.upm.es/~isidoro/tc3/Radiation%20View%20factors.pdf.

  dc = [0:L_div:L];

  for h = 1:length(dc)-1

    x = [0, a_gl]; y = [0, L_div]; %% Coordinate set up for cells

    z = [0, a_gl]; n = [dc(h), dc(h+1)];


    x1 = [10^-6, a_gl]; y1 = [0, L_div];

    z1 = [10^-6, a_gl]; n1 = [dc(h), dc(h+1)];


    x2 = [10^-6, a_gl];y2 = [0, a_gl];

    z2 = [dc(h), dc(h+1)];n2 = [0, a_gl];


    A = (x(2)-x(1))*(y(2)-y(1)); %% Areas of cells

    A1 = (x1(2)-x1(1))*(y1(2)-y1(1));

    A2 = (x2(2)-x2(1))*(y2(2)-y2(1));
```

F.2

```matlab
B = 0;
B1 = 0;
B2 = 0;
F = 0;
Ff = 0;
Ff2 = 0;
for l = 1:length(z)
  for k = 1:length(n)
    for j = 1:length(y)
      for i = 1:length(x)
        B = B + (-1)^(i+j+k+l)*B_func(x(i),y(j),n(k),z(l),a_gl);
        F = (1/(2*pi*A))*B;
      end
    end
  end
end
F4(h) = F;              %% Parallel view factors for all cells
for l = 1:length(z1)
  for k = 1:length(n1)
    for j = 1:length(y1)
      for i = 1:length(x1)
        B1 = B1 + (-1)^(i+j+k+l)*B_func2(x1(i),y1(j),n1(k),z1(l));
        Ff = (1/(2*pi*A1))*B1;

      end
    end
  end
end
F3(h) = Ff;              %% perpendicular view factors for all cells
for l = 1:length(z2)
  for k = 1:length(n2)
    for j = 1:length(y2)
      for i = 1:length(x2)
        B2 = B2 + (-1)^(i+j+k+l)*B_func2(x2(i),y2(j),n2(k),z2(l));
        Ff2 = (1/(2*pi*A2))*B2;
      end
    end
  end
end
```

F.3

```matlab
        end
      F5(h) = Ff2;              %% view factor to backwall/aperture
   end
F6 = flip(F5);
F = zeros(N,N);

Fr1 = zeros(4,4);
Fr2 = zeros(4,4);
Fr3 = zeros(4,4);
Fr4 = zeros(4,4);
for i = 1:N
  for j = 1:N
    if j-i == 1
      F(i,j) = F3(1);
    elseif j-i == 2
      F(i,j) = F4(1);
    elseif j-i == 3
      F(i,j) = F3(1);
    end
  end
end
for i = 1:4
  for j = 1:4
    if j-i == 1
      Fr1(i,j) = F3(2);
    elseif j-i == 2
      Fr1(i,j) = F4(2);
    elseif j-i == 3
      Fr1(i,j) = F3(2);
    end
  end
end
Fr1 = Fr1 + triu(Fr1,-1)';
for i = 1:4
  for j = 1:4
    if j-i == 1
      Fr2(i,j) = F3(3);
    elseif j-i == 2
      Fr2(i,j) = F4(3);
```

```matlab
        elseif j-i == 3
            Fr2(i,j) = F3(3);
        end
    end
end
Fr2 = Fr2 + triu(Fr2,-1)';
for i = 1:4
    for j = 1:4
        if j-i == 1
            Fr3(i,j) = F3(4);
        elseif j-i == 2
            Fr3(i,j) = F4(4);
        elseif j-i == 3
            Fr3(i,j) = F3(4);
        end
    end
end
Fr3 = Fr3 + triu(Fr3,-1)';
for i = 1:4
    for j = 1:4
        if j-i == 1
            Fr4(i,j) = F3(5);
        elseif j-i == 2
            Fr4(i,j) = F4(5);
        elseif j-i == 3
            Fr4(i,j) = F3(5);
        end
    end
end
Fr4 = Fr4 + triu(Fr4,-1)';




F(1:4,5:8) = Fr1;
F(5:8,9:12) = Fr1;
F(9:12,13:16) = Fr1;
F(13:16,17:20) = Fr1;


F(1:4,9:12) = Fr2;
```

```matlab
    F(5:8,13:16) = Fr2;
    F(9:12,17:20) = Fr2;


    F(1:4,13:16) = Fr3;
    F(5:8,17:20) = Fr3;


    F(1:4,17:20) = Fr4;


    F = F + triu(F,-1)'; %% view factors for the individual cells


    Finf = zeros(2,N);
    F_inf(1,1:4) = F5(1); %% view factors to aperture
    F_inf(1,5:8) = F5(2);
    F_inf(1,9:12) = F5(3);
    F_inf(1,13:16) = F5(4);
    F_inf(1,17:20) = F5(5);
    F_inf(2,1:4) = F6(1); %% view factors to back wall
    F_inf(2,5:8) = F6(2);
    F_inf(2,9:12) = F6(3);
    F_inf(2,13:16) = F6(4);
    F_inf(2,17:20) = F6(5);


    F(1:N,N+1:N+2) = F_inf';
end
```

F.6

F.3 Gauss matrix function

```
function [A,B] =
gauss_mat_R1(N,A_div,A_chn,eps_gl,eps_inf,sig,c1,m1,m_dot,c_p,T_inf,Ta_in,h
_cav,h_chn,F,Finf,Q_abs)
  A = zeros(2*N+1,2*N+1);
  B = zeros((2*N+1),1);
  A_top = 0.25^2;

  B(1:(N+1),1) = -1*Ta_in;

  for i = 1:N+1
    B((N+1)+i) = Q_abs(i)  - A_div*eps_gl*sig*c1 +
A_div*eps_gl*sig*c1*sum(F(i,:)) + A_div*eps_inf*sig*Finf(1,i)*T_inf^4 +
h_cav(i)*A_div*T_inf;
  endfor

  for j = 1:N+1
    A(j,(N+1)+j) = (1/(h_chn(j)*A_chn) + 1/(2*m_dot*c_p));
    A(j,j) = -1;
    A(j+1:5,(N+1)+1:(N+1)+j) = 1/(m_dot*c_p);
  endfor

  for j = 6:10
    A(j+1:10,(N+1)+6:(N+1)+j) = 1/(m_dot*c_p);
  endfor
  for j = 11:15
    A(j+1:15,(N+1)+11:(N+1)+j) = 1/(m_dot*c_p);
  endfor

  for j = 16:N
    A(j+1:N,(N+1)+16:(N+1)+j) = 1/(m_dot*c_p);
  endfor

  for j = (N+1)+1:2*(N+1)
    A(j,j) = 1;
  endfor
  zz = ones(N,1);
  AA = diag(zz,0);

  for i = 1:N
    for j = 1:N
      A((N+1)+i,j) = (A_div*eps_gl*sig*m1 + A_div*h_cav(j))*AA(i,j) -
A_div*eps_gl*sig*m1*F(i,j);
    endfor
  endfor
  A(2*(N+1),N+1) = A_top*eps_gl*sig*m1 + A_top*h_cav(j);
```

F.4 Window code

```matlab
function [Qloss_tot,dP,Ts,h_chn] = window_R4(Trec,T2,m_T,a_chn,Qs_win)
  %%%%%%%%%%%%%%%%%%
  %%% TESTING %%%

  %%%%%%%%%%%%%%%%%%
  m_dot = m_T/5;
  Ta_in = T2;
  %% Edit this funcion if different inputs/assumptions is required
  [T_gap,c_p,eps_gl,eps_inf,t_gl,alpha,Tt_wall] = inputs();

  %% Edit this function for new cavity dimensions & other knowns
  [T_inf,P_inf,a,L,N,N_div,sig,I_sol,rho_dish,D_dish,eps_w,m1,c1] =
knowns();

  T_rec = Trec*ones(N+1,1); % Receiver temp assumption in Kelvin - must be
larger than 800K (for now)
  %T_rec = input('Input receiver temp assumption in Kelvin: ');
  % based on metlting point of thermal storage material

  % Cavity dimension
  a_cav = 0.25; % cavity width (square)

  %% air gap width %%
  t_gap = 0.065; % if this value is editted here it must also be changed in
SolTrace

  %new receiver wall dimensions
  a = a + 2*t_gap;
  b_chn = a_cav;% + 2*t_gl;
  b_gl = 0.27276;

  L_div = L/N_div;
  A_div = a_cav*L_div;
  A_chn = (2*a_chn + 2*b_chn)*L_div; %glass heat transfer area
  A_chnn = a_chn*b_chn; %channel area

  %============================%
  %%%%%%%%% CALCS %%%%%%%%%%%%%
  %============================%

  %%% Initialize values %%%
  tol = 1e-4;
  err1 = 1;
  err2 = 1;
  err = 1;
  Qnet_w(1) = 1000;
  c = 1;
  mat = ones(N+1,1);
```

```matlab
    Tf_chn = Tf_chni;

    %% Cavity heat transfer coefficient
    Tf_cavi = 350*mat; % average between cavity and glass surface
    Tf_cav = Tf_cavi;

    Ta1(1) = Ta_in;
    Ta2(1) = Ta_in;
    Ta3(1) = Ta_in;
    Ta4(1) = Ta_in;
    Ta5(1) = Ta_in; %% assumed the same flow goes through the top glass

    %% View factors
    %[F,Finf,F_rw] = view_fact(a_cav,a,L_div,L,N,N_div,t_gap);
    %[F,F3,F4,F5,F_rw] = view_fact(a_cav,a,L_div,L,N,N_div,t_gap);
    %[F,Frw,Finf,F5,F6,Ff2] = view_fact_R1(a_cav,a,L_div,L,N,N_div,t_gap);
    [F,Frw,Faper] = view_fact_R3(a_cav,a,L_div,L,N,N_div,t_gap);
    Finf = Faper;
    % NOTE: it is assumed that there is no net HT between the two glass panes
    %       thus, view factor is zero

    while c <= 5
##  while err >= tol

    %% Channel heat transfer coefficient
    ratio = b_chn/a_chn;
    rho_chn = rho(Tf_chni-273,P_inf)';
    rho_chn;
    mu_chn = mu(Tf_chni-273)';
    nu_chn = mu_chn./rho_chn;
    Pr_chn = Pr(Tf_chni-273)';
    k_chn = thermalcond(Tf_chni-273);
    Dh_chn = (2*a_chn*b_chn)/(a_chn+b_chn);
    V_chn = m_dot./(A_chnn.*rho_chn);
    Re_chn = (rho_chn.*V_chn*Dh_chn)./mu_chn;
    B_chn = (1./Tf_chni);
##    Gr_chn = (9.81.*B_chn.*(Ts - T_inf).*Dh_chn^3)./(nu_chn.^2);
    h_chn = HT_coeff_chn_R1(Dh_chn,Re_chn,Pr_chn,k_chn,ratio);
    h_chn = h_chn';
    %% Cavity heat transfer coefficient
    rho_cav = rho(Tf_cavi-273,P_inf)';
    mu_cav = mu(Tf_cavi-273)';
    nu_cav = mu_cav./rho_cav;
    Pr_cav = Pr(Tf_cavi-273)';
    k_cav = thermalcond(Tf_cavi-273)';
    h_cav = HT_coeff_cavity_R1(45,a_cav,L,Ts,T_inf,nu_cav,Pr_cav,k_cav);
```

```matlab
    %% Pressure drop %%
##    e_rough = 0.01e-6; % from J.A Berger et al
##    ratio = e_rough/Dh_chn;
##    f_chn = colebrook(Re_chn,ratio);

    f_chn = f_R1(ratio, Re_chn);
    dp = f_chn'*(L/Dh_chn).*(V_chn.^2/2).*rho_chn;
    %% Receiver wall radiation
    Qrad_rec = A_div.*Frw'.*sig.*abs(T_rec.^4 - Ts.^4);
    Qrad_w = sum(alpha*Qrad_rec);
    Qrr = alpha*Qrad_rec;
    Qconv_rec = sum(Q_enc);
    Q_star = Qs_win + Qrr + Q_enc;


    %% Gauss matrix setup
    [A,B] =
gauss_mat_R1(N,A_div,A_chn,eps_gl,eps_inf,sig,c1,m1,m_dot,c_p,T_inf,Ta_in,h
_cav,h_chn,F,Finf,Q_star);

    %% Gauss Elimination
    X = A\B;
    Ts_new = X(1:N+1);
    Qnet_r = X(N+2:end);
##    Qnet_w = sum(Qnet_r(1:5));
    Qnet_w(c+1) = sum(Qnet_r(1:5));

    for h = 2:N_div+1
      Ta1(h) = Qnet_r(h-1)/(m_dot*c_p) + Ta1(h-1);
      Tf_ave1(h-1) = (Ta1(h) + Ta1(h-1))/2;
      dT1(h-1) = (Ta1(h) - Ta1(h-1));

      Ta2(h) = Qnet_r(h+4)/(m_dot*c_p) + Ta2(h-1);
      Tf_ave2(h-1) = (Ta2(h) + Ta2(h-1))/2;
      dT2(h-1) = (Ta2(h) - Ta2(h-1));

      Ta3(h) = Qnet_r(h+9)/(m_dot*c_p) + Ta3(h-1);
      Tf_ave3(h-1) = (Ta3(h) + Ta3(h-1))/2;
      dT3(h-1) = (Ta3(h) - Ta3(h-1));

      Ta4(h) = Qnet_r(h+14)/(m_dot*c_p) + Ta4(h-1);
      Tf_ave4(h-1) = (Ta4(h) + Ta4(h-1))/2;
      dT4(h-1) = (Ta4(h) - Ta4(h-1));
    end
    Ta5(2) = Qnet_r(N+1)/(m_dot*c_p) + Ta5(1);
    Tf_ave5(1) = (Ta5(2) + Ta5(1))/2;
    dT5 = (Ta5(2) - Ta5(1));
```

F.10

```
    Ta = mat;
    j = 2:6;
    Ta(1:5) = Ta1(j);
    Ta(6:10) = Ta2(j);
    Ta(11:15) = Ta3(j);
    Ta(16:20) = Ta4(j);
    Ta(21) = Ta5(2);
    Tf_chni = Tf_ave; % work only in kelvin


    Tfc = (T_inf+Ts_new)/2;

    Tf_cavi = Tfc;

    Qtest1 = m_dot*c_p.*dT;
    Qtest2 = h_chn.*A_chn.*(Ts - Tf_chni);
    QL_rad = Finf'.*eps_gl*sig*(A_div).*(Ts.^4 - T_inf.^4);
    QL_conv = (h_cav.*A_div.*(Ts - T_inf)); % do different calc
    %Qloss = QL_rad + QL_conv;
    %Qcheck = Qabs + Qrec_w + Qloss;
    err1 = abs(Qnet_r - Qtest1);
    err2 = abs(Qnet_r - Qtest2);
    err2;
##    Qloss_r = sum(QL_rad(1:5));
    Qloss_r = sum(QL_rad);
##    Qloss_cv = sum(QL_conv(1:5));
    Qloss_cv = sum(QL_conv);
    Qloss_tot = Qloss_cv + Qloss_r;

    Ts = Ts_new;
    Tf_chn = Tf_chni;
    Tf_cav = Tf_cavi;
    T1 = T_rec; % for enclosure HT
    T11 = T1;
    T2 = Ts;
    T22 = T2;
    c = c + 1;
    err = abs(Qnet_w(c) - Qnet_w(c-1));

  end
  dP = sum(dp);
endfunction
```